UNIVERSITY OF CALIFORNIA,
IRVINE

Physical-Biogeochemical Interactions Driving Low Oxygen Events at Dongsha Atoll

DISSERTATION

submitted in partial satisfaction of the requirements
for the degree of

DOCTOR OF PHILOSOPHY

in Civil and Environmental Engineering

by

Sarah Ruth Merrigan

Dissertation Committee:
Associate Professor Kristen Davis, Chair
Professor Geno Pawlak
Professor Brett Sanders

2024

"The ocean is so big,
We are so small,
And nothing really matters"
–Dongsha Atoll, 2019

TABLE OF CONTENTS

LIST OF FIGURES

Page

LIST OF TABLES

ACKNOWLEDGMENTS

I would first like to thank my advisor, Dr. Kristen Davis, who has continuously supported me throughout the entirety of my graduate career. Kristen has provided me with both the guidance and resources necessary to succeed, as well as the freedom to pursue my own interests and think independently. I am grateful to her for providing me my first opportunity to explore oceanography and for all the research and fieldwork adventures since!

I would also like to thank Dr. Geno Pawlak for his mentorship and guidance. I am grateful for his invaluable knowledge and input throughout the entirety of my PhD. Geno's rigorous contributions have elevated the quality of my research.

Thank you to Dr. Brett Sanders, who has served on all my committee throughout my PhD, for his advice and feedback. Also, thank you to Dr. Tirtha Banerjee, Dr. Joleah Lamb, and Dr. Russ Detweiler for their support during my preliminary and qualifying exams.

I am thankful for the camaraderie and support of all my Coastal Dynamics lab members: Emma Reid, Aryan Safaie, Christina Frieder, Greg Sinnett, Isa Arzeno, Sam Kastner, Jared Brzenski, Madolyn Kelm, and Shuwen Tan.

Special thanks to all my collaborators, who provided essential guidance and contributions to my research. I would like to thank Ke-Hsien Fu for his help in the field for generously providing data and guidance. My fieldwork would have not been possible without the additional help of Yi-Bei Liang and Heather Crume.

I would like to acknowledge and express my gratitude for the Friday Harbor Laboratories Estuarine and Coastal Fluid Dynamics course, for providing me inspiration and an educational foundation, as well as a wonderful group of peers and friends.

Most importantly, I would like to thank my family. Thank you to my parents for their unwavering love and support. Thank you to Alex for your constant encouragement, love, and willingness to read my first drafts.

I would like to thank the Ridge 2 Reef program for the funding support through the Ridge 2 Reef Fellowship and providing me with foundational skills to succeed in my graduate studies and support my career goals.

VITA

Sarah Ruth Merrigan

EDUCATION

Doctor of Philosophy in Civil and Environmental Engineering **2024**
University of California, Irvine *Irvine, CA*

Masters of Science in Civil Engineering **2019**
University of Arizona *Tucson, AZ*

Bachelor of Science in Civil Engineering **2017**
University of Arizona *Tucson, AZ*

RESEARCH EXPERIENCE

Graduate Research Assistant **2018–2024**
University of California, Irvine *Irvine, California*

TEACHING EXPERIENCE

Teaching Assistant **2021–2023**
University of California, Irvine *Irvine, CA*

Open Channel Hydraulics *Spring 2021*
Computational Problem Solving *Spring 2021,2023*

CONFERENCE PRESENTATIONS

S.R Merrigan, G. Pawlak, K.H. Fu, K. Davis, "Physical processes shaping low oxygen events in a highly flushed coral atoll lagoon" **Feb 2024**
Poster Presentation at Ocean Sciences Meeting

S.R Merrigan, G. Pawlak, K.H. Fu, K. Davis, "Low oxygen conditions in a highly flushed coral atoll lagoon: Physical processes driving bottom water oxygen dynamics" **June 2023**
Poster and Oral Presentation at Gordon Research Conference and Seminar

S.R Merrigan, G. Sinnett, G. Pawlak, K. Davis, "A heat budget of a tidally flushed atoll lagoon" **Feb 2022**
Oral Presentation at Ocean Sciences Meeting

S.R Merrigan, G. Sinnett, G. Pawlak, K. Davis, "A heat budget of a tidally flushed atoll lagoon" **November 2021**
Oral Presentation at Coastal and Estuarine Research Federation Conference

S.R Merrigan, G. Sinnett, G. Pawlak, K. Davis, "Circulation in a tidally-flushed atoll lagoon" **Feb 2020**
Poster Presentation at Ocean Sciences Meeting

ABSTRACT OF THE DISSERTATION

Physical-Biogeochemical Interactions Driving Low Oxygen Events at Dongsha Atoll

By

Sarah Ruth Merrigan

Doctor of Philosophy in Civil and Environmental Engineering

University of California, Irvine, 2024

Associate Professor Kristen Davis, Chair

Oxygen levels in the global coastal ocean have drastically decreased in past decades with a surge in reported hypoxic events. In most coastal systems, hypoxia is induced through eutrophication, long residence times, and lack of ventilation to the atmosphere. Understanding the complex physical and biogeochemical processes in these systems is crucial for ecosystem health and resilience.

Dongsha Atoll is a coral atoll and Taiwanese National Park located in the northern South China Sea. In summers 2014 and 2015, hypoxia-related fish kills, coral bleaching, and sea grass die offs were observed on the eastern edge of Dongsha Atoll lagoon, motivating further work to understand the key drivers of hypoxia. This body of work focuses on a field campaign in summer 2019. Here, I aim to further our understanding of how physical-biogeochemical interactions drive oxygen availability in tropical reef-lagoon systems.

First, I construct a heat and volume budget for the lagoon to understand the physical processes governing heating, circulation, and ocean-lagoon exchange. Results show that surface heat fluxes drive rapid heating of the lagoon by $\sim$1.5°C over the 22-day study period. Advective transport over the reef flat from tide- and wave-driven flows is an important component of ocean-lagoon exchange that is balanced by a net outflow through the channels on subtidal timescales. Specifically, a near phase-locked interaction between diurnal solar

forcing and near-diurnal tidal exchange drives persistent advective cooling over the reef flat.

Next, in order to understand the physical processes governing residence time and renewal of the bottom waters, I construct a bottom water mass budget in Dongsha Atoll lagoon. Results show frequent bottom water renewal events driven by tidally modulated advective processes through the lagoon channels and over the reef flat. Though bottom water renewal events are usually a mechanism for refreshing oxygen levels in stratified systems, the water advected into Dongsha Atoll lagoon from the reef flat can, at times, be hypoxic. The water flowing off of the reef flat into the Dongsha Atoll lagoon is intermittently oxygen deficient, due to seasonal phase-alignments between the primarily diurnal tidal flow and biological respiration on the reef. During the study period, the flood phase of the tide, which drives flow of cooler offshore water across the reef flat from the ocean to the lagoon, occurred at night when strong biological respiration draws down oxygen on the shallow reef flat. These cooler, low oxygen waters sink to the bottom of the stratified lagoon waters, creating a pool of isolated low-oxygen water.

Lastly, I examine the drivers of low oxygen on the east reef flat of Dongsha Atoll. Results show that the diurnal biological cycle on the reef flat is in phase with diurnal flood-at-night tidal forcing, which together leads to strong nocturnal oxygen drawdown. Lagoonward flow at night then transports the low oxygen water to the lagoon boundary. This process results in episodic low-oxygen events at depth inside the lagoon. We show that this pattern is seasonal on Dongsha Atoll due to the annual phasing of the diurnal tides, with the flood phase of the tide consistently occurring at night during summer months. Our findings underscore the potential significance of physical-biological interactions in other reef systems with diurnal tides, emphasizing the need for further work to elucidate oxygen dynamics in coastal tropics.

Chapter 1

Introduction

1.1 Motivation

Dissolved oxygen is a vital resource in marine environments, influencing productivity, biodiversity, and biochemical processes (Breitburg et al., 2018). Unfortunately, over the past 80 years, observed oxygen concentrations across the global ocean have decreased approximately 2% as a result of rising ocean temperature and resultant heat wave events (Frölicher et al., 2018), as well as eutrophication, leading to the expansion of oxygen minimum zones (Stramma et al., 2008; Keeling et al., 2010; Breitburg et al., 2018; Diaz and Rosenberg, 2008; Rabalais et al., 2010a). This trend is expected to continue with projected decreases in global oxygen concentrations of 1-7% over the next century (Keeling et al., 2010; Long et al., 2016). Hypoxia is defined as dissolved oxygen concentrations ≤ 2 mg L^{-1}. However, recent studies have shown sublethal ecosystem damage at oxygen concentrations as high as 5 mgL^{-1} (Vaquer-Sunyer and Duarte, 2008).

Various stressors, including eutrophication, biological demands, and physical processes, such as mixing and advective transport, exacerbate deoxygenation in coastal regions (Breitburg

et al., 2018; Gilbert et al., 2010). Eutrophication can be driven by both anthropogenic sources, such as agricultural runoff and sewage, as well as natural phenomena like upwelling (Howarth, 2008; Diaz and Rosenberg, 2008; Chan et al., 2008).

Studies of coastal hypoxia have primarily been limited to temperate climates (Scully, 2010, 2013; Bianchi et al., 2010). Tropical coral reef systems have historically been assumed to be well-oxygenated, however, a global literature review conducted by Altieri et al. (2017) shows that tropical dead zones are likely dramatically under reported. Though some work has been done to research hypoxia in deep tropical systems (e.g. Kealoha et al. (2020); Bates (2017); Scranton et al. (2014)), there is a critical gap in understanding hypoxia in the shallow tropics.

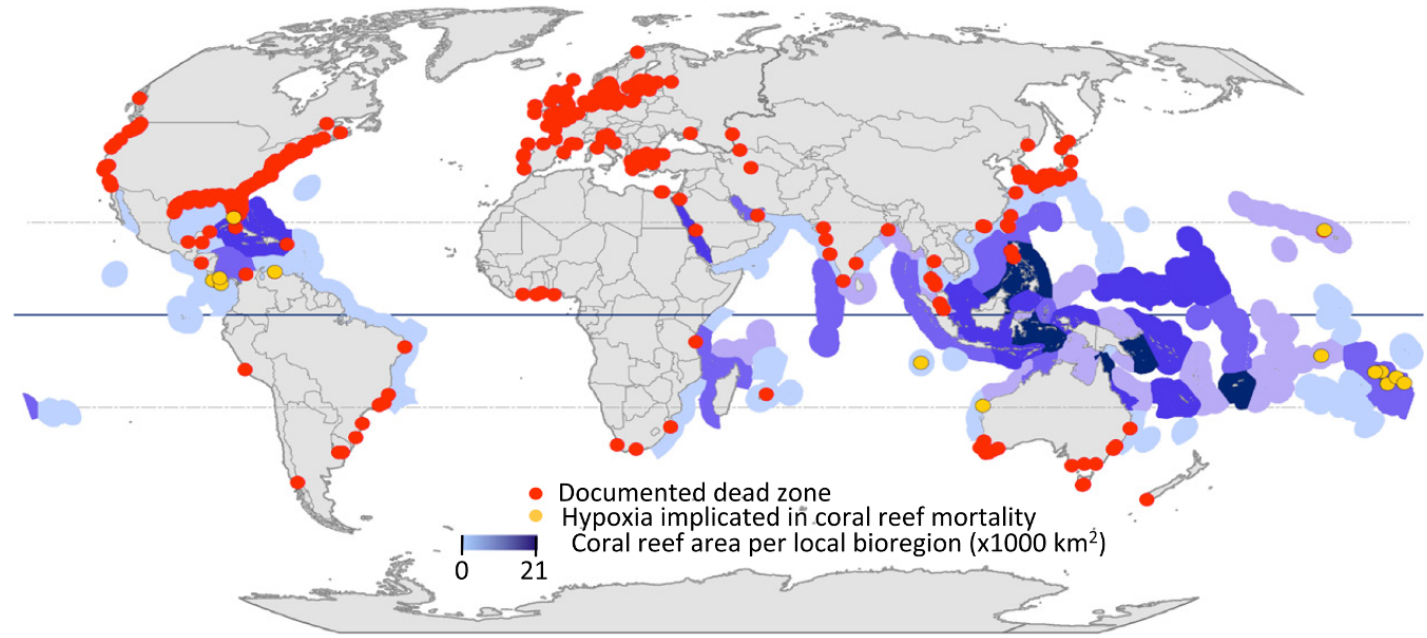

Figure 1.1: Global map with all known dead zones (red dots) and coral reefs where hypoxia has been implicated in mass mortality of reef organisms (gold dots). Documented dead zones are notably concentrated in temperate regions in areas with relatively greater research capacity, whereas coral reefs are found primarily in the tropics. The solid horizontal line represents the equator, and the upper and lower dashed lines represent the Tropics of Cancer and Capricorn respectively. Intensity of purple color indicates densities of coral reef area per ecoregion, from lightest to darkest: 0, 1–1,000, 1,001–2,500, 2,501–5,000, 5,001–10,000, and 10,001–21,000 km^2. (Altieri et al., 2017)

1.2 Physical and Biogeochemical Controls on Hypoxia

The oxygen variability in coral reef systems are controlled by both physical and biogeochemical processes. Physical mechanisms, such as stratification, can limit oxygen availability at depth, creating hypoxia and isolating bodies of water through inhibited air-sea gas exchange and restricted renewal events (Fennel and Testa, 2019; Farmer and Freeland, 1983). Stratification commonly develops due to quiescent wind, wave, or tidal conditions, inhibiting vertical mixing, as well as freshwater input via river inflow or precipitation. Hypoxia can be relieved through wind- or wave-driven vertical mixing, convective cooling, or renewal events (Stanley and Nixon, 1992; Boesch and Rabalais, 1991; Kemp et al., 2009a). Deep water renewal events, which typically transport dense, higher oxygen water to depth, have been primarily observed in fjords (Gade and Edwards, 1980), but a recent study observed this mechanism in a tropical embayment (Adelson et al., 2022).

Biological cycles include which influence oxygen in coastal waters primary production (adding oxygen to the water column during the day through photosynthesis) and respiration (the rate at which organisms consume oxygen). Primary production occurs only during the day while respiration happens continuously, but is a dominant process at night when primary production is absent. In very shallow waters, hypoxia can occur on diurnal timescales due to the relative influence of depth and biological respiration (DeCarlo et al., 2017a; Tyler et al., 2009a; D'Avanzo and Kremer, 1994). Additionally, temperature plays a crucial role in determining oxygen availability– increasing ocean temperature reduces the oxygen solubility of water and increases biological respiration, exacerbating the effects of thermal stress on coral reefs (Vaquer-Sunyer and Duarte, 2011).

1.3 Lagoon Hydrodynamics

Hydrodynamics control the spatial distribution of heat, nutrients, and oxygen within a lagoon system (Falter et al., 2004; Gruber et al., 2017). For atoll lagoons, hydrodynamics are dependent on both the morphology of the atoll and the local forcing mechanisms, such as tides, waves, and wind (Hench et al., 2008; Green et al., 2018; Dumas et al., 2012; Rogers et al., 2017).

Atoll systems are comprised of reef or land encompassing a shallow lagoon surrounded by open ocean, and are often classified based on their connectivity to open ocean. Atoll connectivity varies from enclosed, with continuously exposed rims, to open, where a reef flat is perpetually submerged. Semi-enclosed lagoons have a combination of a raised rim, reef flat, and/or deeper channels (Goldberg, 2016). For enclosed atoll lagoons, as studied in Callaghan et al. (2006), waves are the primary driver of circulation, setting up a pressure gradient, forcing flow over the reef flat. In semi-enclosed lagoons, the influence of tides is more significant due to the presence of channels allowing for increased exchange between lagoon and the open ocean (Green et al., 2018; Dumas et al., 2012).

Though many of the past studies have focused on the importance of wave- and wind-driven flow in lagoons (Hench et al., 2008; Callaghan et al., 2006; Costa et al., 2017; Dumas et al., 2012), tides can have a large role in driving circulation in lagoons with narrow channels that constrict flow between open ocean and lagoon waters (Green et al., 2018; Dumas et al., 2012). In reef-lagoon systems, water quality and biogeochemical properties are dependent on circulation and water renewal timescales, which are dictated by flow through the channels and over the reef (Andréfouët et al., 2001; Pagès et al., 2001).

1.4 Dongsha Atoll

Dongsha Atoll is a semi-enclosed coral atoll and Taiwanese National Park located in the northern South China Sea with a diameter of 28 km and a surface area of approximately 600 km^2 (Dai, 2004). The atoll is characterized by a central lagoon surrounded by a wide ($\sim$3 km) reef flat to the north, east, and south, and flanked by two channels on the west separated by a small island. Large internal waves generated in the Luzon Straight break on the forereef of the atoll, bathing the surrounding reef flat with cool, nutrient dense water, influencing the circulation and resultant temperature and nutrient variability across the reef (Davis et al., 2020; Sinnett et al., 2022; Reid et al., 2019). In summers 2014 and 2015, hypoxia related fish-kills and sea grass die offs were observed in the eastern and northeastern region of the lagoon, motivating further understanding of the circulation and oxygen dynamics inside the lagoon (Gajdzik and DeCarlo, 2017). Dongsha is a unique system in that it is geographically remote with limited anthropogenic influence on the environment. Additionally, unlike many coastal and estuarine systems, there is no freshwater inflow, making precipitation the only freshwater source. These key features position Dongsha Atoll as an ideal natural system for studying hypoxia by isolating the physical and biological processes driving oxygen dynamics.

1.5 Outline of Dissertation

In Chapter 2, I construct a heat budget for the lagoon to understand the physical processes governing circulation and ocean-lagoon exchange and examine the influence of tides, winds, waves, advective exchange, and surface heating on lagoon heating and flushing time.

One of the most common features linking globally documented low oxygen zones is temperature. By the end of the century, globally documented hypoxic zones are expected to warm, on average, over 2 °C (Altieri and Gedan, 2015; Diaz and Rosenberg, 2008). For reef

systems, a link between temperature and hypoxia has been well established. In a study of 11 hypoxia-driven mass mortality events across Pacific atoll lagoons, 10 of them occurred during warm seasons (Andréfouët et al., 2015). This relationship between temperature and oxygen levels is due to both physical and biological processes including increased stratification, a higher demand for oxygen in warm water from increased organism metabolic rates, and lower oxygen solubility in warm water (Brown et al., 2004; Best et al., 2007; Weiss, 1970; Nelson and Altieri, 2019; Altieri and Gedan, 2015).

These studies demonstrate that temperature is an important proxy in understanding an atoll system's oxygen dynamics. The temperature and water properties of reef flat and offshore water also affects oxygen availability in atoll systems and can influence lagoon biodiversity (Bicchi et al., 2002; Kraines et al., 1996). Over the past 20 years, multiple severe warming events have been recorded at Dongsha and studies show that the lagoon ecosystem has not completely recovered from a severe warming event in 1998 (Tkachenko and Soong, 2017; Chen and Lin, 2017). Chapter 2 is in peer review at *Limnology and Oceanography.*

In Chapter 3, I construct a bottom water mass budget in Dongsha Atoll lagoon in order to understand the physical processes governing flushing time and renewal of the lagoon bottom waters. The heat budget allows us to understand the physical mechanisms controlling exchange with the open ocean, thereby influencing the properties of water inside the lagoon. However, the lagoon is often stratified, creating a surface layer that is regularly mixed by winds and refreshed by incoming water through the channels, as well as a bottom layer with restricted ventilation and a likely longer residence time compared to the surface layer. Biological activity can then draw down available oxygen, causing the bottom layer to become hypoxic.

Ambient bottom water is renewed through the advection of water with equal or greater density, or through vertical mixing. Wind, wave, convective cooling at the surface, and tidal forcing can lead to vertical mixing, decreasing stratification and entraining ambient

bottom water with near surface water. Precipitation, strong surface heating, and quiescent winds, waves, and tides all strengthen stratification, which inhibits bottom water renewal, and allows for the potential for bottom water to become hypoxic.

Quantifying the timescales for bottom water renewal is a common framework for considering oxygen recovery in enclosed basins, such as fjords, and on shelves (Bograd et al., 2002; Arneborg et al., 2004; Li et al., 2015). Renewal events are identified by looking at the difference between offshore water properties and the ambient basin bottom water properties: if the offshore water is denser than ambient basin water at depth, it can replenish otherwise stagnant waters (Bograd et al., 2002; Gillibrand et al., 1996). These events are often periodic and occur on tidal to seasonal timescales (Geyer and Cannon, 1982; Gillibrand et al., 1996). Renewal of bottom water replenishes a system's oxygen and nutrient levels (Gillibrand et al., 1996). Systems devoid of bottom water renewal events are more prone to hypoxia or anoxia, and related mortality events (Hartstein et al., 2019). Though much of the literature surrounding the study of bottom renewal events is focused on fjords, the methodology can be applied to estuaries and enclosed basins where bathymetric features impact water exchange with the open ocean (Bograd et al., 2002; Li et al., 2015; Adelson et al., 2022).

In Chapter 4, I use a heat and oxygen budget on the east reef flat of Dongsha Atoll to understand the physical and biogeochemical drivers of low oxygen. Reef flat oxygen availability is controlled by various physical and biogeochemical processes, including biological oxygen production and consumption, air-sea gas exchange, and advection (Nelson and Altieri, 2019; Kraines et al., 1996). On shallow reef flats, primary production can drive saturated oxygen levels during the day, while respiration can drive oxygen drawdown to hypoxic levels at night (Kinsey and Kinsey, 1967; Kraines et al., 1996; Ohde and van Woesik, 1999). Oxygen levels are also influenced by advective processes, which can transport water from the lagoon or the open ocean across the reef flat (Kraines et al., 1996).

Systems with hypoxia timescales of hours to days are often a result of biological processes,

anthropogenic eutrophication, or stratification (D'Avanzo and Kremer, 1994; Borsuk et al., 2001; Tyler et al., 2009a; Turner et al., 1987; Gilbert et al., 2010). Dongsha Atoll is a geographically isolated system with limited anthropogenic influence. Results from Chapter 2 and 3 show that the lagoon is well-flushed with flushing timescales of 3 days and 3-4 days for the bulk lagoon and lagoon bottom water, respectively, making the system relatively well flushed for a system with observed hypoxic events (Fennel and Testa, 2019). During the study period covered in this body of work, the primarily diurnal tides at Dongsha Atoll are phase locked with the diurnal biological cycle on the shallow reef flat. Chapter 3 highlights a mechanism for the advection formation of hypoxia at depth inside the lagoon: at night, respiration draws down oxygen to hypoxic levels on the reef, which is then advected into the lagoon by flooding tides. In Chapter 4, we aim to further explore the physical-biogeochemical interactions on the reef flat of Dongsha Atoll to understand the physical drivers of oxygen variability on the reef flat that lead to the formation of these low oxygen pulses at depth inside the lagoon.

Chapter 2

Relative phase between tidal and solar cycles influences the heating of a coral atoll lagoon

2.1 Introduction

Hydrodynamics shape both the physical and biogeochemical environment in reef-lagoon systems, influencing the spatial distribution of heat, nutrients, and oxygen, as well as circulation and residence time (Andréfouët et al., 2001; Pagès et al., 2001; Kraines et al., 1996). Circulation within atoll lagoons is dependent on both the geomorphology of the atoll and local forcing mechanisms, such as tides, waves, and wind (Hench et al., 2008; Green et al., 2018; Dumas et al., 2012; Rogers et al., 2017). Atoll morphology varies from enclosed, with continuous and exposed rims at mean sea level, to open, where a reef flat is constantly submerged. For enclosed atoll lagoons, as studied in Callaghan et al. (2006), waves are the primary driver of circulation, setting up a pressure gradient that forces flow over the reef flat. In

semi-enclosed atolls, which are characterized by a combination of a raised rim, reef flat, and/or deeper channels, the influence of tides is generally more significant due to the presence of channels allowing for increased exchange between lagoon and the open ocean (Green et al., 2018; Dumas et al., 2012; Goldberg, 2016). Though many past studies have focused on the importance of wave- and wind-driven flow in lagoons (Hench et al., 2008; Andréfouët et al., 2001; Callaghan et al., 2006; Costa et al., 2017; Dumas et al., 2012; Kraines et al., 1999; Rogers et al., 2017; Tartinville et al., 1997), tides can also be an important driver of circulation (Green et al., 2018; Dumas et al., 2012).

The focus of this study is Dongsha Atoll, a Taiwanese national park located in the South China Sea (SCS, Figure 3.1a). Previous work at Dongsha Atoll has focused on understanding the shoaling and impact of internal waves, as well as the dynamics controlling flow and exchange of nutrients and heat on the reef flat (Davis et al., 2020; DeCarlo et al., 2017a; Reid et al., 2019, 2020; Sinnett et al., 2022). Chen (2023) investigated lagoon dynamics during monsoon conditions, showing the importance of wind- and wave-driven forcing on lagoon hydrodynamics during these periods. The northern part of the South China Sea has large internal waves that are generated in the Luzon Strait and break on the east side of the atoll, bathing the surrounding reef flat with cool, nutrient rich water (Davis et al., 2020; Sinnett et al., 2022; Alford et al., 2015). Despite the cooling influence of these internal waves, multiple severe warming events have been recorded at Dongsha Atoll in the past 20 years. The lagoon ecosystem has yet to completely recover from a particularly severe warming event in 1998 (Tkachenko and Soong, 2017; Chen and Lin, 2017).

In summers 2014 and 2015, there were hypoxic related die offs observed in the northwest corner of Dongsha Atoll lagoon (Gajdzik and DeCarlo, 2017), motivating better understanding of circulation within the system. Understanding the connection between physical processes and oxygen dynamics in coastal systems is important, as oxygen levels in the global coastal ocean have drastically decreased in past decades, causing a surge of hypoxic (or low-oxygen,

4.6 mg/L; Vaquer-Sunyer and Duarte (2008)) events associated with fish kills, sea grass die off, and coral bleaching (Altieri et al., 2017; Gilbert et al., 2010; Zhang et al., 2010). The goal of this study is to use heat as a tracer to identify the physical forcing mechanisms driving lagoon-ocean exchange to better understand the flushing time scales inside the lagoon. We show that, during our study period, shortwave solar radiation is the primary driver of heating in the lagoon and is balanced by tidal and wave driven advective fluxes over the reef flat and through the channels.

2.2 Methods

2.2.1 Field Site Description

Dongsha Atoll is a partially enclosed atoll and has a diameter of 28 km and an area of approximately 600 km^2 (Dai, 2004) (Figure 3.1), with a central lagoon with a diameter of 14 km and an approximate area of 200 km^2. The lagoon is surrounded by a shallow reef flat approximately 2-3 km wide. Pratas Island, on the western side of the atoll, is flanked to the north and south by two channels, approximately 8 and 11 m deep, respectively. The lagoon has an average depth of 11 m and a maximum depth of 22 m. It has a sandy bottom studded with reef patches extending up to 1 m from the surface.

2.2.2 Observations

The presented observations are part of a larger study of internal wave propagation around Dongsha Atoll (Sinnett et al., 2022; Ramp et al., 2022). We used measurements of currents, pressure, and temperature in and surrounding the lagoon (channels, reef flat, forereef), as well as meteorological measurements taken on Pratas Island collected from 20 May 2019 -

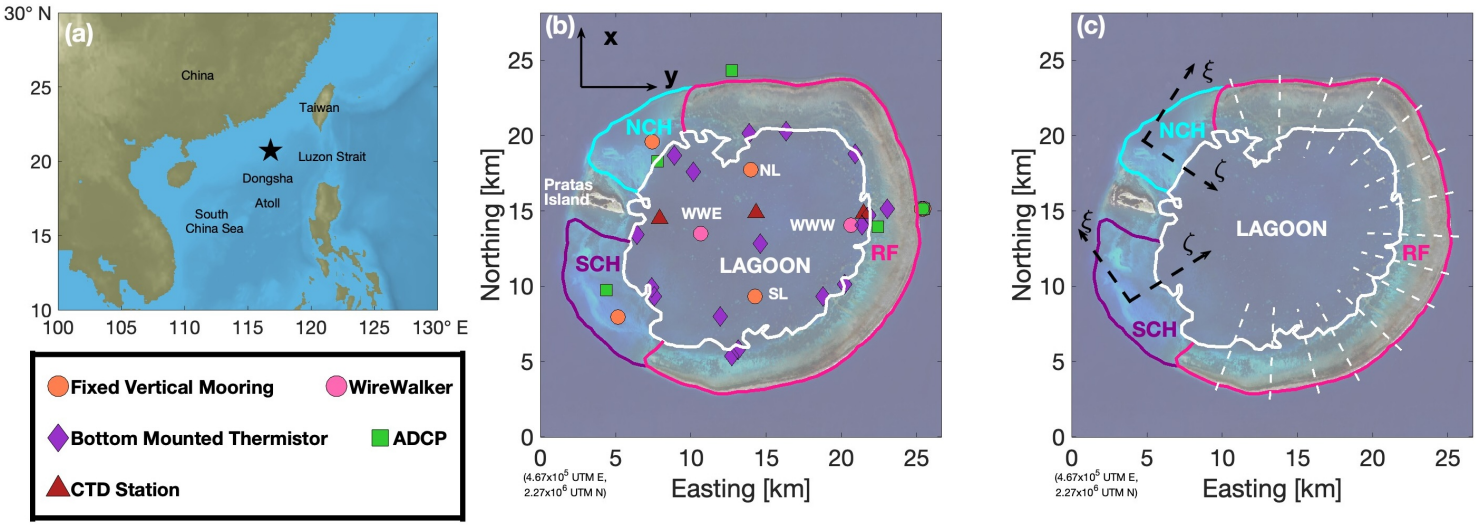

Figure 2.1: a) Map with location of Dongsha Atoll in the South China Sea with, b) instrument locations during the 2019 lagoon experiment. The white lagoon outline is defined by an 8 meter bathymetric contour. Reef Flat (RF), North Channel (NCH), and South Channel(SCH) outlines are approximate. c) Map showing each section of lagoon system. Dashed white lines represent each reef flat section used for flow estimation. Black dashed arrows show rotated advective flux local cartesian coordinate system for North Channel and South Channel. Velocity measurements are rotated so east-west (ζ) flow into lagoon is perpendicular to lagoon boundary. The same approach was used for each section of the reef flat.

09 June 2019 (Figure 3.1). Instrumentation is detailed in Table 2.1, but will be described briefly below.

Water temperature in the lagoon was measured on two fixed vertical moorings in the north and south lagoon, two vertically profiling moorings (WireWalkers, Rainville and Pinkel (2001)) in the east and west lagoon, and on bottom moored thermistors at various locations around the lagoon (Figure 3.1b). Water temperature was measured in both the north channel (NCH) and south channel (SCH) on fixed vertical moorings (Figure 3.1). Temperature sensors used in the experimental array include RBR Concerto sampling at 5 hertz, Seabird Electronics SBE-37s (conductivity, temperature, pressure) sampling at a 1 minute interval, SBE-56s and RBR soloTs sampling at 1 second, (all measuring temperature to $\pm$ 0.002°C), HOBO U22 Water Temp Pro sensors, sampling at 1 minute intervals (bottom

moored thermistors; measuring temperature to ± 0.2°C), and JFE RINKO W sensors, sampling at 15 minute intervals (bottom mounted, measuring temperature to ± 0.02°C). Water temperature was measured on the east reef flat with a bottom moored RBR-soloT, sampling at 1 second intervals (RF in Figure 3.1b). Thermistors were calibrated using a linear offset determined from a pre-deployment calibration bath. Corrected temperatures are within 0.055 °C. Additionally, water temperature and salinity were measured with depth approximately every 2 days throughout the study period by a SonTek YSI Castaway CTD at three stations at the west, center, and east lagoon (triangles, Figure 3.1b).

Water velocities were measured by three 1200kHz Teledyne RDI Workhorse Acoustic Doppler Current Profilers (ADCPs), one in the north channel, one in the south channel, and one on the east reef flat, all sampling at 2-second intervals (Figure 3.1b). Pressure in the lagoon was recorded by a SBE-37 on the north lagoon mooring, reef flat pressure was recorded by the east reef flat ADCP and offshore pressure by a bottom mounted ADCP located on the 10 m mooring on the east forereef, outside of the lagoon (Figure 3.1b).

The meteorological data used in this study was measured at the airport located on Pratas Island. Measurements include precipitation and shortwave radiation sampled at 1-minute intervals. Offshore conditions including wind speed, wind direction, significant wave height, and direction were obtained from the European Center for Medium-Range Weather Forecasts (ECMWF) ERA5 1-hour data on a 30-km grid (Hersbach et al., 2020).

2.3 Model of Exchange Between the Lagoon and Ocean

An analytical model of lagoon-ocean exchange is developed to estimate changes in lagoon volume and heat content and, ultimately, to better understand the residence time of water in the lagoon. The model considers flow over the shallow reef flat and through the deep

channels, as well as heat fluxes through the lagoon surface (Figure 3.1c). All variables used in the model are summarized in Table 2.2.

2.3.1 Lagoon Volume Budget

The lagoon control volume is defined here using the 8 meter depth contour (Figure 3.1b, white line), determined from bathymetric data. The rate of change of the lagoon volume must be equal to the advective fluxes of water through the bounding control surfaces. Defining the net volume fluxes through the north and south channels and over the reef flat as F_{NCH}, F_{SCH}, and F_{RF}, respectively, the rate of change of the lagoon volume is,

$$\frac{dV_L}{dt} = \int_{A_I} v_A dA = \overline{v}_A A_I = F_{NCH} + F_{SCH} + F_{RF}. \tag{2.1}$$

V_L is the lagoon volume, v_A is the velocity of the flow through the lagoon flux faces where overbar denotes cross sectional averaging (Equation 2.3), the cross sectional area of the flux faces is A_I, and $\int_{A_I}$ is the area integral over the flux faces. Volume contribution due to precipitation and evaporation is also assumed to be negligible. The volume rate of change on the left side of Equation 2.1 can be represented as,

$$\frac{dV_L}{dt} = \frac{\Delta\eta_L}{\Delta t} A_S, \tag{2.2}$$

where η_L is the perturbation from the mean water depth obtained from pressure measurements at site NL (Figure 3.1b). In the lagoon, η_L varies primarily in response to tides. A correlation of all pressure sensors in the lagoon (NCH and SCH mooring, the SL and NL

moorings, and the east RF ADCP) shows a maximum lag of twelve minutes, which is much smaller than the 1-hr averaging time scale used in the volume and heat budget analyses, and therefore the tidal response inside the lagoon is considered uniform. The lagoon surface area, A_S, is defined by the 8 meter bathymetric contour.

The flux of water through the channels and over the reef flat is calculated by integrating v_A over the flux faces of the lagoon boundary (Figure 3.1c), where a positive flux is inward and we are neglecting cross-channel variation in flow.. The cross-sectional average velocity is calculated using width-weighted average velocities in 1-m vertical bins, where the weights are determined by the percent of the total cross-sectional area contained in each vertical bin:

$$\overline{v}_A = \sum_{i=1:n} \langle \overline{v}_i \rangle \frac{h_{bin} W_i}{A_I}, \tag{2.3}$$

where n is the total number of depth bins and $\langle\rangle$ denotes a 1-hr average. $h_{bin}W_i$ is the cross-sectional area of each bin, h_{bin} is the height of each bin (1 m) and W_i is the width of the flux face cross-section in each respective bin calculated from bathymetric data defined at the edge of the lagoon at each flux face and the time-variable depth. The volume flux through the channels is

$$F_{CH} = \overline{v}_{A,CH} A_{CH}. \tag{2.4}$$

$\overline{v}_{A,CH}$ is calculated from the 1-hour averaged velocity normal to the lagoon-channel boundary (ζ direction in Figure 3.1) vertically averaged within each 1-m depth bin. A_{CH} is calculated from the channel depth measured by the ADCP pressure sensors in the north and south

channel and bathymetric data. To fill in data gaps near the bed and at the surface that are not sampled by the ADCPs, bottom velocities are linearly interpolated to zero at the bed and the velocity in the top bin is extended to the surface.

Volume flux over the reef flat is defined as the sum of the volume fluxes in 16 reef sections, with local Cartesian coordinate system applied at each section, to resolve spatial variability in advective fluxes due to directional wind and wave forcing,

$$F_{RF} = \sum_{j=1:16} \overline{v}_{A,RF,j} A_{RF,j}, \tag{2.5}$$

where j represents each reef section (Figure 3.1c). $A_{RF,j}$ is the cross-sectional area of each reef section. Time-variable depth on the reef flat is calculated from the east reef flat ADCP pressure sensor (ERF in Figure 3.1b) with the assumption that depth is uniform along the lagoon-reef flat boundary. The 1-hr and cross-sectionally-averaged flow normal to the lagoon boundary for each subsection of the reef flat, $\overline{v}_{A,RF,j}$, is estimated by a model of reef flat transport from Reid et al. (2020).

Following Reid et al. (2020), the bathymetric slope over the reef flat is assumed to be small and the cross-sectionally-averaged velocity is estimated as the momentum due to wave radiation stress, wind stress, and the pressure gradient balanced by the quadratic bottom stress,

$$\langle \overline{v}_{A,RF,j} \rangle = sgn\left(-\frac{\Delta S_{\zeta\zeta,j}}{\rho C_{da} \Delta r_j} + \frac{\tau_j^{w\zeta}}{\rho C_{da}} - \frac{g \Delta \eta D}{C_{da} \Delta r_j} \right) \sqrt{\left| -\frac{\Delta S_{\zeta\zeta,j}}{\underset{(1)}{\rho C_{da} \Delta r_j}} + \frac{\tau_j^{w\zeta}}{\underset{(2)}{\rho C_{da}}} - \frac{g \Delta \eta D}{\underset{(3)}{C_{da} \Delta r_j}} \right|}, \tag{2.6}$$

where term (1) represents the flow over the reef flat driven by surface waves, term (2) represents the flow driven by wind stress, and term (3) represents flow driven by the tidally forced pressure gradient between the lagoon and open ocean. All terms are 1-hr averaged. The depth at the lagoon-reef flat boundary, D, is measured using the east reef flat ADCP pressure sensor and Δr is the width of the reef flat in the ζ-direction for each section, as calculated from the bathymetric data. The depth-dependent drag coefficient, C_{da}, which has been shown to be important on shallow coral reefs (Lentz et al., 2017; Davis et al., 2021), is defined as,

$$C_{da} = \kappa^2 \left\{ log\left(\frac{D}{z_0}\right) + (\Pi - 1) \right\}^{-2} \tag{2.7}$$

where $\kappa = 0.4$ is the Von Karmen constant, $\Pi = 0.2$ is the Cole's wake strength parameter, and the hydrodynamic roughness, $z_0 = 2.4$ cm, is an average of estimates on the Dongsha reef flat from Lentz et al. (2017). The incident wave radiation stress in shallow water is estimated via,

$$S_{\zeta\zeta,j} = \frac{\rho g H_{s,j}^2}{32} \left\{ (cos^2(\theta_{wave}) + 1)\frac{c_g}{c} - \frac{1}{2} \right\}, \tag{2.8}$$

where θ_{wave} is the wave direction, c_g is the group speed of the waves, and c is the wave celerity. From the shallow water assumption, $\frac{c_g}{c} = 1$. $H_{s,j}$ is the significant wave height for each reef flat section and is estimated from offshore significant wave height, H_s, and wave direction, θ_{wave}, obtained from ECMWF ERA5 1-hr data from a 30-km grid (Hersbach et al., 2020) as detailed in Equation 2.9 below. H_s inside the lagoon is assumed to be negligible (Reid et al., 2020); therefore, the spatial difference in radiation stress, term (1) in Equation

2.6, is equal to the radiation stress on the offshore side of the reef flat. Wave shoaling is not considered. To account for the refractive damping of a directional wave field, offshore wave height around the atoll is estimated using a simple geometric model,

$$H_{s,j} = H_s \left\{\cos^2(\theta_{wave})\right\} \quad [-\frac{\pi}{2} < \theta_{wave} > +\frac{\pi}{2}]. \tag{2.9}$$

In this model, the full incident offshore wave height predicted by ECMWF ERA5 1-hr data, H_s, is applied at the point on the forereef aligned with the wave direction and is decimated with distance around the forereef by applying a cos^2 function to $\pm\frac{\pi}{2}$ of the wave direction. A minimum wave height of 0.2 meters is applied based on observed wave data on the north and east forereef (Figure 3.1b) measured throughout the duration of the study. Estimated wave height using Equation 2.9 is well correlated with observed significant wave height from the AWAC at 20 m depth on the east forereef ($R^2 = 0.81$).

The wind stress is estimated as,

$$\tau_j^{w\zeta} = C_{d,wind}\rho v_{wind}^2, \tag{2.10}$$

where $C_{d,wind} = 1.1 \times 10^{-3}$ is the wind drag coefficient for wind speeds less than 6 ms^{-1} (Gill, 1982), and v_{wind} is the component of the wind velocity at 10 m height obtained from ECMWF ERA5 1-hr data that is aligned with the cross-reef direction (ζ) for each reef section.

The difference in sea surface height across the reef flat is estimated as,

$$\Delta\eta = \eta_L - \eta_O \tag{2.11}$$

which includes variations sea surface height due to tides and other low frequency processes. In Equation 2.11, η_O is measured from the bottom mounted ADCP on the 10 meter offshore mooring and η_L is measured at the pressure sensor (SBE-37) on the north lagoon mooring. Both pressure signals were band-pass filtered (4 to 60 hours). Analysis of pressure sensors on the forereef indicate that water levels around the exterior of the reef flat over the scale of the atoll are correlated at timescales less than our averaging period (1 hour). Therefore, $\Delta\eta$ is assumed to be the same for all reef sections. The reef flow model is validated by comparing the estimated cross-reef flow to the depth averaged flow recorded by the east reef flat ADCP, with an R^2 of 0.37 (Figure 2.2g).

This R^2 is significantly lower compared to the $R^2 = 0.88$ from Reid et al. (2020) using the same momentum model at a similar location on the east reef. Our pressure observations from this study show that during low spring tides the offshore pressures are hydraulically disconnected from the rest of the system, predicting a lagoonward flow forced by the pressure gradient term in the momentum budget that is not observed in the east reef flat observations. Additionally, we have more coarsely dispersed pressure measurements compared to the study in Reid et al. (2020), leading to further error in our calculations.

2.3.2 Lagoon Heat Budget

The total observed heat content of the lagoon, H_L, is,

$$H_L(t) = \rho c_p V_L T_L = \rho c_p V_L \sum_i \beta_i T_{L,i}, \tag{2.12}$$

where the heat capacity per unit volume, ρc_p, is assumed constant and equal to 4.1×10^6 J s m^{-3}C^{-1} and T_L is the volume-averaged water temperature in the lagoon. T_L is estimated by grouping the temperature sensors moored in the lagoon (including individual moored sensors and WireWalker profiles) and in the channels into variable sized depth bins. Then a horizontal, 2-dimensional spatial interpolation is applied to the temperature sensors within each bin. Bin heights are determined by the spatial distribution of temperature sensors in each bin. Next, a weighted vertical average of the temperature in each depth bin is calculated based on the hypsometric volume curve. In Equation 2.12 ,i represents depth bins in the lagoon, $\beta_i = V_{L,i}/V_L$ is a volume dependent weighting factor, $T_{L,i}$ is the interpolated temperature at each depth bin, and $V_{L,i}$ is the volume of each depth bin.

The rate of change of heat in the lagoon is due to the fluxes of heat through the bounding surfaces, and can be written as:

$$\frac{dH_L}{dt} = Q_A + Q_N, \tag{2.13}$$

where $Q_A = Q_{NCH} + Q_{SCH} + Q_{RF}$ is the sum of advective heat fluxes through the channels and over the reef flat and Q_N is the net surface heat flux. As noted for the volume flux calculation, we neglect any advective heat flux due to groundwater flow or precipitation.

Q_A can be written as

$$Q_A = \rho c_p \int_{A_I} v_A(\xi, z, t) T_A(\xi, z, t) dA, \tag{2.14}$$

where $T_A(\xi, z, t)$ is the water temperature at each flux face. Similar to v_A, T_A can be expanded into barotropic ($\overline{T_A}(\xi, t)$ cross-sectionally-averaged, done similarly in Equation 2.3) and baroclinic ($T'_A(\xi, z, t)$ depth-varying, with cross-sectional-average removed) components.

The net surface heat flux between lagoon and atmosphere is calculated as,

$$Q_N = (Q_E + Q_H + Q_S + Q_L) * A_S, \tag{2.15}$$

where Q_E is the latent heat flux, Q_H is the sensible heat flux, Q_S is the shortwave heat flux, and Q_L is the longwave heat flux. Q_E, Q_H, and Q_L are calculated via the COARE 3.0 (Coupled Ocean-Atmosphere Response Experiment) algorithm (Fairall et al., 1996, 2003) with observed meteorological data inputs from the Dongsha airport weather station and Dongsha Navy weather station; cool skin and warm layer corrections were not applied. Cloud coverage is obtained from ECMWF ERA5 1-hour data. Q_S is observed at the Dongsha airport weather station with albedo calculated via methods presented in (Taylor et al., 1996). Taylor et al. (1996) observes an average open ocean albedo of 0.06; however, on reef platforms and shallow lagoons, the average albedo has been observed to be higher, with average values of up to 0.16 and 0.12 on reef flats and in lagoons, respectively (McGowan et al., 2019). Dongsha Atoll lagoon is not only shallower than the open ocean, but it also contains hundreds of coral platforms that reach the near surface, increasing reflectance. To better represent the Dongsha Atoll lagoon system, we use an average albedo of 0.1, which is consistent with values observed in McGowan et al. (2019).

Setting the observed heating rate of the lagoon (Equations 2.12) equal to the heating rate of the advective and surface heat fluxes (Equations 2.13), gives,

$$\rho c_p T_L \frac{dV_L}{dt} + \rho c_p V_L \frac{dT_L}{dt} = \rho c_p \overline{v}_A \overline{T}_A A_I + \rho c_p \int_{A_I} (v_A{}' T_A{}') dA + Q_N, \tag{2.16}$$

where the first term on the left hand side is the change in heat due to the change in volume, and the second term on the left hand side is the change in heat due to the change in temperature. Moving the first term on the left hand side to the right and and applying conservation of mass for $\frac{dV_L}{dt}$ (Equation 2.1), gives,

$$\rho c_p V_L \frac{dT_L}{dt} = \underbrace{\sum_{n=1:3} \rho c_p \overline{v_A} \Delta T_A A_I}_{Q_{BT}} + \underbrace{\rho c_p \int_{A_I} (v_A{}' T_A{}') dA}_{Q_{BC}} + Q_N. \tag{2.17}$$

The first term on the right hand side is the barotropic advective heat flux (Q_{BT}), where i represents each flux face surrounding the lagoon (NCH, SCH, RF), the second term is the baroclinic advective heat flux (Q_{BC}), and the third term is the net surface heat flux.

ΔT_A is defined as,

$$\Delta T_A = \langle \overline{T_A} \rangle - \langle T_L \rangle. \tag{2.18}$$

Equation 2.17 is integrated in time to obtain the evolution of the lagoon-averaged temperature over the observational period. In the channels, the barotropic heat flux is calculated from

the difference between the cross-sectionally-averaged channel temperature and the lagoon-averaged temperature, as well as the cross-sectionally-averaged along-channel velocity. They are calculated from the 1-hr averaged, cross-sectional weighted water temperature and velocity, measured by the north and south channel moorings and ADCPs, respectively. The baroclinic heat flux in the channels is calculated from the depth-varying water temperature measured by the channel moorings, as defined in Equation 2.12, and the depth-varying velocity with axis aligned with channel geometry (into/out of the lagoon), measured by ADCPs at the north and south channels. North channel water temperature measurements miss the top three meters of the water column, and south channel water temperature measurements miss the top four meters of the water column. In order to better represent temperature stratification in the channels, the observed near-surface temperature stratification structure from the most westward CTD station (Figure 3.1b) is applied in the channels. The stratification structure is only applied during ebb tides. The CTD measurements are not continuous (approximately every 2 days), so the stratification structure is averaged for each spring and neap tide. During flood tide, when the channels temperature profiles are nearly homogeneous, the top bin with observed temperature measurements is extended to the surface.

We assume baroclinic heat fluxes on the reef flat to be negligible given strong bottom-driven mixing and shallow water depths (Reid et al., 2020). The barotropic heat flux over the reef is calculated from the difference in temperature between the reef and volume-averaged lagoon temperature, and the modeled cross-sectionally-averaged flow on the reef. Reef flat temperature is sampled by the east reef flat bottom mounted thermistor (Figure 2.2h) and assumed to be spatially homogeneous. The flow on the reef is from the modeled reef flat flow at each reef cross section, calculated in Equation 2.6.

LOCATION	**WATER DEPTH (m)**	**SENSORS**
North Channel (NCH)		
Fixed Vertical Mooring	8.8	2 temperature sensors at depths of 5.9 and 3 meters.
Bottom Mounted ADCP	8.9	1200 kHz Workhorse ADCP.
South Channel (SCH)		
Fixed Vertical Mooring	8.6	2 temperature sensors at 7.8 and 5.2 meters.
Bottom Mounted ADCP	8.2	1200 kHz Workhorse ADCP.
Lagoon		
Fixed Vertical Mooring North (NL)	17	5 temperature sensors at depths ranging from 13.2 to 3 meters; pressure at 3.6 meters.
Fixed Vertical Mooring South (SL)	19	4 temperature sensors at depths ranging from 16.3 to 4.8 meters.
WireWalker Mooring West (WWW)	17	Continuous sampling of temperature and pressure along depth.
WireWalker Mooring East (WWE)	16	Continuous sampling of temperature and pressure along depth.
Bottom Mounted Thermistors	Various	10 temperature sensors at depths ranging from 9.8 to 18.7 meters.
Reef Flat (RF)		
Bottom Mounted Thermistors	$\sim$2	1 temperature sensor at approximately 1 meter depth.
Bottom Mounted ADCP	1.8	1200 kHz Workhorse ADCP.
Offshore Moorings		
Fixed Vertical 10 meter mooring	10	5 temperature sensors at depths ranging from 9.75 to 2 meters; pressure at 2 meters.
Fixed Vertical 20 meter mooring	20	10 temperature sensors at depths ranging from 19 to 5.5 meters; pressure at 5.5 meters.

Table 2.1: Experiment Instrumentation

Variable	Description	Units	Variable	Description	Units
A_I	Cross-sectional area of the flux faces surrounding the lagoon	m^2	T_A	Water temperature at each lagoon flux face	°C
A_{RF}	Reef flat cross sectional area	m^2	$\overline{T_A}$	Cross-sectionally-averaged temperature at lagoon flux faces	°C
A_S	Lagoon surface area	m^2	T'_A	Cross-sectionally-varying temperature at lagoon flux faces	°C
β_i	Volume dependent weighting factor	%	$T'_{A,CH}$	Cross-sectionally-averaged, depth varying water temperature in the channels	°C
c	Wave celerity	ms^{-1}	T_f	Flushing time	days
C_{da}	Reef flat drag coefficient		T_L	Lagoon volume-averaged temperature	°C
$C_{d,wind}$	Wind drag coefficient		v_{wind}	10 m wind speed	ms^{-1}
c_g	Wave group speed	ms^{-1}	v_A	Flow through the lagoon boundaries	ms^{-1}
c_p	Heat capacity of water	$Jkg^{-1}K^{-1}$	$\overline{v_A}$	Barotropic velocity through lagoon boundaries	ms^{-1}
D	Water depth on reef flat	m	v'_A	Baroclinic velocity through lagoon boundaries	ms^{-1}
F_{CH}	Volume fluxes through the channels	m^3s^{-1}	$\overline{v_{A,CH}}$	Cross-sectionally-averaged velocity normal to lagoon-channel boundary	ms^{-1}
F_{RF}	Volume fluxes through over the reef flat	m^3s^{-1}	$v'_{A,CH}$	Baroclinic flow through the channels	ms^{-1}
h	Height of each channel depth bin	m	V_L	Lagoon volume	m^3
H_L	Lagoon heat content	W	W_{CH}	Width of each channel depth bin	m
h_0	Lagoon bed elevation above datum (deepest point in lagoon, 22 m)	m	z	Vertical coordinate, positive upwards	m
H_s	Significant wave height	m	z_0	Hydrodynamic roughness	m
Q	Cumulative volumetric flow rate into the lagoon	m^3s^{-1}	α	Least squares fitting coefficient	
Q_A	Advective heat flux	Wm^{-2}	ΔT_A	Temperature difference between advective component and lagoon	°C
Q_{BC}	Baroclinic heat flux	Wm^{-2}	Δr	Reef flat width in the cross-sectional direction	m
Q_{BT}	Barotropic heat flux	Wm^{-2}	η	Free surface elevation	m
Q_E	Latent heat flux	Wm^{-2}	η_L	Perturbation from mean water depth in lagoon	m
Q_H	Sensible heat flux	Wm^{-2}	η_O	Perturbation from mean water depth offshore	m
Q_N	Net surface heat flux	Wm^{-2}	κ	Von Karman constant	
Q_L	Longwave heat flux	Wm^{-2}	Π	Coles Wake Strength parameter	
Q_S	Shortwave heat flux	Wm^{-2}	θ_{wave}	Wave direction	deg
$S_{y'y'}$	Incident wave radiation stress	$kgms^{-2}$	$\tau^{wy'}$	Wind stress	kgm^{-3}
t	Time	hr	ρ	Density of water	kgm^{-3}

Table 2.2: Variable Descriptions and Units

2.4 Results

2.4.1 Oceanographic Conditions

Full and new moons occurred on 19 May and 03 June 2019, respectively, such that the first and last weeks of the study period (20-26 May and 04-10 June) were characterized by spring tidal conditions, while the second week of observations (27 May- 03 June) was characterized by neap tide conditions (Figure 2.2a). Tidal amplitude varied from 0.4 to 1.2 m meters during neap and spring tides, respectively (Figure 2.2a). Cloud coverage was highly variable except for a period of persistent high cloud cover from 25 - 29 May associated with precipitation events of 18 mm and 14 mm on 27 May and 29 May, respectively (Figure 2.2b). Winds were variable in magnitude but primarily directed to the north except near the start of the deployment from 20 - 23 May, when winds shifted to the southwest. The average wind speed was 2 $\mathrm{m\,s^{-1}}$ with gusts of up to 6 $\mathrm{m\,s^{-1}}$ (Figure 2.2c).

Offshore significant wave height, H_s, ranged from 0.4 m to 2 m, with the largest waves during the first half of the study period, peaking on 25 May. Subsequently, H_s decreased to an average of 0.5 m from 01-07 June, increasing again to 1.2 m from 08-09 June (Figure 2.2d). Wave direction was primarily from the east, except for 01-05 June and 09-10 June where waves were from the south (Figure 2.2e).

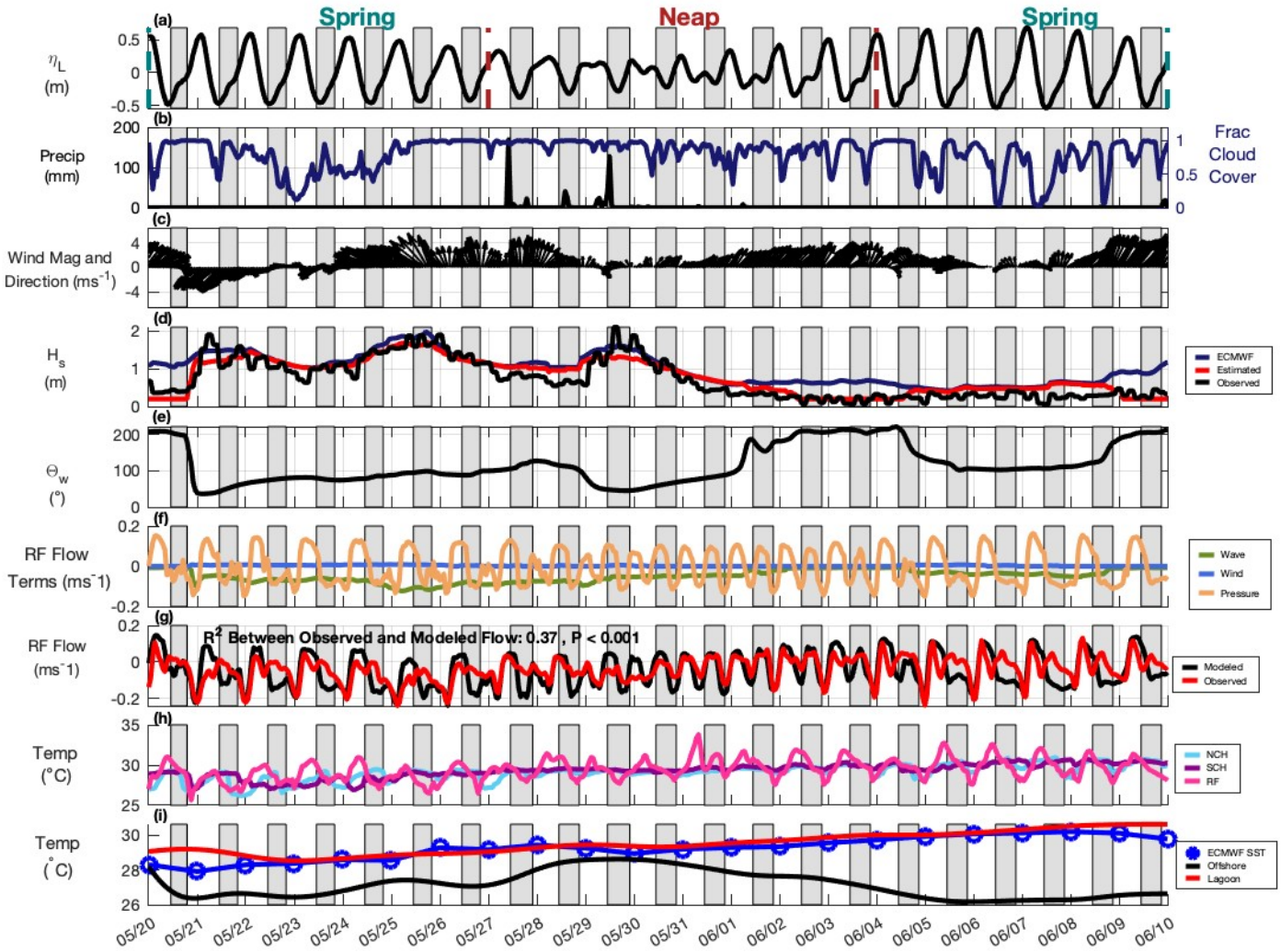

Figure 2.2: Oceanographic and meteorological data throughout deployment. a) Tidal water level from SBE37 on north lagoon mooring at 3.6 m depth, bandpass filtered from 4 to 60 hours. b) Precipitation from meteorological station located on Pratas island (left, black) and cloud coverage from ECMWF ERA5 (right, blue). c) Wind direction and magnitude from ECMWF ERA5 (upward north). d) Comparison of significant wave height measured by ADCP on the east reef (black) and ECMWF ERA5 (blue), and estimated by Equation 2.9 for east reef (red). e) Offshore wave direction from ECMWF ERA5 (0 degrees from the north). f) Terms in the reef flat flow (Equation 2.6) for the east reef. Orange: pressure-driven flow, blue: wind-driven flow, and green: wave-driven flow. All terms are 4 hr low pass filtered. g) Comparison of the depth averaged observed (black) and estimated flow (red) on the east reef, 4 hour low pass filtered. h) 4 hr low pass filtered, depth-averaged temperature in the north channel (blue), south channel (purple), and east reef flat (pink). i) 60 hr low pass filtered lagoon averaged temperature (red) and offshore temperature at the 10 m offshore mooring, at 4 m depth (black). Offshore surface temperature from ECMWF ERA5 (blue). Dark grey vertical shading indicates periods of night.

2.4.2 Lagoon Circulation

On average, subtidal (60-hour low pass filtered) circulation transports open ocean water into the lagoon over the reef flat and is balanced by flow out of the lagoon through the channels (Figure 2.3b). This subtidal circulation pattern is primarily driven by surface waves breaking on the reef crest, driving a net flow over the reef flat toward the lagoon (Figure 2.2f) (Reid et al., 2020). Water exchange over the reef flat and through the channels is also influenced by tides, varying on daily and fortnightly time scales (Figure 2.2f). The average subtidal transport over the reef flat and through the north and south channels yield 1.0 x $10^7 m^3 s^{-1}$, -3.9 x $10^6 m^3 s^{-1}$, and -2.6 x $10^6 m^3 s^{-1}$, respectively, with positive transport directed into the lagoon.The non-zero net transport is indicative of error in the estimates.

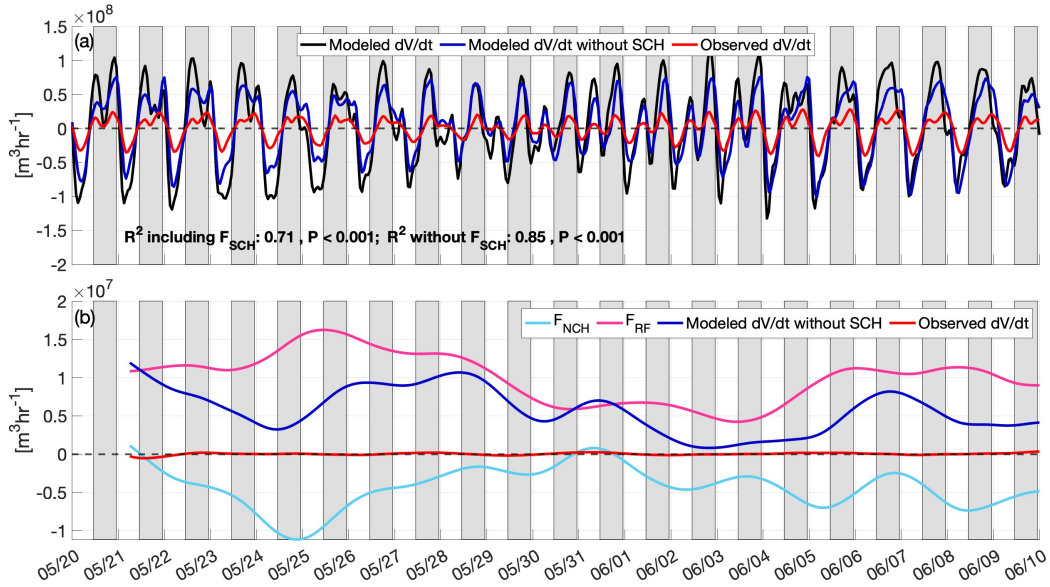

Figure 2.3: a) The 4 hr low-pass filtered (lpf) modeled volume budget, with the south channel (black) and without the south channel (blue), compared to the observed 4 hr lpf lagoon volume in red. b) The 60 hr lpf modeled volume budget without the south channel (dark blue), compared to the observed 60 hr lpf lagoon volume in red. The 60 hr lpf volume contributions from the north channel and reef flat are shown in light blue and pink, respectively. Black dashed line indicates zero.

There are uncertainties inherent in estimating a volume or heat budget of the lagoon system from a few moorings located in the channels and on the reef flat. In order to constrain the uncertainty in the volume budget, we consider a least squares approach for the advective fluxes on tidal timescales where we allow for adjustment to the flow rate measured at each site by a constant factor. The volume budget is written as,

$$\frac{dV_L}{dt} = \alpha_1 F_{NCH} + \alpha_2 V_{SCH} + \alpha_3 F_{RF}. \tag{2.19}$$

Here, we use the north channel as the reference site (setting $\alpha_1 = 1$) as it has the least complex bathymetry and we expect our measurements of currents are most representative. The least squares fit effectively minimizes α_2 to zero, the south channel volume flux term, and decreases α_3, the reef flat volume flux term, by two thirds. The south channel has complex bathymetry with wide, shallow edges and a deeper, narrow center. The estimated volume fluxes in the south channel have higher directional variability compared to both the north channel and reef flat volume fluxes. These observations, combined with the volume budget and least squares results, suggest that the observed south channel flow measurements are not representative of the flow across the entire south channel-lagoon boundary, likely leading to error in the volume and heat budgets. Further discussion of error is presented in the Discussion.

2.4.3 The Heat Budget

Dongsha Atoll lagoon experienced strong net heating over the three-week study period ($\sim$ 1.5°C). The lagoon warms similarly to sea surface temperatures offshore but notably, water temperature on the forereef surrounding the atoll does not show the same warming trend (Figure 2.2i), likely due to the influence of internal waves (Davis et al., 2020). Here, we

	Mean [°C]	**Standard Deviation** [°C]
Net Surface Heat Flux	$8x10^{-3}$	$2x10^{-2}$
Total Advective Heat Flux	$-2x10^{-3}$	$1x10^{-2}$
North Channel Advective Heat Flux	$-1x10^{-6}$	$9x10^{-3}$
South Channel Advective Heat Flux	$5x10^{-4}$	$6x10^{-3}$
Reef Flat Advective Heat Flux	$-6x10^{-3}$	$2x10^{-2}$

Table 2.3: Mean and Standard Deviation of Heat Fluxes

use a lagoon-averaged heat budget (Model of Exchange Between the Lagoon and Ocean, Lagoon Heat Budget section) to examine the processes leading to heating and cooling in the lagoon. Heat budget terms from Equation 2.13 are shown in Figure 2.5 (4-hr low pass filtered (LPF) terms in Figure 2.5a, 60-hr LPF in Figure 2.5c). The modeled lagoon heating rate is compared to the observed bulk heating rate in Figure 2.5b (4-hr LPF) and Figure 2.5d (60-hr LPF). The 4-hr LPF analytical heat budget predicts the daily heating rate of the lagoon system with an $R^2 = 0.47$ (Figure 2.5b) and a daily averaged $R^2 = 0.95$ (Figure 2.4). Additionally, Table 2.3 shows the mean and standard deviation for each term in the heat budget (Equation 2.13).

The primary contribution of heat to the lagoon system during the study period was from surface heat fluxes (which is primarily solar heating; Figure 2.5 a,c), explaining 68% of the variance in the total modeled heating rate. The only days with net lagoon cooling, 29-30 May, also had high cloud cover and precipitation (Figure 2.2b). Advective fluxes of water over the reef flat and through the north channel cool the lagoon (Figure 2.5c), with an average cooling rate of $-8x10^{-3}$ °C hr^{-1} and $-8x10^{-4}$ °C hr^{-1}, respectively. The south channel, on average heats the lagoon system with an average heating rate of $9x10^{-4}$ °C hr^{-1}. The south channel heating of the system is a result of the removal of cool water from the lagoon with little tidal modulation in the recorded south channel temperature and velocities compared to the north channel and reef flat. There is a persistently negative ΔT, meaning the south channel is almost always cooler than the lagoon, along with a net outward flow in the south channel.

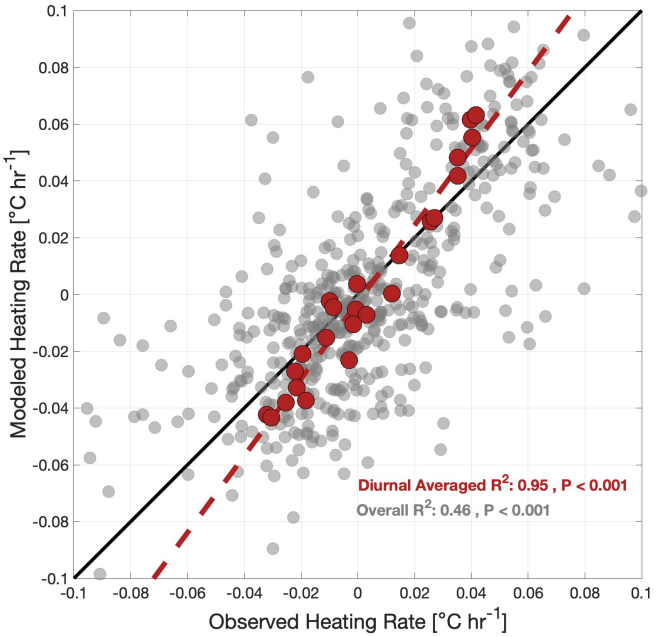

Figure 2.4: Scatter plot of observed and modeled heating rate on the x and y axis, respectively. The light grey points represent all data points. The dark red points represent the diurnally averaged heating rate. The dark red dashed line is the line of best fit for the averaged data. The black line is a 1:1 line for reference.

During spring tides, reef flat driven cooling of the lagoon is nearly three times as large as during neap tides (average cooling rate for spring and neap tides are $-1x10^{-2}$ °C hr^{-1} and $-3x10^{-3}$ °C hr^{-1}, respectively). Increased advective forcing during spring tide can drive strong cooling events, such as those observed on 20 May and 7-8 June (Figure 2.5a). This cooling is likely a result of fortnightly variability in both water temperature and flow on the reef flat. The transport of water across the reef flat is strongly forced by tides, as represented in the pressure gradient term of Equation 2.6 (Figure 2.2f), leading to stronger lagoonward flow during spring tides. The offshore water temperature is also cooler during spring tide (Figure 2.2i) due to internal wave-driven cooling (Reid et al., 2019), with colder water advected onto the reef from offshore. The phasing of the tidal currents and diurnal surface heating on the reef flat plays a key role in the cooling of lagoon waters and will be discussed further in the Discussion.

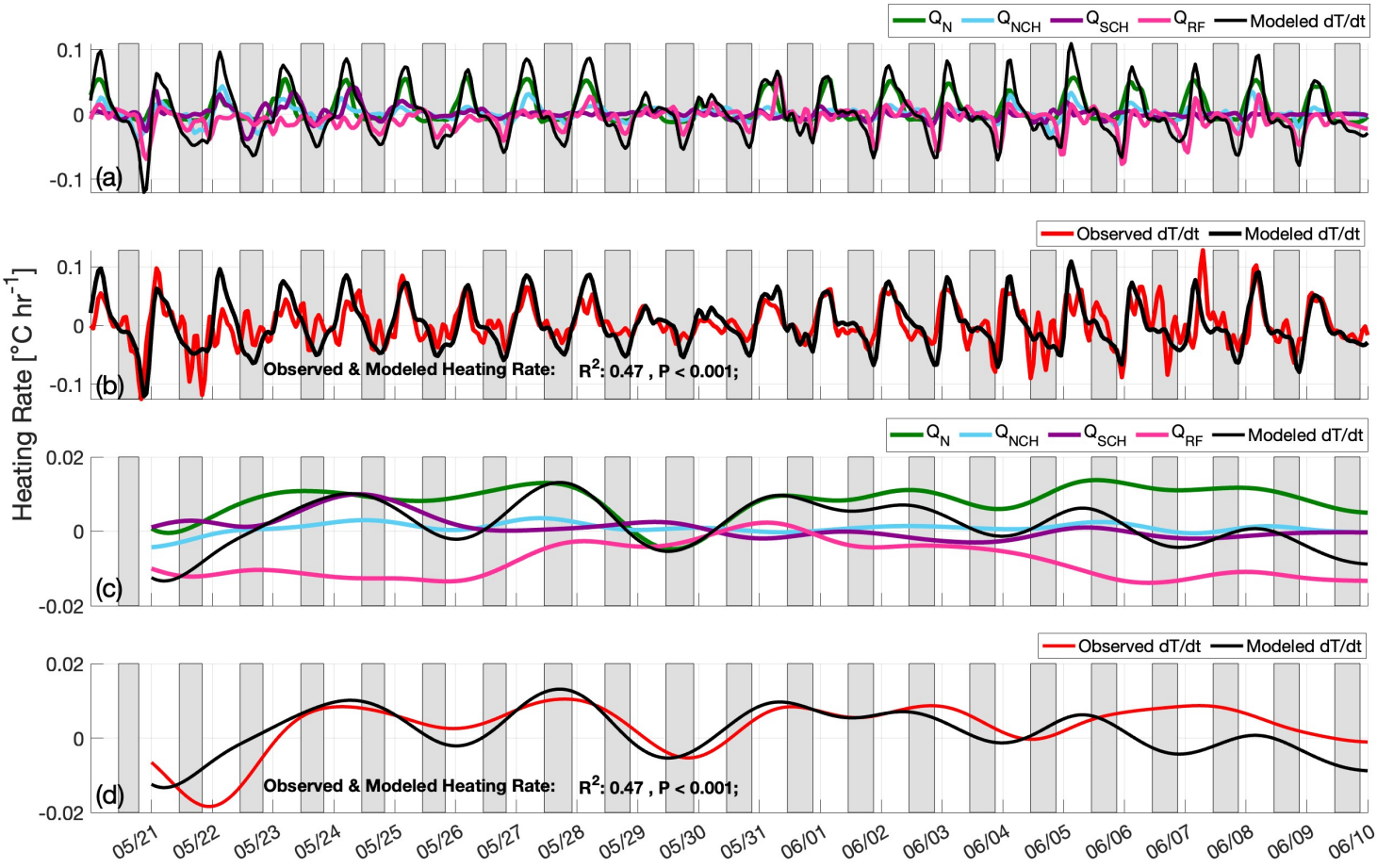

Figure 2.5: Lagoon spatially integrated heat flux. a) The 4 hour lowpass filtered heat budget terms. Modeled dT/dt (black), surface heat flux Q_N (green), north channel heat flux Q_{NCH} (blue), south channel heat flux Q_{SCH} (purple), and reef flat heat flux Q_{RF} (pink). Negative values indicate cooling of the lagoon system, while positive values indicate heating. Grey shaded areas represent night in local time and white indicates day. Time stamp is UTC. b) The total estimated lagoon heating rate from heat flux (Equation 2.17) in black compared to the observed lagoon heating rate in red. c) The 60 hour lowpass filtered heat budget terms. The first day of data is ignored due to the filtering edge effects. Modeled dT/dt (black), subtidal surface heat flux Q_N (green), subtidal north channel heat flux Q_{NCH} (blue), subtidal south channel heat flux Q_{SCH} (purple), and the subtidal reef flat heat flux Q_{RF} (pink). d) The 60 hour lowpass filtered estimated lagoon heating rate from heat flux (Equation 2.17) in black compared to the 60 hour lowpass filtered observed lagoon heating rate in red.

2.5 Discussion

2.5.1 Heat Budget Errors

The heat budget developed above indicates that the substantial warming of Dongsha Atoll lagoon observed during the study period was primarily driven by solar radiation, which was heating the lagoon faster than advective cooling through the channels and over the reef flat. This simple heat budget captures the general observed thermal characteristics of the Dongsha Atoll lagoon – an overall increase in lagoon temperature during the three-week observational period, fortnightly tidal modulation of lagoon heat content, and daily heating and cooling dynamics.

However, there are significant differences between the observed and modeled lagoon heat content over the long term. Other than the last four days of the study period, the model overpredicts the heating of the lagoon (Figure 2.6a,b), indicating, on average, either overestimation of the advective or surface heat flux terms and/or that the observations are biased towards areas in the lagoon that are not heating as quickly. Both are likely true; the latter because our static moorings (NL and SL) and profiling WireWalker moorings (WWE and WWW) did not measure the top two meters of the water column, the region most likely to experience the strongest heating. For example, CTD casts indicate increasing thermal stratification in the upper four meters of the water column throughout the study period, with an average measured temperature difference in the top four meters of the water column of 0.22°C. However, a CTD cast from 06 June, near the end of the study period, shows a temperature difference of ~ 2°C in the top one meter of the water column – which was not captured by our mooring-based observations and therefore is not included in our observed estimate of lagoon heat content. Our estimated observed lagoon heat content is thus likely biased low, especially in early June when wind and wave conditions were calm and the near surface water column was thermally stratified.

Sparse horizontal instrumentation likely also contributed to errors in the estimated observed lagoon temperature. We employ three methods of calculating the observed lagoon temperature to determine the sensitivity of the calculation to the sensors used. The first method is described in the Model of Exchange Between the Lagoon and Ocean section and is used in the results presented above. The second method is similar to the first, except the channel temperature sensors were not included in the average, only sensors within the lagoon. In the third method, the thermistors in each bin are not horizontally interpolated, but rather averaged horizontally and then vertically averaged based on the percent volume of each depth bin. Overall, the bulk averaged lagoon temperature did not prove to be highly sensitive to the method used, with method two and three resulting in $R^2 = 0.48$ and $R^2 = 0.51$, respectively, when compared to the modeled heat budget and method one resulting in an $R^2 = 0.46$. The first method was implemented in the analysis presented in this paper as it employs the greatest number of sensors per depth bin and accounts for the spatial distribution of the sensors.

There are two periods of cooling during the three week study period, one from 20-24 May, which is solely seen in the observations, not the model. The other, from 06-10 June, is a model-predicted cooling event which does not appear in the observations. During the first cooling period, on 22 May, when the residual is the largest, observations show a strong cooling event that is not captured by the model. This cooling event coincides with a shift in wave direction (to the west) together with an increase in significant wave height (Figure 2.2d,e). Internal waves were also observed to shoal shallower than 5m depth on the fore reef slope during this same period (Sinnett et al., 2022). While cold water transported over the reef flat and through the channels by wind, wave (surface or internal), and tidally driven currents should, theoretically, be captured by our analytical heat budget model, the estimates of advective heat fluxes rely on sparsely placed temperature sensors on the east reef flat (to represent the whole reef flat) and in the channels. Spatial variability in water temperatures on the reef flat or in the channels associated with these processes during this

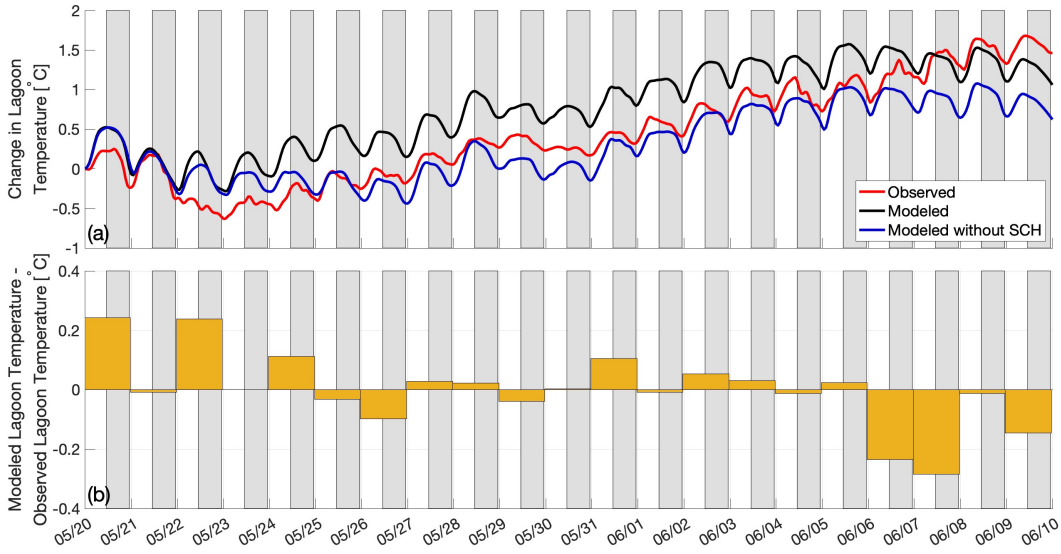

Figure 2.6: a) Net temperature gain in the lagoon during duration of study period in degrees C. The black line is the modeled heat gain with the south channel heat fluxes included, the blue line is the modeled heat gain without the south channel heat fluxes included, and the red line is the observed heat gain. b) Daily residual between the observed and modeled cumulative temperature with the south channel.

time period likely introduced cooling that was not captured by the sparse flux measurements used in our model.

Another source of error in the volume and heat budgets is associated with volume transport through the lagoon channels and over the reef flat. The second cooling event, between 06-10 June, the model gradually cools over the four day period, which is not seen in the observations. This event is likely due to an overestimation of volume and heat transport over the reef flat. Modeled currents are more frequently lagoonward compared to the observed flow, leading to an overestimation of volume flux (Figure 2.2g). This overestimation of lagoonward transport off the reef, coupled with the phasing of the diurnal solar cycle and tide on the reef, results in the strong modeled cooling deviating from the observations during this period (Figure 2.6a,b). Least-squares fitting Lagoon Circulation Results section indicated that the

placement of the moored current meter in the south channel was not providing information that was useful for constraining the observed changes in volume and heat content of the lagoon, likely due to its location near bathymetric irregularities in the channel. Furthermore, a recent modeling study of Dongsha Atoll lagoon (Chen, 2023) showed spatially variable flow in the south channel, in support of the hypothesis that the flow in the channel is too complex to be captured by a single point. By excluding the south channel heat flux in the heat budget, there is no significant change in the modeled hourly or cumulative heating rate, but there is a significant improvement in the lagoon volume budget (Figure 2.3a,b).

2.5.2 The Relative Importance of Waves, Tides in Driving Lagoon Cooling

Tidal forcing at Dongsha Atoll is primarily diurnal and, thus, nearly phase locked with the solar day during the three week study period, with flood tide at night and ebb tide during the day (Figure 2.7a, 2.7b, green). As tides are a dominant driver of flow over the reef flat (Results, Lagoon Circulation section), $\overline{v}_{A,RF}$ is primarily lagoonward at night. Due to the diurnal phasing of the tidal and solar cycle, this lagoonward flow advects water that has been cooled on the shallow reef flat into the lagoon. The resultant heat flux on the reef flat drives a persistent cooling of the lagoon at night, with a peak cooling at approximately 6 AM local time, corresponding with near maximum lagoonward reef flat flow and minimum reef flat temperatures (Figure 2.7c). Wave-forced advection over the reef flat, however, is not diurnally variable at this site and so transports both sun-warmed and cooler waters into the lagoon.

In order to understand the importance of waves compared to tides in driving these cooling events, we employ a simple thought experiment. We set either the wave (term 1, Equation 2.6) or pressure gradient (term 3, Equation 2.6) term to zero in the reef flat momentum

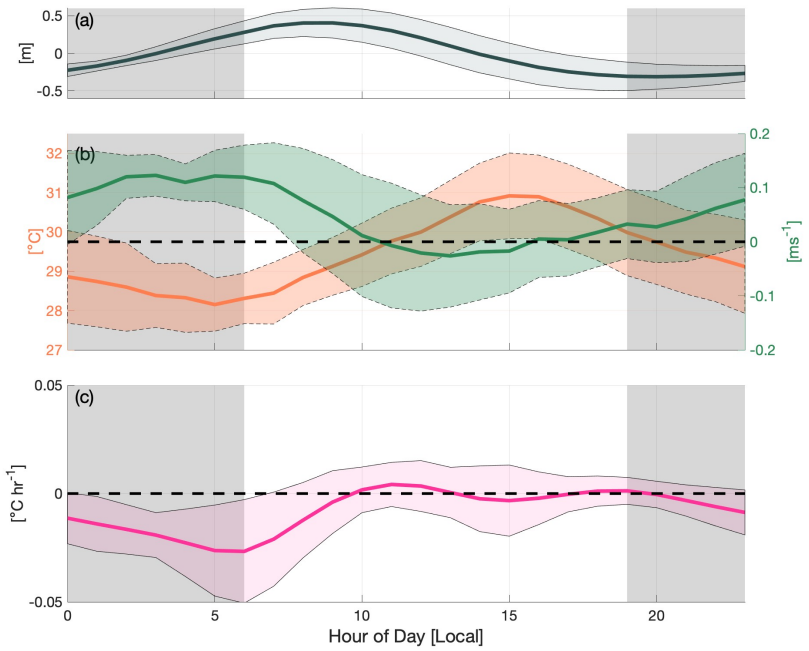

Figure 2.7: All plots show a daily composite average of each respective term for the entirety of the study period. a) 4 to 60 hour bandpass filtered, tidal water level from SBE37 on the north lagoon mooring at 3.6 m depth. b) 4 hr low pass filtered, daily averaged east reef flat temperature (orange) and estimated reef flat velocity v_{RF} (green). c) 4 hr low pass filtered, daily averaged east reef flat heat flux. Grey regions indicate night. Lightly shaded colored regions indicate the range of one standard deviation from the mean.

budget and calculate the cumulative cooling over the study period that is driven by reef flat advection. We find that when wave forcing is neglected tidal forcing on the reef flat alone cools the lagoon by 2.98°C over the study period, over three times greater than the cooling driven by waves alone (cumulative cooling of 0.90°C). This analysis, though not dynamically consistent (since wave, tide and friction forcing are linked), illustrates that relative to waves, tides are the primary driver of cooling over the reef flat due to the alignment of flood tides with night hours.

2.5.3 Flushing Time Estimate

Given the observations of low oxygen in the lagoon waters of Dongsha Atoll (Gajdzik and DeCarlo, 2017), it is desirable to understand more about the rate of flushing of the lagoon. The flushing time, T_f, is an integrative measure of the renewal time of water in a defined system, calculated as the volume of water (V) divided by the volumetric flow rate (Q) through the system (Monsen et al., 2002),

$$T_f = \frac{V_L}{Q}. \tag{2.20}$$

Here, V_L is the lagoon volume, and Q is the overall volumetric flow rate into the lagoon through the channels and over the reef flat. Calculated in this way, the average flushing time for Dongsha Lagoon is 2.9 days during the study period. On average, the reef flat flushed 19% of the total lagoon volume each day, while the north and south channels replenish 8% and 7% of the total lagoon volume, respectively. As with the heat content of the lagoon, the flushing time varies on fortnightly timescales. The flushing time for spring tide periods (average of the first and third weeks of the time series) is 2.7 days, but 3.2 days for the neap tidal regime in the second week of observations. These are similar in magnitude to flushing times calculated by modeling work from Chen (2023).

For the duration of the study period, barotropic tides are the primary driver of mass exchange between the lagoon and ocean. Though Chen (2023) concludes that winds and waves are the primary drivers of circulation inside Dongsha Atoll lagoon, our study coincides with a period of relatively low winds and waves. Similar to results from Reid et al. (2020), pressure-driven flow is the dominant term in the momentum budget over the reef flat, accounting for 71% of the average reef flat flow over the study period. Due to the relatively small (average < 1 m) significant wave height during the study period, the pressure gradient term in the momentum

budget is primarily due to tides (Reid et al., 2020). Wave radiation stress accounts for 26% of the total reef flat flow, and winds only account for 2% of the flow. Barotropic volume exchange through the channels is modulated by the spring-neap and ebb-flood tidal cycles and is an order of magnitude greater than the baroclinic exchange. Although surface waves may also increase transport through the channels, the tidal signal is dominant in the observed flow.

2.5.4 Consequences for Hypoxia in Dongsha Atoll Lagoon

The rapid warming observed in Dongsha Atoll lagoon during the study could have implications for oxygen availability in the system, as most documented hypoxic dead zones are in regions that are expected to warm 2 °C due to climate change by the end of the century (Altieri and Gedan, 2015). In a study of eleven hypoxia driven mass mortality events across Pacific atoll lagoons, ten of them occurred during warm seasons (Andréfouët et al., 2015). During 2014, a significant hypoxic event was observed in the northwest corner of Dongsha Atoll lagoon, causing seagrass die off and fish kills (Gajdzik and DeCarlo, 2017). This event occurred during a strong El Niño, associated with high sea surface temperatures and relatively calm wave and wind conditions, potentially leading to increased stratification, increased bottom water residence time, and eventually hypoxia. Warming water temperatures pose a multifaceted challenge to coastal marine ecosystems. Increased water temperatures reduce the oxygen solubility of water and can also lead to an increase in biological respiration rates, putting stress on the oxygen availability in a system (Vaquer-Sunyer and Duarte, 2011). As sea surface temperatures continue to rise, hypoxic events as seen in Dongsha Atoll lagoon could become more frequent and widespread on reefs across the globe (Andréfouët et al., 2015).

Freshwater discharge and anthropogenic pollution are common drivers of coastal marine

hypoxia (Altieri and Gedan, 2015). Dongsha Atoll lagoon, however, is a remote marine protected area with minimal nutrient pollution and limited freshwater sources (precipitation only). This lack of conventional hypoxia–inducing processes coupled with the relatively fast flushing times creates an unusual environment for the formation of low oxygen. The reef flat contributes the greatest volume of water to the lagoon system (Figure 2.3b), and previous studies have shown that the reef flat can become hypoxic on diurnal time scales (DeCarlo et al., 2017a), creating a possible mechanism for the advection of low oxygen water into the lagoon. This motivates further work to understand the physical processes influencing oxygen dynamics inside Dongsha Atoll lagoon.

2.6 Conclusion

Over a three week study period spanning mid May through early June 2019, the Dongsha Atoll lagoon heated nearly 1.5°C largely due to solar insolation. The bulk thermal dynamics of the lagoon are represented using a simple heat budget which includes surface heat fluxes, barotropic heat fluxes over the reef flat and through the channels, and baroclinic exchange through the channels. While shortwave radiation is the primary source of heating inside the lagoon, it is balanced by barotropic advective cooling over the reef flat and through the channels. The phasing of the diurnal solar cycle and tides for this time period advects cool water off the reef flat and into the lagoon at the end of the night. This phasing creates a mechanism for persistent nighttime cooling of the lagoon through reef flat advection. When comparing the relative importance of waves and the pressure gradient (primarily tides) in driving this cooling, it was found that the pressure gradient drives three times greater cooling compared to waves.

A volume budget shows a net transport of water into the lagoon off the reef flat, balanced by a net outflow through the north channel. While tides are the primary driver of flow over

the reef flat and through the north channel, increased transport over the reef flat is observed during periods of stronger wave forcing. We use the volume budget to estimate flushing timescales, which vary between 2.7 and 3.2 days between spring and neap tides, respectively.

The heat and volume budgets capture the physical processes controlling circulation inside Dongsha Atoll lagoon for our measurement period and highlight relatively short flushing timescales for a system in which low oxygen has been observed. These observations coupled with limited anthropogenic and freshwater inputs motivate further work to understand the physical drivers shaping the lagoons biogeochemical environment and enhance our understanding of hypoxia in the coastal tropics.

Chapter 3

Physical processes shaping low-oxygen events in a highly flushed coral atoll lagoon

3.1 Introduction

Over the past 50 years, oxygen levels in the open ocean have decreased an estimated 2%, with projections of an additional $3.2 - 3.7\%$ by the end of the next century, resulting in the expansion of oxygen minimum zones (Breitburg et al., 2018; Keeling et al., 2010; Bopp et al., 2013; Kwiatkowski et al., 2020). In the coastal ocean, reported hypoxic sites have increased exponentially since the 1960s and are associated with a surge of fish kills, sea grass die offs, coral bleaching events, and dead-zones (Vaquer-Sunyer and Duarte, 2008; Altieri et al., 2017; Gilbert et al., 2010; Zhang et al., 2010). Hypoxia is defined as oxygen concentrations ≤ 2 mg L^{-1}, though recently work has shown negative effects of sublethal low oxygen thresholds between 4-5 mg L^{-1} (Vaquer-Sunyer and Duarte, 2008; Nilsson et al.,

2010; Pezner et al., 2023). Despite extensive research to understand hypoxia in temperate coastal regions, there is a critical knowledge gap in understanding hypoxia in shallow tropical waters (Rabalais et al., 2010b; Diaz, 2001). A global literature review conducted by Altieri et al. (2017) shows that tropical dead zones are dramatically under reported. Further, within the already understudied topic of hypoxia in the tropics, there is a significant lack of focus on tropical lagoons and embayments. While nutrient levels can impact water quality and oxygen availability (Fabricius, 2005), physical controls such as circulation, stratification, and residence time of coastal water play a critical role in hypoxic events in shallow waters.

Coastal systems comprising of enclosed basins with restricted exchange with the open ocean, such as estuaries and fjords, are commonly susceptible to hypoxia. Density stratification may further isolate bottom water from air-sea gas exchange and create the physical conditions conducive to hypoxia (Fennel and Testa, 2019; Farmer and Freeland, 1983). Hypoxia can be relieved through vertical mixing, which is commonly driven by wind, tides, or convective cooling (Stanley and Nixon, 1992; Boesch and Rabalais, 1991; Kemp et al., 2009a). Additionally, advective inflow from rivers or deep water renewal from the open ocean can refresh isolated bottom waters. Deep water renewal events, which typically transport dense, higher oxygen water to depth, have been primarily observed in fjords (Gade and Edwards, 1980), but a recent study observed this mechanism in a tropical embayment (Adelson et al., 2022).

This study focuses on Dongsha Atoll, a semi-enclosed coral atoll located in the South China Sea. In summers 2014 and 2015, suspected hypoxia related fish kills and sea grass die offs were observed inside the lagoon and on the surrounding wide reef flat (Gajdzik and DeCarlo, 2017). Previous work from the same study period used a bulk lagoon heat budget to better understand drivers of observed warming events inside the lagoon and lagoon-ocean exchange (Merrigan et al. (b), in review). The study found average lagoon-wide flushing timescales of 3 days (Merrigan et al. (b). Additionally, Dongsha Atoll Lagoon is geographically isolated with limited anthropogenic eutrophication and an average daily dissolved oxygen range of

$\sim$1.5 mg L^{-1}, defining a system that is relatively absent of the conventional physical and biological mechanisms that form hypoxia (Kemp et al., 2009a). To better understand the physical processes controlling oxygen dynamics within Dongsha Lagoon, we construct a mass budget for the bottom waters of to estimate the residence time, which may be longer than the lagoon-wide average previously estimated, as well as the magnitude and frequency of bottom water renewal events.

3.2 Methods

3.2.1 Field Site

Dongsha Atoll is a coral atoll located in the South China Sea (Figure 3.1a). It is characterized by a central lagoon with a diameter of 28 kilometers and a surface area of approximately 600 km^2. The average depth of the lagoon is 10 m with depths of up to 21 m and coral columns extending up to 1 m from the surface. The lagoon is surrounded on the east, north, and south by a wide reef flat up to 3 km across (Figure 3.1b). The reef flat is continuously submerged with an average depth of one meter and a benthic community consisting of fleshy algae, sea grass, and live coral which modulate reef flat oxygen production and consumption (DeCarlo et al., 2017b). To the west, the lagoon is flanked by a north and south channel, with average depths of 8 and 11 m, respectively, separated by Pratas Island (Figure 3.1b).

3.2.2 Experiment

This analysis focuses on velocity, temperature, salinity, and oxygen measurements inside Dongsha Atoll lagoon and in the surrounding channels and reef flat. Meteorological conditions were measured at the airport located on Pratas Island. Measurements include precipi-

Depth [m]	Percent of total lagoon volume	Instrument Location
11	6.1	WWW, WWE, SW, S, N, NW, SW, NL, SL
12	5.41	WWW, WWE, NL, SL
13	4.75	C, NL, SL
14	3.94	NL, SL
15	2.94	NW, SL
16	1.75	*NW, SL*
17	0.67	*NW, SL*
18	0.15	*NW, SL*
19	0.04	*NW, SL*
20	0.02	*NW, SL*
21	0.004	*NW, SL*

Table 3.1: Table of instrument location per depth bin within the bottom volume of the lagoon. Italics denote depth bins where instruments were extrapolated due to lack of instrumentation. All instruments listed measure temperature with WWW and WWE also measuring salinity.

tation and shortwave radiation sampled at 1-minute intervals. Offshore conditions including wind speed, wind direction, significant wave height, and direction were obtained from the European Center for Medium-Range Weather Forecasts (ECMWF) ERA5 1-hour data on a 30-km grid (Hersbach et al., 2020).

Water temperature in the lagoon was measured with bottom moored thermistors at nine locations around the lagoon (Figure 3.1b) and on two fixed vertical moorings in the north (NL) and south (SL) lagoon with sensors at depths from 1.5 to 14 meters above the bed (Table 3.1). Water temperature was measured in both the north channel (NCH) and south channel (SCH) on fixed vertical moorings with sensors at depths from 0.4 to 5.6 meters above the bed (Figure 3.1). Temperature sensors used in the experimental array include RBR Concerto sampling at 5 Hz, Seabird Electronics SBE-37s (conductivity, temperature, pressure) sampling at a 1 minute interval, SBE-56s and RBR soloTs sampling at 1 second (all measuring temperature to ± 0.002°C), HOBO U22 Water Temp Pro sensors sampling at 1 minute intervals (bottom moored thermistors; measuring temperature to ± 0.2°C), and JFE RINKO W sensors sampling at 15 minute intervals (bottom mounted, measuring

temperature to ± 0.02°C). Water temperature was measured on the east reef flat with a bottom moored RBR-soloT sampling at 1 second intervals (RF in Figure 3.1b). Thermistors were calibrated using a linear offset determined from a pre-deployment calibration bath. Corrected temperatures are within 0.055 °C.

Two vertically profiling moorings with depth ranges from the surface to 12 m (WireWalkers, Rainville and Pinkel (2001)) measure temperature and salinity, one in the west lagoon (WWW) with a RBR Concerto sampling at 5 hertz and in the east (WWE) with a Seabird Electronics SBE-37s (conductivity, temperature, pressure) sampling at a 1 minute interval. Oxygen measurements are located on nine bottom mounted sensors on the reef and inside the lagoon measured by JFE RINKO W sensors sampling at 15 minute intervals.

Water velocities were measured by three 1200kHz Teledyne RDI Workhorse Acoustic Doppler Current Profilers (ADCPs), one in the north channel, one in the south channel, and one on the east reef flat, all sampling at 2-second intervals (Figure 3.1b). Pressure in the lagoon was recorded by a SBE-37 on the north lagoon mooring, reef flat pressure was recorded by the east reef flat ADCP and offshore pressure by a bottom mounted ADCP located on the 10 m mooring on the east forereef, outside of the lagoon (Figure 3.1b).

3.2.3 Conservation of Mass for Lagoon Bottom Waters

The following analysis considers a control volume of the lagoon bottom water. Here we describe the calculation of the observed bottom volume density and the modeled mass budget inside the control volume.

We define the upper-bound of the bottom volume to be the 11 m isobath from mean sea level, and the lower-bound as the lagoon bed, a volume that encompasses approximately 25% of the total lagoon volume. The bottom volume density, ρ_B, is calculated from the observed average

bottom volume temperature and salinity using the Gibbs-SeaWater Oceanographic toolbox (McDougall and Barker, 2011). The average bottom volume temperature is calculated as,

$$T_B = \sum_{n=11:22} \beta_n T_n, \tag{3.1}$$

where n denotes depth bins inside the lagoon bottom volume in one meter increments from the surface of the bottom water control volume to the bottom of the lagoon and $\beta_n = V_{B,n}/V_B$ is a volume dependent weighting factor. T_n is the horizontally-averaged temperature in each depth bin, calculated by linearly weighting temperature measurements from i sensors in each bin based on their distances from the center of the lagoon:

$$T_n = \frac{1}{i} \sum_{i} (a(x_0 - x_i) + b(y_0 - y_i) + T_i), \tag{3.2}$$

where x_0 and y_0 are the coordinates of the center of the lagoon, x_i and y_i are the coordinates of the temperature sensor, and T_i is the temperature recorded by sensor i. The coefficients a and b are calculated from a linear plane fit of all temperature measurements in each depth bin at each time step. Temperature measurements from WWW, WWE, NL, SL, and bottom mounted thermistors capture temperatures in the 11 through 15 m depth bins. For depths 16 m and below, which account for 5% of total lagoon volume, the deepest sensors (NW bottom mounted thermistor and SL mooring bottom thermistor) are extended to the bed and averaged to obtain the average temperature at those depths (Table 3.1).

The bottom volume average salinity is calculated from averaging salinity measurements on WWW and WWE, which measure salinity in the 11 and 12 m depth bins.

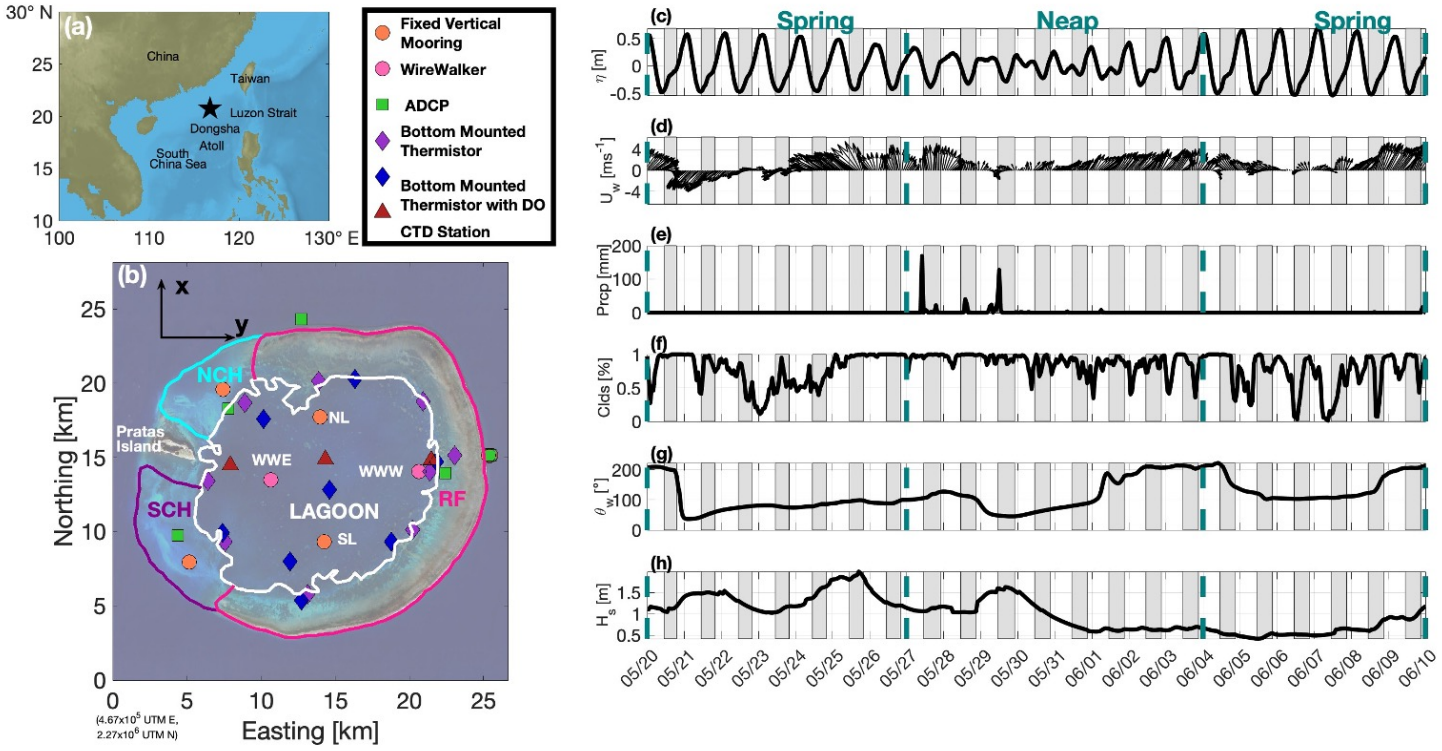

Figure 3.1: a) Map with location of Dongsha Atoll in the South China Sea with instrument locations during the 2019 lagoon experiment. The white lagoon outline is defined by an 8 meter bathymetric contour. Reef Flat (RF), North Channel (NCH), and South Channel SCH) outlines are approximate. (c) - (h) show oceanographic and meteorological data throughout deployment: c) tidal water level from SBE37 on north lagoon mooring at 3.6 m depth, band-pass filtered from 4 to 60 hours. d) Wind direction and magnitude from ECMWF ERA5 (upward north). e) Precipitation from meteorological station located on Pratas Island. f) Cloud coverage from ECMWF ERA5. g) Offshore wave direction from ECMWF ERA5 (0 degrees from the north). d) Significant wave height from ECMWF ERA5 and e) Offshore wave direction from ECMWF ERA5 (both 0 degrees from the north).

The conservation of volume of the lagoon bottom water is expressed here as a balance between dense water inputs through the lagoon channels and over the reef flat and the resulting vertical displacement of less dense water through the top area of the control volume,

$$\frac{dV_B}{dt} = \int^{S_A} \overline{u}_{CH} dA + \int^{S_A} \overline{u}_{RF} dA - wA_I = 0. \tag{3.3}$$

The first term on the right-hand-side of the equation is the volume contribution from the channels integrated over the surface area of the lagoon-channel interface, where $\overline{u}_{CH}$ is the cross-sectionally averaged velocity through the north and south channels, defined as positive (lagoonward) only; flow out of the lagoon is set to zero, as we assume water transported out of the lagoon through the channels and over the reef flat is surface lagoon water (Merrigan et al. (b), in review). S_A is defined as the cross-sectional where ρ_{CH} and ρ_{RF}, the density in the channels and on the reef flat, are greater than the ambient bottom water density, ρ_B. The second term on the right-hand-side of the equation is the volume contribution over the reef flat integrated over the surface area of the reef flat-lagoon interface, where $\overline{u}_{RF}$ is the cross-sectionally averaged velocity over the reef flat, as modeled in Merrigan et al. (b) (in review). The volume fluxes through the channels and over the reef flat only contribute to the bottom volume when flow is both lagoonward and the density of the inflowing water is greater than the density of the ambient bottom water. The third term on the right hand side of Equation 3.3 is the upward displacement, and is defined as,

$$w = \frac{\int^{S_A} \overline{u}_{CH} dA + \int^{S_A} \overline{u}_{RF} dA}{A_I}, \tag{3.4}$$

where A_I is the surface area of the interface between the bottom volume and the surface

volume of the lagoon (11 m depth). The velocities in the channels are measured by ADCPs in the north and south channels, respectively; the recorded velocities are 1-hour averaged and rotated normal to the lagoon-channel boundary in 1-m depth bins. Flow over the reef flat is modeled following Reid et al. (2020) modeled from local tidal, wave, and wind-driven transport as done in Merrigan et al. (b) (in review) for this same experiment. Details of the reef flat transport model are not repeated here, but the model accounted for 37% of variance in observed flow on the east reef over the study period. Density of water in the north channel is calculated from 1 m binned temperatures from the north channel mooring and salinity from the SBE-37 located 5.2 meters above the bed on the north channel mooring. Density of water in the south channel is calculated from 1 m binned temperatures from the south channel mooring and, due to lack of salinity measurements in the south channel, salinity was assumed to be the same as the north channel. Density of the water on the reef flat is calculated from temperature on the east reef flat and salinity measured by an SBE-37 on the 10 m mooring just offshore of the east reef flat. Density around the reef flat is assumed to be homogeneous both horizontally and vertically. This introduces some additional error though examine the correlation between the east reef flat thermistor (2.5 m depth) with a thermistor at 4.5 m on the south reef shows a reasonable correlation with an $R^2 = 0.44$.

Least squares coefficients from the bulk lagoon volume budget constrained in Merrigan et al. (b) (in review) for the same study period are applied to the volume fluxes in this study as described later.

The conservation of mass for the lagoon bottom volume can be written as,

$$V_B \frac{d\rho_B}{dt} = \underbrace{\int^{S_A} \rho_{NCH} \overline{u}_{NCH} dA}_{1} + \underbrace{\int^{S_A} \rho_{RF} \overline{u}_{RF} dA}_{2} - \underbrace{\rho_B w A_I}_{3} - \underbrace{F_D \frac{d\rho}{dz} A_I}_{4} + \underbrace{\alpha \frac{I(z) A_I}{c_p}}_{5}. \quad (3.5)$$

The left-hand-side of Equation 3.5 is the change in mass inside the bottom volume with respect to time. The first and second terms on the right-hand-side of Equation 3.5 represents the mass flux through the north channel and over the reef flat. The third, fourth, and fifth terms represent mass fluxes due to vertical displacement of ambient bottom water, vertical mixing and, solar heating at depth, respectively. The calculation of the first three terms, volume and density measurements in the channel and over the reef flat, as well as the vertical displacement and ambient bottom water density, are described above in Section 4.23.2.3. $\frac{d\rho}{dz}$ is the density gradient across the bottom volume-surface volume interface and is discretized as $\frac{\Delta\rho}{\Delta z}$ with a Δz of 0.5 m. F_D is the vertical diffusivity, estimated from a simple 1D salt budget of the bottom volume during a period of restricted advective contribution from 26 through 29 May,

$$F_D = -\left(\frac{dS}{dt}H\right)\left(\frac{1}{\frac{dS}{dz}}\right), \tag{3.6}$$

where $\frac{dS}{dt}$ is the change in salinity over the 3 day time period of low advection, and H is the average depth of the bottom volume, 3 m. $\frac{dS}{dz}$ is the average vertical salinity gradient across the bottom volume-surface volume interface and and is discretized as $\frac{\Delta S}{\Delta z}$ using observed salinity measurements from WWW spatially averaged in 0.5 m bins the vertical with a Δz of 0.5 m. Salinity measurements are from WWW due to the sparse temporal resolution of WWE. From this analysis, we obtain an average F_D value of 2x10^{-4} m^{2}s^{-1}, which is applied for the entire duration of the study period.

In the last term of Equation 3.5 which estimates the density change due to radiative heating of bottom waters, α is the coefficient of thermal expansion and c_p is the specific heat of water in Jkg^{-1}K^{-1}. The exponential decay of light intensity with depth is modeled using Beer's Law (Knauss, 1978),

$$I(z) = I_0 e^{-kz}, \tag{3.7}$$

where I_0 is the surface solar radiation obtained *via* ECMWF ERA5, z is the depth of the bottom volume, 11 m. We use uncalibrated PAR profiles, located on WWW, and calculate an e-folding time to estimate the average daytime Secchi depth for the study period. k is then estimated from this average depth using the formula $k = 1.7/S_d$ (Poole and Atkins, 1929).

All terms in the bottom mass budget are interpolated onto a 1-hour timestep and are 4-hour lowpass filtered.

3.3 Results

3.3.1 Oceanographic Conditions and Previous Work

The study period encompasses two spring tidal periods the first (20-26 May) and last (04-10 June) week of the study with neap tidal forcing 27 May through 03 June. Tidal amplitude ranged from 0.4 m to 1.2 m between neap and spring tides, respectively (Figure 3.1c). Wind was from the north at the beginning of the study period and shifted from the south on 23 May with an average wind speed of 2 $\mathrm{m\,s^{-1}}$ with gusts of up to 6 $\mathrm{m\,s^{-1}}$ (Figure 3.1d). Cloud coverage is variable except a period of high coverage 25-29 May, corresponding to precipitation events on 27 and 29 May with magnitudes of 18 mm and 14 mm, respectively (Figure 3.1e,f). Wave direction was primarily from the east, except for 01-05 and 09 June when direction shifts from the south (Figure 3.1g). Significant wave height ranges from 0.4 m to 2 m with largest wave magnitude on 25 May, decreasing to an average of 0.5 m 01-07

June before increasing to 1.2 m on 08 June (Figure 3.1h).

Merrigan et al. (b) (in review) constructed a bulk volume and heat budget for Dongsha Atoll lagoon for the same study period presented in this paper. This study showed a strong heating trend of approximately 1.5 °C over the 22 day study period, largely driven by surface heat fluxes. Advective transport out of the lagoon through the channels was balanced by inflow over the reef flat. This reef flat inflow was found to be the primary source of cooling in the system, driven by the phasing of the primarily diurnal tides and diurnal solar forcing. In order to close the bulk lagoon volume budget, the study applied a least squares approach to determine constant multiplier coefficients in order to account for uncertainties in the flow estimates. The north channel factor was held constant and the least squares fitting reduced the reef flat volume flux by a factor of two-thirds, while the south channel volume flux was minimized to near zero. This aligned with observations of velocity in the south channel, which do not show strong directionality or magnitude. The south channel is bathymetrically complex and our velocity measurements are likely not representative of fluxes along the entirety of the lagoon-south channel interface. This complex circulation inside the south channel is also reported in a recent modeling study of the system (Chen, 2023). These least squares coefficients are applied to all volume fluxes in this study.

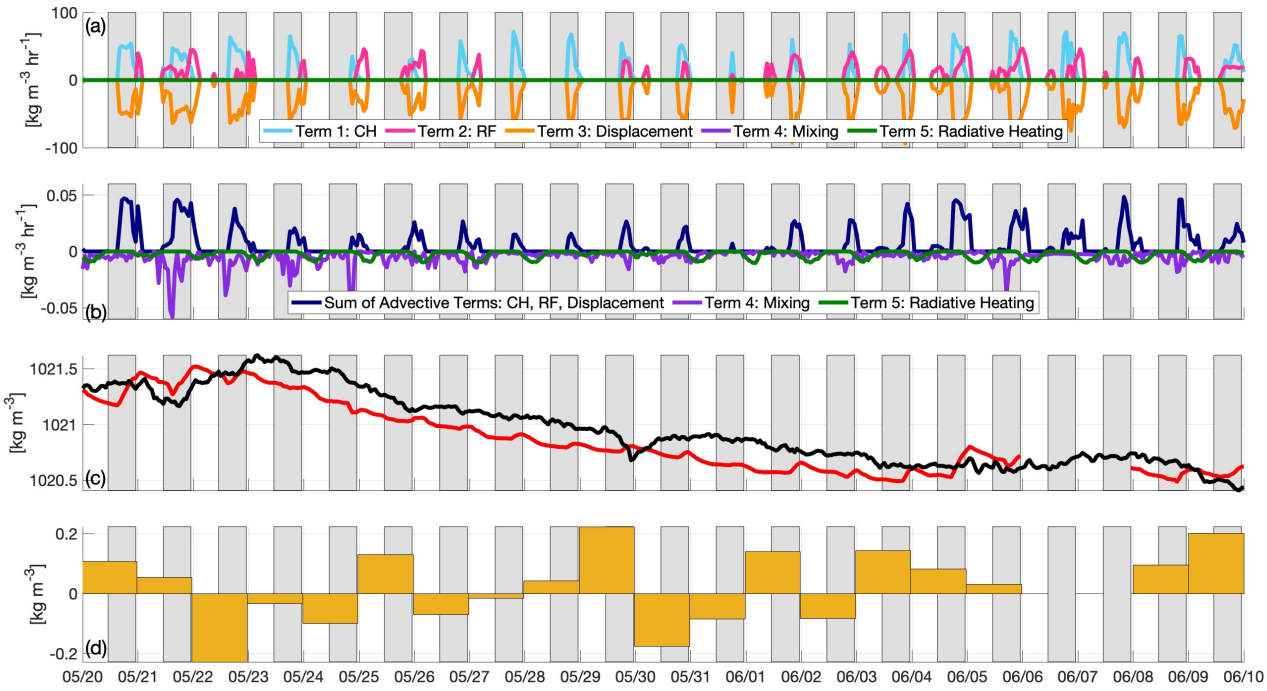

Figure 3.2: a) The 4 hour lowpass filtered mass budget terms from Equation 3.5 divided by the lagoon bottom water volume. Mass flux due to solar radiative heating (green), north channel mass flux (blue), mass flux due to turbulent mixing (purple), reef flat mass flux (pink), and vertical displacement (orange). Positive values indicate flux of higher density water into the control volume. b) Zoom in of mass flux due to radiative heating (green), mass flux due to mixing (purple), and total mass flux due to advective terms (north channel, reef flat, and vertical displacement) (navy). c) Net density loss in the lagoon during duration of study period in kgm^{-3}. The black line is the modeled density and the red line is the observed density. d) Daily residual between the observed and modeled density.

3.3.2 Bottom Volume Mass Budget

The modeled bottom volume mass budget (Equation 3.5) captures the primary trends in the observed bottom water density with an $R^2 = 0.74$ and an average daily residual of -0.047kg m^{-3} (Figure 3.2c,d). The density of the bottom waters of the lagoon decreases over the 3-week study (Figure 3.2c) due to direct radiative heating of the bottom waters (green line in Fig 2b) and turbulent mixing of warmer water from above (purple line in Figure 3.2b). Brief periods of density increase occur during the first and third weeks (around 22 May and 06 June in Figure 3.2c), coinciding with spring tide conditions in which advection of dense, cool water from the reef flat and the channels into the bottom of the lagoon is greatest.

Dense advective contributions over the reef flat and through the channels increase density of the lagoon bottom water with the reef flat contributing to 42% and the north channel contributing 58% of the total dense water inflow volume (Figure 3.2a). The advective terms are largely balanced by the vertical displacement term. The density of the system is further reduced by vertical mixing and light attenuation at depth by -2.5kg m^{-3} and -1.2kg m^{-3}, respectively, cumulatively over the duration of the three week study period (Figure 3.2b). The advective terms add mass to the bottom volume in daily volume pulses which are modulated by the spring-neap cycle. On average, during spring tide, the reef flat contributes 42% of the dense water inflow volume compared to 58% through the north channel. During neap tide, the total magnitudes of dense water inflow volume is reduced by 60%, with the reef flat and north channel contributing 55% and 65% less dense water inflow volume than they did during spring tidal forcing, respectively (Figure 3.2a). These pulses of dense water inflow occur on daily cycles due to the primarily diurnal tides at Dongsha Atoll.

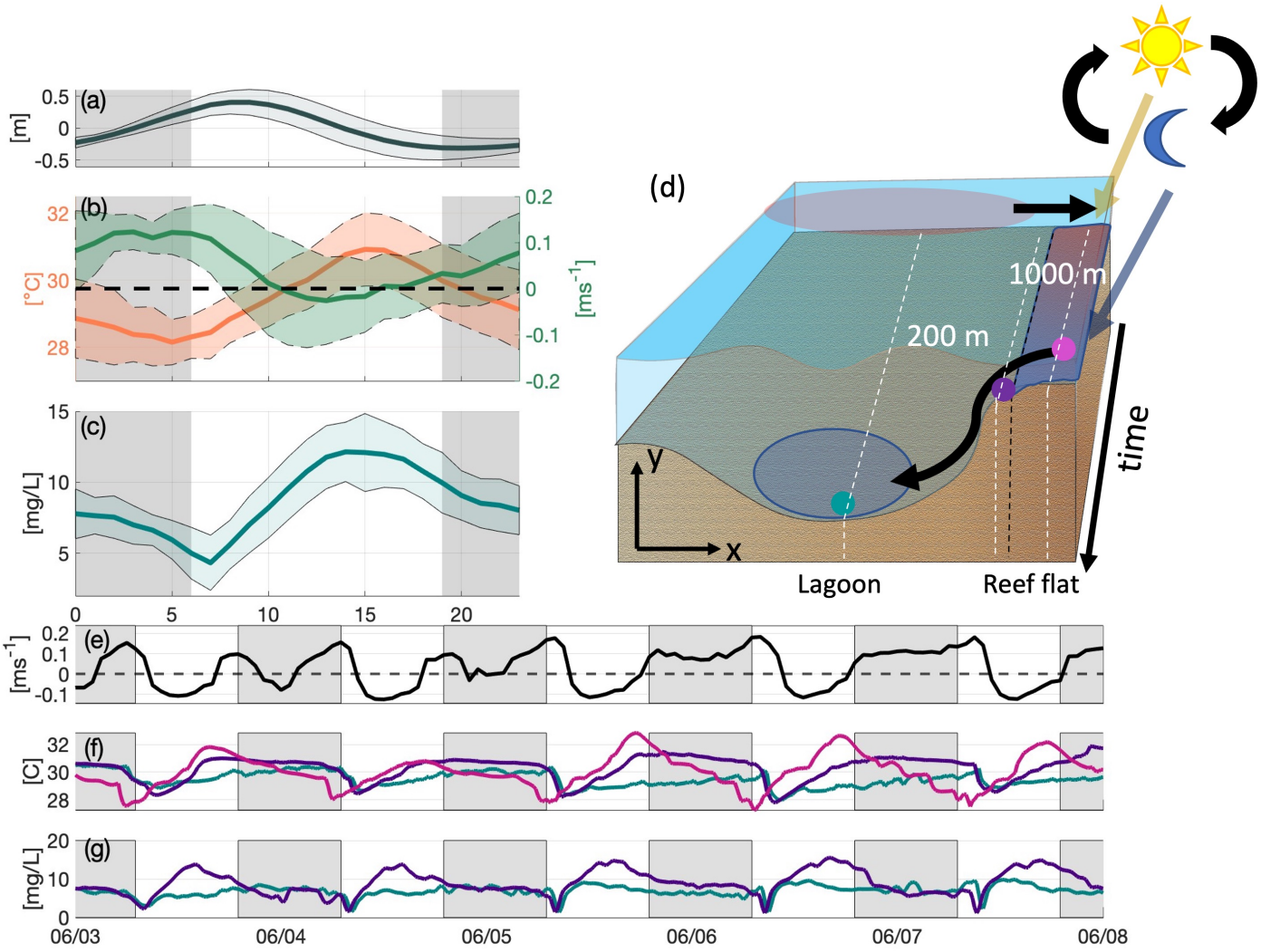

Figure 3.3: a) 4 to 60 hour bandpass filtered tidal water level daily averaged for the duration of the study period from SBE37 on the north lagoon mooring at 3.6 m depth. b) 4 hr low pass filtered east reef flat temperature (orange) and estimated reef flat velocity (green) daily averaged for the duration of the study period. c) East reef dissolved oxygen daily averaged for the duration of the study period. Grey regions indicate night. Lightly shaded colored regions indicate the range of one standard deviation from the mean. d) Conceptual illustration of the east reef flat and east lagoon sensors and the diurnal heating and cooling cycle. Pink dot represents the temperature sensor at approximately 1 meter depth on the east reef, purple represents the temperature and DO sensor at 2.5 meters depth at the edge of the east reef, and green represents the temperature and DO sensor at 10 meters depth inside the east lagoon. Not drawn to scale.

3.3.3 The Influence of Diurnal Tidal and Solar Phasing on the Reef Flat

Dense water flowing from the reef flat into the lagoon is a significant part of the lagoon bottom water mass budget. Here we will examine how the phasing between the diurnal tide and the solar cycle regulates the formation and transport of dense water from the reef flat into the lagoon. Due to the similar period of these cycles, they are near phase-locked during the study period, with flood tide (lagoonward transport) occurring at night. The shallow reef flat experiences strong heating during the day and cooling at night, with an average diurnal temperature range of over 4°C during the study period (Figure 3.3b).

At the end of night during the study period, as the diurnal tide nears maximum flood (Figure 3.3a), the strongest lagoonward flow is observed, corresponding to the coolest, lowest oxygen water observed on the reef (Figure 3.3b). The reef flat on Dongsha is highly productive with high rates of primary productivity during the day, as evidenced by super-saturated oxygen concentrations, and respiration at night, drawing down oxygen on the reef to hypoxic, even anoxic, levels (Figure 3.3c). This creates a cascade of dense, low oxygen water off the reef flat to depth inside the lagoon on a daily cycle (Figure 3.3d). This pattern is most prevalent during spring tide, when tidally driven flow on the reef is strongest, and can be traced through both oxygen and temperature measurements on the reef to 10 m depth inside the east lagoon (Figure 3.3f,g).

During the second spring tide of the study period, pulses of cold water on the east reef flat at 1 m depth are lagged by cold pulses at 2 m depth at the lagoon-reef interface and at 10 m depth on the east edge of the lagoon (Figure 3.3f). These lagged pulses in temperature also correspond to pulses in oxygen measurements at 2 and 10 m depth with measurements of oxygen below the low oxygen threshold of 4.6 mg L^{-1} at the 10 m site (Figure 3.3g). The timescales of the lag between these pulses scale with theoretical gravity current flow

timescales defined as (Benjamin, 1968),

$$U = \sqrt{2g'h}. \tag{3.8}$$

h is the height of the gravity current and g' is the reduced gravity. For this calculation we assume no mixing and a constant gravity current depth between sensors. The east reef flat sensor in the middle of the reef flat is ∼1000 m away from the sensor on the edge of the east reef with an average lag of ∼2 hours between temperature pulses. From equation 3.8, we estimate a gravity current speed of $\sim$ 0.2 m s^{-1}, providing a lag estimate of 1-2 hours between pulses on the reef flat. The sensor on the edge of the east reef and the sensor at 10 m depth are 200 m apart with observed pulses lagged ∼15 minutes compared to the estimated lag of 15-30 minutes.

3.4 Discussion

3.4.1 Flushing Time Estimates

In Merrigan et al. (b) (in review), the estimated flushing time inside Dongsha Atoll lagoon is found to be 2.9 days for the study period. This is a relatively short flushing time for a system that has experienced hypoxia, as oxygen drawdown has been often reported as due to high residence times (timescales of weeks to months, Fennel and Testa (2019)) and limited air-sea gas exchange. In order to better understand the relative flushing time of the lagoon bottom water compared to the whole lagoon, we use the bottom water mass budget to constrain flushing time estimates for the bottom volume. The flushing time captures the bulk renewal timescales within a system, here calculated as the volume of lagoon bottom

water (V_B) divided by the volumetric flow rate through the system (Q) (Monsen et al., 2002),

$$T_f = \frac{V_B}{Q}. \tag{3.9}$$

Here, Q is defined as the volume of the inflowing water through the north channel and over the reef flat when the inflowing water is greater in density than the ambient bottom water, as described in Section 3.3, and V_B is the volume of the lagoon bottom water.

The average flushing time of the bottom water for the study period is 3.7 days with the reef flat replenishing 15% of the bottom volume and the north channel replenishing 21% of the bottom volume in one day, displacing an average 0.5 m and 0.7 m of water, respectively (Figure 3.4d). During the study period, there is spring-neap variability to the flushing time. During neap tide, the north channel and reef flat flush 15% (0.5 m) and 8% (0.28 m) of the bottom volume in one day, respectively, with an average flushing time of 5.6 days. Conversely, during spring tide, the north channel flushes 23% (0.80 m) and the reef flat flushes 18% (0.62 m) with an average flushing time of 2.7 days.

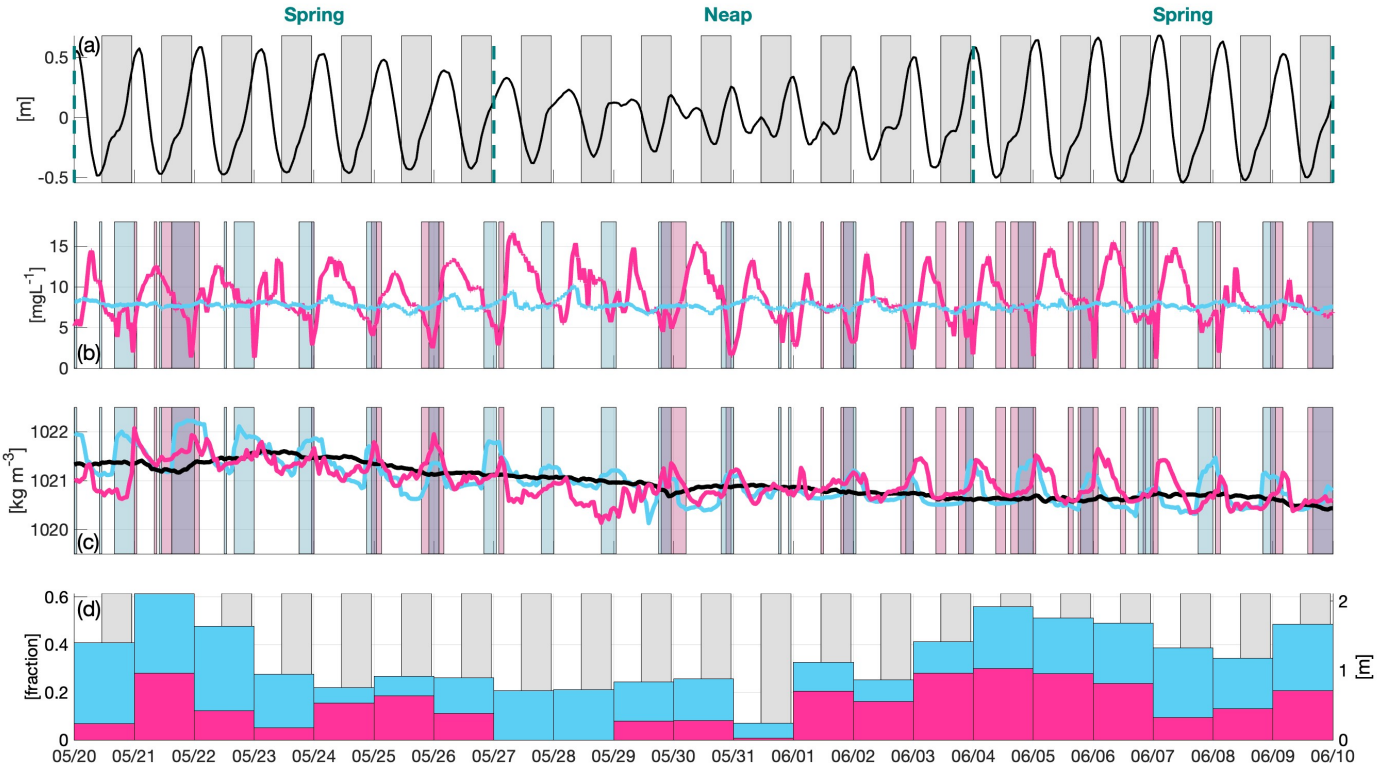

Figure 3.4: a) Tidal water level from SBE37 on north lagoon mooring at 3.6 m depth, bandpass filtered from 4 to 60 hours. b) Dissolved oxygen in the north channel at 10 m depth (blue) and on the east reef at 2.5 m depth (pink). c) Density in the north channel (blue), on the reef flat (pink), and the observed ambient lagoon bottom water density (black). Blue and pink shaded regions indicate periods of inflow that is greater or equal to the density of the ambient lagoon bottom water in the north channel and over the reef flat, respectively. d) Fraction of the total bottom volume flushed in one day (right) and the depth in meters of the inflow in one day based on the bottom volume surface area by the north channel volume flux (blue) and the reef flat volume flux (pink).

During the second spring tide, when waves are low (average significant wave height of 0.5 m, Figure3.1h), the flushing time is 2.3 days compared to 3.1 days during the first spring tide when waves are high (average H_s of 1.5 m, Figure3.1h). During the first and second spring tide, the north channel flushes an average of 23% (0.80 m) and 24% (0.82 m) of the bottom volume, respectively. However, the fraction flushed by the reef flat varies between 14% (0.49 m) during the first spring tide and 22% (0.75 m) during the second (Figure 3.4d). Although waves are an important driver of volume flux over the reef flat, volume contribution to the bottom water is also dependent on the density of both the ambient bottom water and the density of the incoming water masses. As the lagoon heats over the study period (Merrigan et al. (b), in review), the density of the lagoon, including the bottom volume, decreases. During the first spring tide, lagoon bottom volume density is more similar to the density of the incoming water masses, especially the reef flat, leading to more moderate renewal events. During the second spring tide, as the lagoon has lost density over the study period, the difference in density between the incoming reef flat and north channel water is greater. The reef flat is almost always denser than the bottom volume during this period, leading to an increase in reef flat driven renewal events.

In comparison, hypoxia time scales are defined by the amount of time it takes a system to deplete its initial oxygen supplies C_{O_2} from daily net oxygen consumption R_{net} alone (Fennel and Testa, 2019),

$$T_{hyp} = \frac{C_{O_2}}{R_{net}}. \tag{3.10}$$

Here, C_{O_2} is defined as the beginning of day oxygen concentration, ~ 6.5 mg L^{-1}, from the daily composite average of oxygen at the bottom mounted oxygen sensor at 13 m depth located near the lagoon center. R_{net} is estimated from the difference in end of night oxygen

concentration and beginning of day oxygen concentration from the same daily composite average of the center lagoon oxygen sensor, resulting in a daily average change is dissolved oxygen concentration of $-.15$ mg L^{-1}. The center lagoon oxygen sensor is the deepest oxygen sensor from the deployment (13 m) with more limited advective influence compared to sensors near the channels and reef flat. The average hypoxia time scale for the study period is estimated to be 43 days, an order of magnitude larger than the flushing time estimates, indicating advection is the principle driver of low oxygen inside the lagoon bottom waters during the study period.

3.4.2 Implications of tidal phasing on oxygen dynamics inside Dongsha Atoll lagoon

Diurnally dominant tides have an annual pattern. On Dongsha, maximum flood-at-night occurs near the summer solstice, while flood-during-day occurs near the winter solstice. Due to the seasonality of the tidal phasing on the reef flat, Dongsha Atoll lagoon could be susceptible to advectively driven low oxygen pulses during the summer months, as observed in this study and in DeCarlo et al. (2017a). This seasonal stress of low oxygen inside the lagoon is further exacerbated by warmer water temperatures during summer months. Water temperatures outside of organisms' thermal tolerances alone challenges tropical coral ecosystems. Additionally, increased water temperatures increase the biological oxygen demand, as well as decrease the oxygen solubility of the water, further stressing the oxygen availability of the system.

In conjunction with seasonal heating trends, the regional northern South China Sea seasonal climatology of quiescent wind and waves during early summer months creates conditions susceptible to hypoxia. This study suggests that during the summer, when wind and waves are low, and tides are the primary driver of flow over the reef flat, lagoonward transport at night

allows oxygen draw-down and transport of cool offshore water across the reef throughout the night, creating the advective pulses of dense, low oxygen water at depth inside the lagoon. Calm wind and wave conditions often create stratified water columns with reduced mechanisms for vertical mixing, further isolating the bottom volume. However, longer oxygen and temperature records would be required in order to understand the impacts of seasonal trends in both oxygen and tidal phasing in the lagoon and on the reef flat and prove the repeated seasonality of this phenomenon.

3.5 Conclusion

This study uses observations to constrain a control volume analysis of bottom water mass for the Dongsha Atoll lagoon to capture the physical processes driving bottom water renewal and the timescales of these events. We show that unlike many documented hypoxic systems with long residence times, the bottom water flushing timescale is relatively low, varying, on average, between 3-4 days. The magnitude and frequency of renewal events are increased during spring tidal forcing, coinciding with an increase in observed hypoxic events at depth inside the lagoon.

During the study period the tide is near phase locked with flood at night. This creates a lagoonward flow of cooler offshore water as oxygen is drawn down due to high biological respiration on the shallow reef flat. The observed renewal events episodically transport dense, low oxygen water to depth inside the lagoon at the end of night, creating a mechanism for advectively driven hypoxia.

These observations highlight the role of physical-biological interactions in shaping oxygen dynamics of tropical, coastal systems and emphasizes the need for further work to contextualize the seasonal tidal and oxygen phasing on the reef.

Chapter 4

Physical-biological interactions driving low oxygen events on a wide reef flat

4.1 Introduction

Oxygen availability has decreased across the global ocean since the mid-20th century, with the expansion of oxygen minimum zones linked to increasing ocean temperatures and marine heat wave events (Stramma et al., 2008; Keeling et al., 2010; Breitburg et al., 2018; Bopp et al., 2013; Kwiatkowski et al., 2020; Frölicher et al., 2018). Over the next century, global ocean oxygen concentrations are predicted to further decrease an additional 1-7% (Keeling et al., 2010; Long et al., 2016). Understanding the physical and biogeochemical controls influencing oxygen dynamics is imperative, as dissolved oxygen is a critical currency in marine environments, impacting productivity, biodiversity, and biochemical processes (Breitburg et al., 2018).

The coastal ocean is especially susceptible to the impacts of hypoxia due to the influence from various physical and biological processes including high biological demand, stratification, upwelling, and both anthropogenic and natural eutrophication(Breitburg et al., 2018; Gilbert et al., 2010; Howarth, 2008; Diaz and Rosenberg, 2008; Chan et al., 2008). Biological cycles, which strongly influence oxygen variability in shallow waters (Kemp et al., 2009a), include primary production (adding oxygen to the water column during the day) and respiration (the rate at which organisms consume oxygen). Primary production occurs only during the day while respiration happens continuously and is a dominant process at night when primary production is absent. Physical mechanisms such as stratification limit air-sea gas exchange and can isolate bodies of water, reducing oxygen availability and limiting renewal events (Fennel and Testa, 2019; Farmer and Freeland, 1983). Other physical processes, such as wind- or wave-driven vertical mixing and advectively driven renewal can relieve systems experiencing low oxygen (Boesch and Rabalais, 1991; Stanley and Nixon, 1992; Kemp et al., 2009b). While hypoxia has traditionally been defined as < 2 mg L^{-1}, recent studies have shown dissolved oxygen levels as low as 5 mg L^{-1} can cause sublethal harm to some organisms (Vaquer-Sunyer and Duarte, 2008).

Despite the notoriety of hypoxia as a stressor the coastal zone, Altieri et al. (2017) highlights the disparity of studies of hypoxia in the coastal tropics. Oxygen availability in tropical systems are strongly influenced by temperature. As ocean temperatures continue to rise, oxygen availability will become limited due to reduced oxygen solubility and increased biological respiration, exacerbating the effects of thermal stress on coral reefs (Vaquer-Sunyer and Duarte, 2011). Though more recent work has begun to investigate hypoxia in the shallow tropics (Adelson et al., 2022; Pezner et al., 2023), there is still a critical knowledge gap in understanding hypoxia in these systems.

Dongsha Atoll is a coral atoll situated in the northern South China Sea. Previous work has shown the importance of internal waves and other physical processes in driving circulation

and subsequent temperature and nutrient availability across the wide (3 km) reef flat (Reid et al., 2019, 2020). During summers 2014 and 2015, fish kills and sea grass die offs were observed inside Dongsha Atoll lagoon and hypothesized to be related to hypoxia (Gajdzik and DeCarlo, 2017).

More recently, studies from a 2019 observational campaign in the region found lagoon-wide flushing times of $\sim$ 3 days and bottom water flushing times of 3-4 days (Merrigan et al. (b), in review, Merrigan et al. (a), in prep). Merrigan et al. (a) (in prep) estimated the time that it would take hypoxia to form from daily oxygen drawdown in the center of the lagoon is 43 days, an order of magnitude greater than the flushing timescales, indicating that advection is likely the principle drive of hypoxia. Additionally, Dongsha Atoll is geographically isolated, located 350 km from the nearest mainland, and therefore has limited anthropogenic influence on the marine environment, apart from a small coast guard base on Pratas Island. Merrigan et al. (a) examines the advective formation of hypoxia inside Dongsha Atoll lagoon. During the study period, diurnal tides are near phase-locked with the solar cycle and, thus, biological primary productivity - with flood tides driving flow toward the lagoon at night as respiration is drawing down oxygen on the shallow reef flat. This results in the advection of cool, low-oxygen water off of the reef flat and into the lagoon at the end of night, resulting in episodic pulses of dense, low-oxygen water that sink to the bottom of the lagoon (Merrigan et al. (a), in prep). This coupled physical-biological process represents a naturally-occurring mechanism for the formation of benthic hypoxia events and, while it has not been reported previously that we could find, likely is not unique to Dongsha Atoll.

4.2 Methods

4.2.1 Field site

Dongsha Atoll is a coral atoll located in the South China Sea with a diameter of 28 km and a surface area of approximately 600 km^2 (Figure 4.1a) (Dai, 2004). The atoll system is comprised of a central lagoon surrounded by a shallow reef flat to the north, east, and south, and two channels to the west separated by Pratas Island (Figure 4.1b). This study focuses on the east reef flat which has a width of nearly 3 km, an average depth of 0.9 m, and minimum and maximum depths of 0.6 m and 3.5 m, respectively (Figure 4.1d) (Reid et al., 2019). A survey from a previous study of the reef showed the benthic reef flat community consists of fleshy algae, sea grass, and live coral (DeCarlo et al., 2017a).

Previous work on the east reef flat illustrated that the thermal and biogeochemical environment on the shallow reef is heavily influenced by the shoaling of internal waves on the sloping forereef, cooling the reef by as much as 2 °C and increasing nutrient concentrations (Reid et al., 2019). Reid et al. (2019) found surface waves and tides to be the primary driver of flow over the east reef flat.

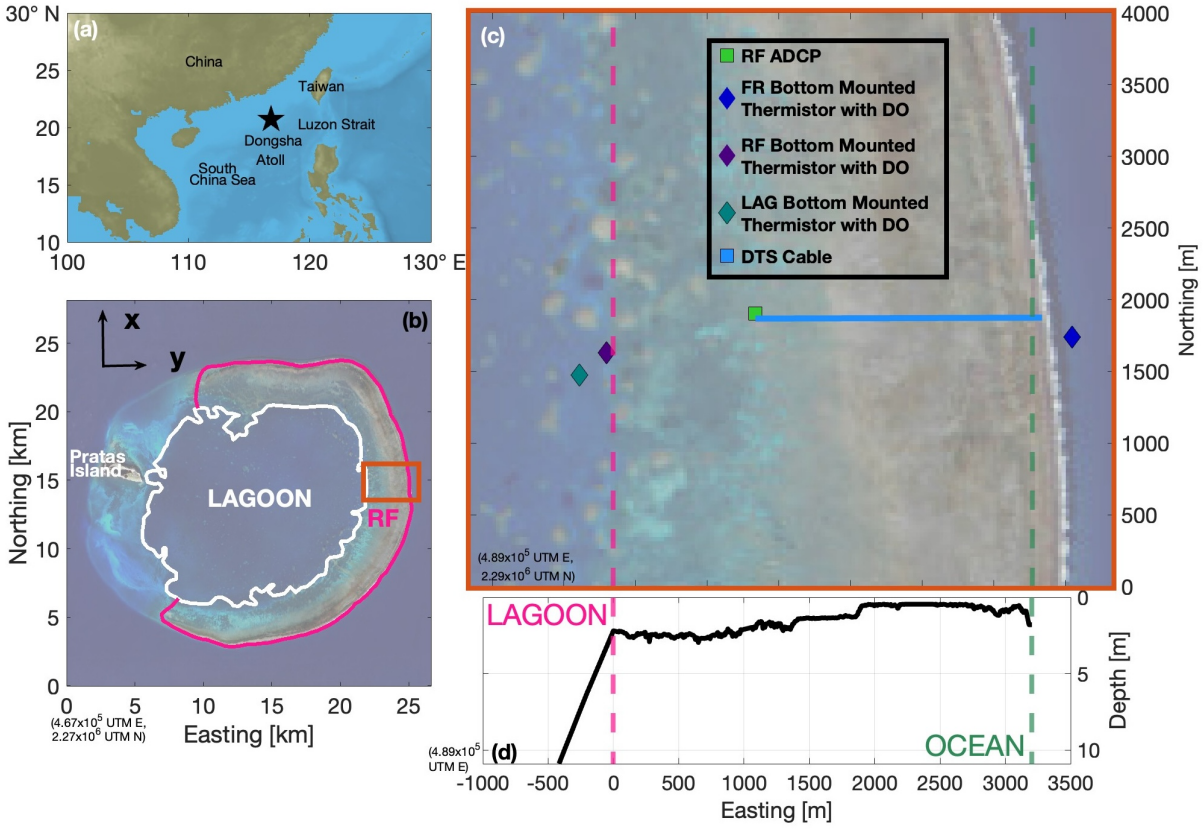

Figure 4.1: a) Map with location of Dongsha Atoll in the South China Sea with, b) Satellite image of Dongsha Atoll showing location of Pratas Island and the Reef Flat (RF). Orange box indicates the region included in panel c. c) Instrument locations used in this study from the 2019 lagoon experiment. Temperature and dissolved oxygen sensors are shown in diamonds (blue: forereef (FR), purple: reef flat (RF), and teal: lagoon (LAG)), current meters are shown in squares, and Distributed Temperature Sensing (DTS) cable shown as blue track. Lagoonward reef boundary marked by pink dashed line and oceanward reef boundary marked by green dashed line. d) Bathymetric cross-section across the east reef flat where DTS was located from LIDAR.

4.2.2 Experiment

The observations presented here are part of a larger study of circulation and bottom water renewal inside Dongsha Atoll Lagoon (Merrigan et al. (b), in review). For the scope of this paper, we will focus on temperature, dissolved oxygen (DO), and currents measurements on the east reef flat from 20 May to 10 June 2019. Water velocity was measured by a 1200 KHz Teledyne RDI WorkHorse acoustic doppler current profiler (ADCP) sampling at 2-second intervals. The ADCP was placed approximately 1 km from the reef-lagoon boundary at a depth of 2.5 m (Figure 4.1c). DO and temperature on the east reef flat and inside the east lagoon at 2.6 and 10 m (RF and LAG, Figure 4.1c), respectively, and were measured by JFE RINKO W sensors sampling at 15 minute intervals (bottom mounted, measuring temperature to $\pm$ 0.02°C and dissolved oxygen to $\pm$ 0.1 mg L^{-1}) (Figure 4.1c). Additional temperature measurements were collected along a distributed temperature sensing (DTS) cable with full deployment details outlined in the following section. Offshore conditions of wind speed and direction, significant wave height, wave direction, and cloud coverage were obtained from the European Center for Medium-Range Weather Forecasts (ECMWF) ERA5 1-hour data on a 30-km grid (Hersbach et al., 2020).

4.2.3 DTS set up and calibration

A DTS cable was deployed on the east Dongsha Atoll reef flat and forereef slope, but here we will consider the data along a 2km section extending from the reef crest towards the lagoon (Figure 4.1c). DTS technology emits a coherent pulse of light through a fiber optic cable, measuring Raman back-scattered light spectra to determine temperature continuously along the length of the cable (Tyler et al., 2009b; Hausner et al., 2011). A Silixa XT-DTS system was stationed on the reef flat at the cable origin and measured nearbed temperature every 0.25 m along the cable, every 30 seconds.

The cable was deployed with 2 calibration baths, a cool and warm (ambient temperature) bath, each containing a 10-m coil of cable and a RBR SoloT (measuring temperature to $\pm$ 0.002°C). An additional calibration coil was placed along the cable at the 10 m isobath on the east forereef. The DTS cable was calibrated following Sinnett et al. (2022) with a constant DTS calibration parameter γ (Sinnett and Feddersen, 2019; Hausner et al., 2011), as well as a spatial and temporal filtering of 1.5 m and 3 minute, respectively, resulting in an RMSE = 0.2°C.

4.2.4 Reef flat heat budget

A heat budget was calculated for the east reef flat to test our assumptions of transport across the reef. Following Reid et al. (2019) and Davis et al. (2011), the heat budget on the reef was calculated as,

$$\frac{\partial T}{\partial t} + \overline{u}\frac{\partial \overline{T}}{\partial x} = -\frac{\partial}{\partial x}\overline{u'T'}, \tag{4.1}$$

where x is the cross reef distance with positive to the east, u denotes the velocity component in the x direction, and T is temperature. Overline denotes depth averaging. For this analysis, we are only applying the heat budget in the cross-reef direction, as alongshore velocities and vertical velocities during this study period are found to be an order of magnitude smaller than the cross-reef velocities. Temperature is assumed to vertically homogeneous over the shallow, well-mixed water column.

The instruments deployed during this study were sampling at an insufficient frequency to capture turbulent processes. Following previous work on Dongsha Atoll (Reid et al., 2019) and heat budgets in other shallow reef systems (Davis et al., 2011) that show an approximate

balance between the advection of heat across the reef flat and surface heat fluxes, here we will neglect both turbulent heat fluxes and heat fluxes through the reef bed.

From Equation 4.1, we integrate over the water column and multiply by the heat capacity per unit volume (ρc_p, assumed constant and equal to 4.1×10^6 W s m^{-3}C^{-1}), resulting in a heat budget of,

$$\rho c_p \frac{dT}{dt} = -\rho c_p h \langle \overline{u} \rangle \frac{d\overline{T}}{dx} + Q_N, \tag{4.2}$$

or,

$$Q_T = \Delta F + Q_N. \tag{4.3}$$

The left hand side, Q_T, is the rate of change of heat storage within the volume. The first term on the right hand side, ΔF, is the advective heat flux, and the second term, Q_N is the net surface heat flux across the air-sea interface. h is the depth of the water column and u is the cross-reef depth averaged velocity from the east reef flat ADCP pressure and velocity, where $\langle\rangle$ denotes time averaging of 1-hr.

The heat budget is calculated discretely on a 200 m and 1-minute spatial and temporal grid, respectively, using an upwind scheme in space and a forward differencing scheme in time. Transport is conserved across the reef, with velocity estimated at each distance bin using the average bin depth at mean sea level and η estimated from the east reef flat ADCP pressure 4- to 60-hour bandpass filtered ($h = D + \eta$). The initial condition across the reef is established using 200 m averaged DTS temperature across the reef. The oceanward boundary condition

is set as the 1-hr lowpass filtered DTS temperature at the reef crest, and the lagoonward boundary condition is set as the daily composite temperature from the east reef flat JFE RINKO W sensor at 2.6 m depth near the lagoon-reef boundary.

The net surface heat fluxes at the air-sea interface are calculated as,

$$Q_N = Q_E + Q_H + Q_S + Q_L \tag{4.4}$$

where Q_E is the latent heat flux, Q_H is the sensible heat flux, Q_S is the shortwave heat flux, and Q_L is the longwave heat flux. Q_E, Q_H, and Q_L are calculated via the COARE 3.0 (Coupled Ocean-Atmosphere Response Experiment) algorithm (Fairall et al., 1996, 2003) with observed meteorological data inputs from the Dongsha airport and Dongsha Navy weather stations; cool skin and warm layer corrections were not applied. Cloud coverage is obtained from ECMWF ERA5 1-hour data. Q_S is observed at the Dongsha airport weather station with albedo calculated via methods presented in (Taylor et al., 1996) with an additional correction to the albedo of 10% to account for high reflectance on a shallow coral bed (Maritorena et al., 1994). Atmospheric heat fluxes use the temperature from the previous timestep as input.

The modeled heat budget is compared against the observed DTS temperature measurements using the Wilmott skill score (Willmott, 1982),

$$WSS = 1 - \frac{\frac{1}{N}\Sigma_{i=1}^{i=N}(m_i - o_i)^2}{\frac{1}{N}\Sigma_{i=1}^{i=N}(|m_i - \overline{o}| + |o_i - \overline{o}|)^2} = 1 - \frac{MSE}{\frac{1}{N}\Sigma_{i=1}^{i=N}(|m_i - \overline{o}| + |o_i - \overline{o}|)^2}. \tag{4.5}$$

N is the number of pairs of model and observation points with o_i as the observational point

and m_i as the corresponding model point. MSE is the mean square error. A skill score of 1 represents to a perfect agreement between the observations and model while a skill score of 0 represents no agreement.

4.2.5 Reef flat oxygen budget

The depth averaged oxygen budget is estimated as

$$\frac{\partial DO}{\partial t} = -\overline{u}\frac{\partial DO}{\partial x} - \frac{\partial}{\partial x}(K\frac{\partial DO}{\partial x}) + F_{DO} + F_{pp} - F_R. \tag{4.6}$$

x is the cross-reef distance with positive east, u is the the velocity in the cross-reef direction, and DO is the dissolved oxygen concentration. Previous studies of oxygen fluxes in coral ecosystems have found fluxes through the air-sea interface to be negligible than the contributions through advection, as well as biological production and consumption (Long et al., 2019; Pezner et al., 2023). The oxygen budget simplifies to

$$\frac{dDO}{dt} = -\overline{u}\frac{dDO}{dx} + F_{PP} - F_R. \tag{4.7}$$

The left-hand-side of Equation 4.7 is the rate of change of dissolved oxygen concentration. The first term on the right-hand-side of the equation is the advective oxygen flux, the second term is the gross primary production rate, and the third term is the respiration rate. We define the gross primary production rate as (Falter et al., 2013),

$$F_{PP} = Psin(\frac{\pi(t - t_{sr})}{(t_{ss} - t_{sr})})^{1.2} \qquad \text{for} \quad t_{sr} \leq t \leq t_{ss} \tag{4.8}$$

$$F_{PP} = 0 \qquad \text{in all other cases}$$

P is maximum gross primary production rate, t_{ss} is time of sunset, and t_{sr} is time of sunset. The maximum primary production rate is estimated from the average rate of change of oxygen at the east reef flat oxygen sensor when flow is lagoonward, in order to mitigate the influence of lagoon water advected onto the reef. Similarly, respiration is assumed to be constant and is estimated from the average rate of change of oxygen at the east reef flat oxygen sensor when flow is lagoonward at night. The original respiration rate value obtained from this analysis, -0.013 mg m^{-2} min^{-1}, resulted in a low oxygen bias in the daily composite average, and was therefore decreased to -0.012 mg m^{-2} min^{-1}, changing the R^2 from 0.91 to 0.96. Further discussion of this can be found in the oxygen budget result section. Respiration and primary production are assumed to be spatially and temporally homogeneous for the study period.

The oxygen budget is calculated discretely on a 60 m and 1-minute spatial and temporal grid, respectively, using an upwind scheme in space and a forward differencing scheme in time. Similar to the heat budget, transport is conserved across the reef, with velocity estimated at each distance bin using its average depth at mean sea level and η estimated from the east reef flat ADCP pressure 4- to 60-hour bandpass filtered ($h = D + \eta$). There are no oxygen observations on the reef crest during the study period so the offshore boundary condition was established using a daily composite average of offshore dissolved oxygen using the closest available observations on each side of the study period (15 September to 15 October 2019 and 25 February to 25 March 2020) 1-hr lowpass filtered. The lagoonward boundary condition is established from the daily composite average dissolved oxygen from the east reef flat JFE

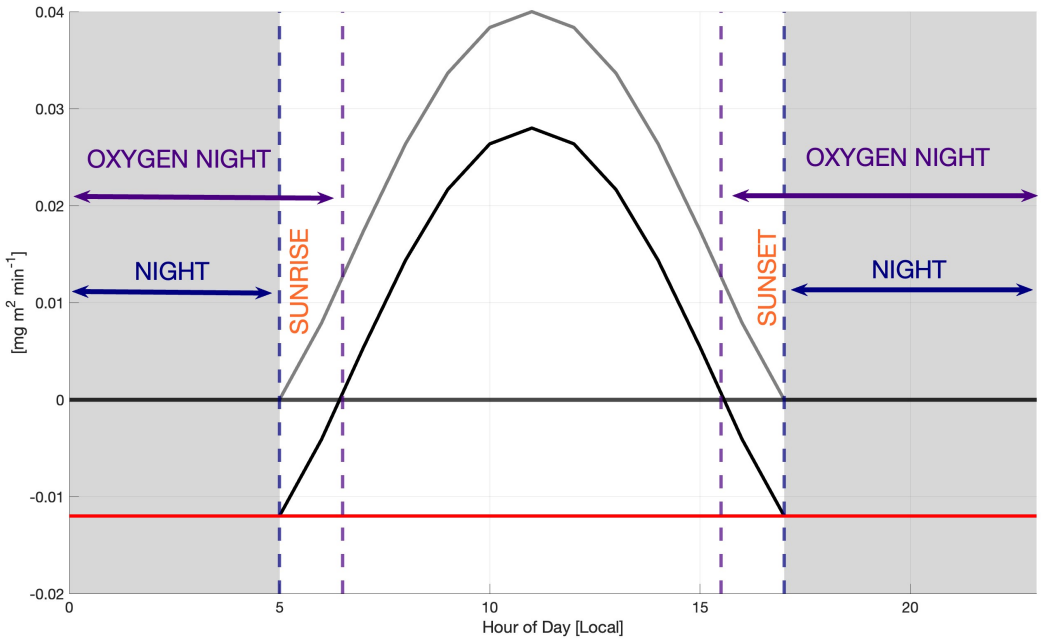

Figure 4.2: Graphical illustration defining 'oxygen-night' in local time. Shaded gray indicated night. The gross primary production curve is shown in the gray curve and the respiration rate plotted in red. The black line is the sum of the primary productive curve and the respiration rate. The primary production curve is 0 mg m^{-2} min^{-1} at night, defined in navy. 'Oxygen-night' is defined in purple and includes all times when the respiration rate is greater than the primary production rate, allowing for oxygen drawdown to occur (approximately 1-hour prior to sunset and 1-hour post sunrise during the study period).

RINKO W sensor at 2.6 m depth near the lagoon-reef boundary (RF Figure 4.1c). The initial condition across the reef is set by linearly interpolating offshore the dissolved oxygen at the offshore boundary condition to the dissolved oxygen at the lagoonward boundary condition.

4.2.6 Particle tracking

We implemented two particle tracking experiments to estimate residence time of water on the reef flat and understand oxygen dynamics. We used a quasi-lagrangian framework similar to that outlined in Reid et al. (2019). Particle paths were tracked using *in situ* velocity, pressure, and bathymetry data. We applied a constant transport in the cross-sectional direction along the reef in the same 60-m grid applied in the oxygen budget, estimating flow in each bin by dividing the observed transport from the RF ADCP by the water depth defined in the section above. A 1D particle tracking was performed, only considering cross-shore (cross-reef) velocities.

Here, we define oxygen-night as the period approximately from sunset to sunrise when the respiration rate is greater than the gross primary production rate (Figure 4.2). During our study period oxygen-night is approximately 14 hours long, and the average night (between sunset and sunrise) is approximately 12 hours. The primary production rate curve peaks at midday, eventually decreasing to 0 mg m^{-2} min^{-1} at sunset. A window of approximately 1-hour prior to sunset and following sunrise exists during our study period where the respiration rate exceeds the primary production rate, leading to net oxygen drawdown.

Two particle tracking-experiments were performed to (A) better understand the transport and oxygen conditions that led to observed hypoxic events that occurred during our study period (Experiment A), and (B) to look more generally at the transport and oxygen history of all water masses arriving at the reef-lagoon boundary during oxygen-night (Experiment B). For Experiment A, particles were released 15-minutes lagged from observed hypoxic events inside the east lagoon (which often occur after oxygen-night), based on the observed lag between oxygen signals on the east reef flat and inside the east lagoon (Merrigan et al., a). For Experiment B, particles were released at the edge of the reef flat-lagoon boundary throughout the oxygen-night and tracked backwards in time to determine the location of the

particle along the reef at the beginning of oxygen-night.

4.3 Results

4.3.1 Oceanographic conditions

The three-week study period is characterized by two spring tidal periods, 20-26 May 2019 and 04-10 June 2019, and one neap tidal period, 27 May-03 June 2019, with tidal amplitudes varying from 0.4 to 1.2 m between neap and spring tidal regimes. The tides were primarily diurnal, with the amplitude of the diurnal tidal constituents over twice as large as the semi-diurnal tidal constituents, and nearly phase locked with the solar day, where flood tide occurs at night (Figure 4.3a). Winds direction was predominantly from the north throughout the duration of the study period, except for 20-23 May, during which they were from the southeast and wind magnitude varied from 2 to 6 $\mathrm{m\,s^{-1}}$ (Figure 4.3b). Significant wave height varied from 0.2-2 m. The largest waves were observed 25 May, but decreased to an average significant wave height of 0.5 m from 01-07 June, before increasing again to 1.2 m from 08-10 June (Figure 4.3c). Waves were primarily from the east, shifting to originate from the south on 01-05 June and 09-10 June (Figure 4.3c). Over the 3 week study period, water temperature on the reef flat and inside the lagoon increased approximately 1.5°C, predominantly driven by surface heat fluxes (Figure 4.3d) (Merrigan et al., b). Dissolved oxygen on the reef flat has strong diurnal fluctuations, ranging from oxygen concentrations that consistently exceed 10 mg $\mathrm{L^{-1}}$ during the day, to hypoxic levels at night ($\leq$ 2 mg $\mathrm{L^{-1}}$) (Figure 4.3e). Dissolved oxygen concentrations inside the lagoon has smaller amplitude diurnal fluctuations, but both the reef flat and lagoon oxygen signals show sharp pulses of hypoxic water arriving in early morning during spring tides (e.g. 21-23 May and 06-10 June) (Figure 4.3e) (Merrigan et al., a).

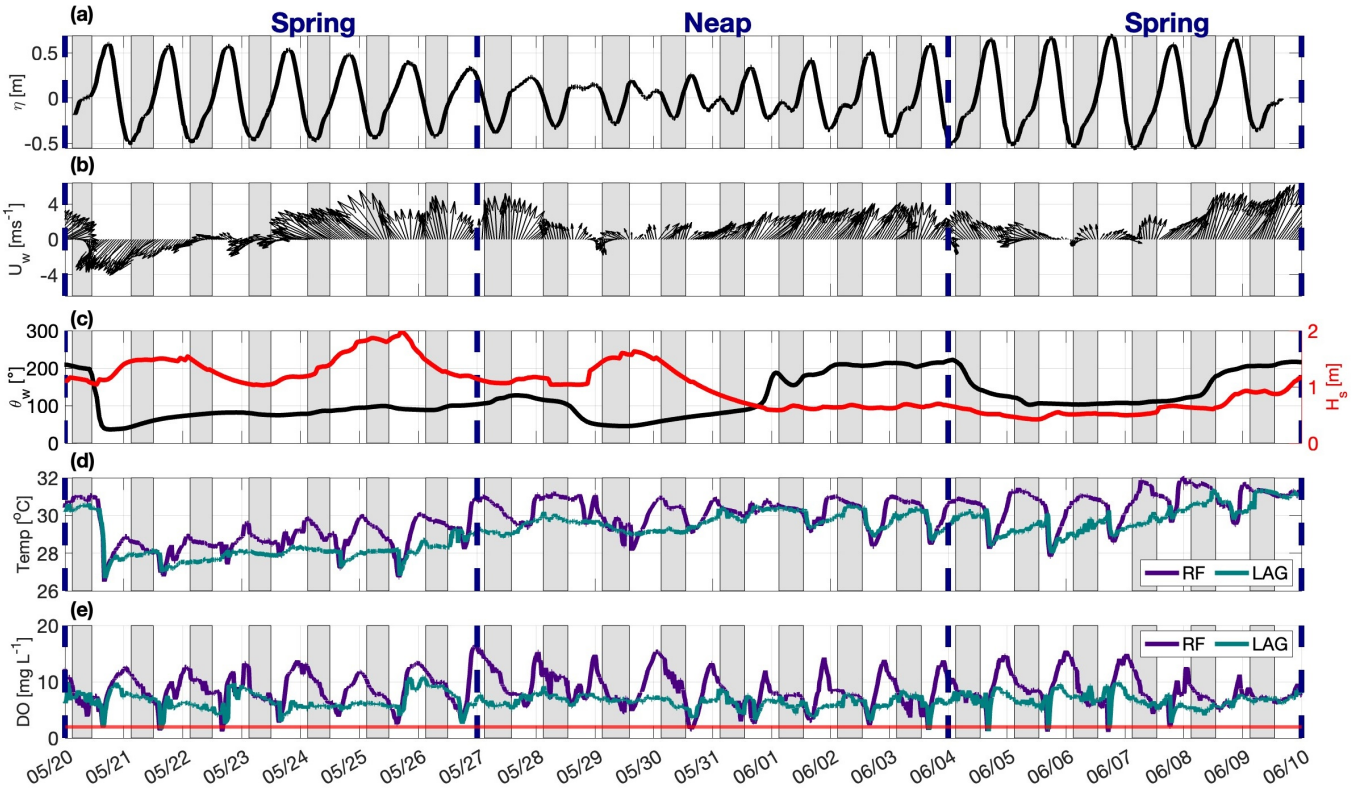

Figure 4.3: Oceanographic and meteorological data throughout deployment in local time: a) tidal water level from SBE37 on north lagoon mooring at 3.6 m depth, bandpass filtered from 4 to 60 hours. b) Wind direction and magnitude from ECMWF ERA5 (upward north). c) Offshore wave direction (left, 0 degrees from the north) and significant wave height (right) from ECMWF ERA5. d) Temperature on the east reef flat at 2.6 m depth (purple) and inside the east lagoon at 10 m depth (teal). e) Dissolved Oxygen on the east reef flat at 2.6 m depth (purple) and inside the east lagoon at 10 m depth (teal). Red line indicates hypoxia (2 mgŁ$^{-1}$).

4.3.2 Reef flat circulation

Flow on the reef flat was measured at one location (Fig. 1c), but water temperature was measured over a 2km section of the reef flat with the DTS cable, so here we use a reef flat heat budget to test our assumption about transport estimates from our limited flow measurements. Water temperature across the reef flat is estimated from the heat budget (Equation 4.3, in which advective transport of heat is estimated from the RF ADCP (Figure 4.1c)) is compared to water temperature measured by the DTS over a composite day (Figure 4.4b,d). The daily composite heat budget captures 90 % of the variance in the DTS data with a Wilmott Skill Score of 0.94 (Figure 4.4c,e). The mean temperature is coolest near the reef crest, with an average temperature of 29.1 °C, compared to 29.9 °C at the reef-lagoon boundary.

We assume a temporally varying, but spatially homogeneous water level (η) across the reef, as discussed in the Methods. There are periods near the reef crest during spring tide when the amplitude of η is greater than the reef flat depth. In order to maintain continuity in the heat budget model, we therefore imposed a minimum depth of 0.1 m. Based on observations presented in Merrigan et al. (b) (in review), the transport on the reef flat is likely hydraulically disconnected during these periods. We are thus likely over-predicting transport in the shallow regions of the reef during these periods, leading to an amplification of transport on the reef flat. Despite these discrepancies, the good agreement between the predicted and observed water temperature across the reef flat indicates that transport on the east reef flat is adequately represented by the flow measurements at the ADCP site.

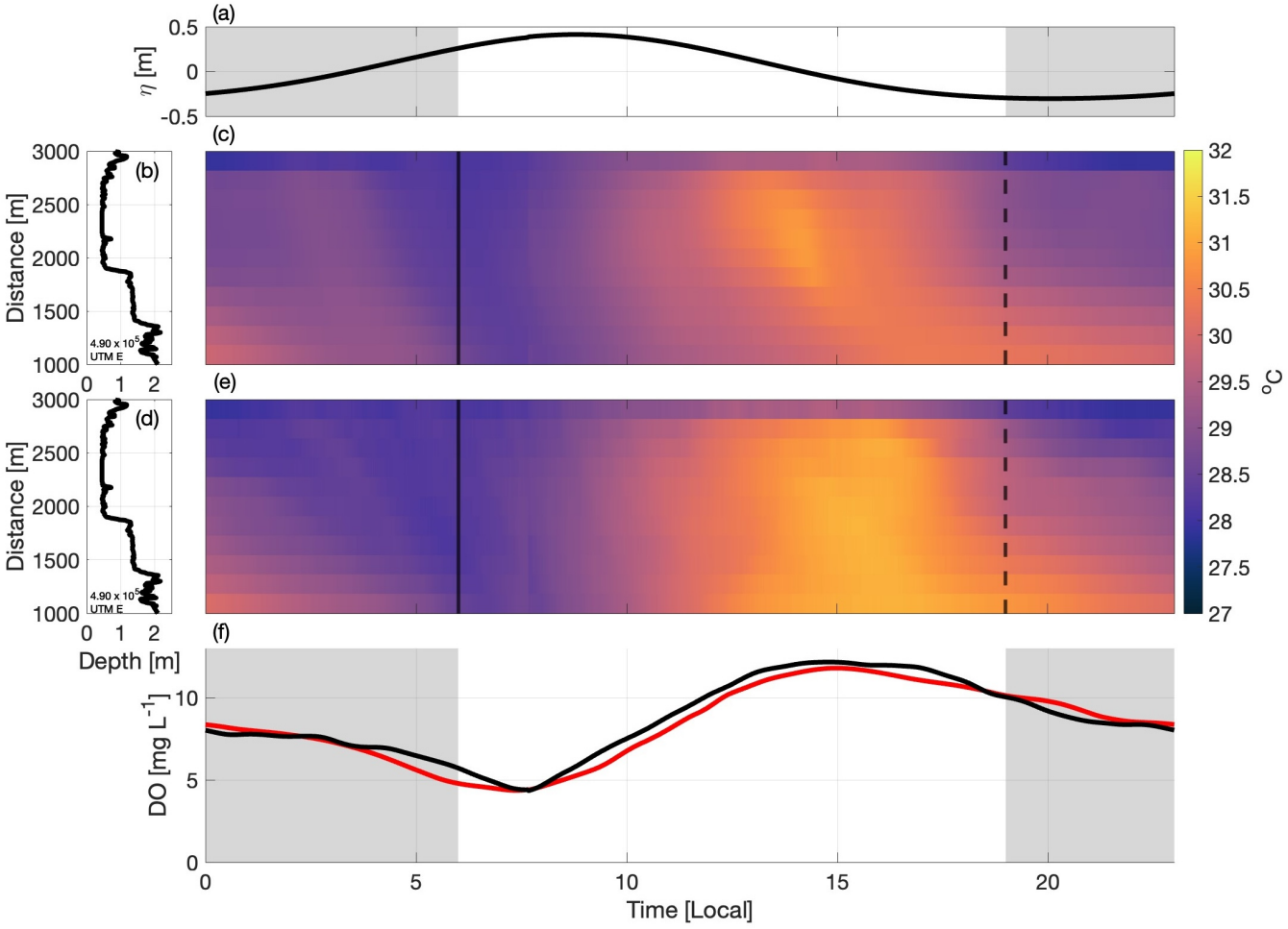

Figure 4.4: a) Daily composite average of free surface elevation. Gray shaded regions indicate night. b) and d) plot the bathymetric depth along the east reef cross section originating at the DTS station to the reef crest where distance denotes distance from lagoon boundary. c) Daily composite average of cross east reef DTS temperature originating at DTS station through the reef crest. Solid line denotes sunrise and dashed line denotes sunset. f) Daily composite average of the reef flat heat budget (Equation 4.3) originating at DTS station through the reef crest. Solid line denotes sunrise and dashed line denotes sunset. Both c) and f) are plotted on same color axis. f) Daily composite average of oxygen, observed east reef flat sensor (black) and oxygen budget (Equation 4.7) (red). Gray shaded regions indicate night.

4.3.3 The Oxygen Budget

An oxygen budget for the Dongsha Atoll east reef flat is calculated from Equation 4.7. The daily composite averaged dissolved oxygen budget output at the RF DO sensor is compared to 1-hr lowpass filtered oxygen observations, with an $R^2 = 0.96$ (Figure 4.4f). During the day, primary production is much greater than the respiration rate, driving increases in dissolved oxygen with a peak oxygen concentration of nearly 15 mg L^{-1}. At night when there is no primary production, strong biological respiration draws oxygen down, often to hypoxic and anoxic levels. This oxygen drawdown is especially prevalent near the reef crest, where shallow depths lead to dramatic levels of drawdown, as the respiration of benthic organisms consumes oxygen from a smaller volume of water.

During periods of lagoonward flow at night, advection transports low-oxygen water from the shallower reef crest region towards the reef-lagoon boundary, resulting in sharp, low oxygen pulses at the end of night or early morning (Figure 4.5b,d), similar to those seen in the observed oxygen signal at the reef-flat lagoon boundary (Figure 4.4f). This is a persistent pattern in the oxygen variability across the reef during the study period as the diurnal tides, the dominant driver of flow over the reef flat, are nearly phase-locked with the diurnal biological cycle of primary production and respiration on the reef.

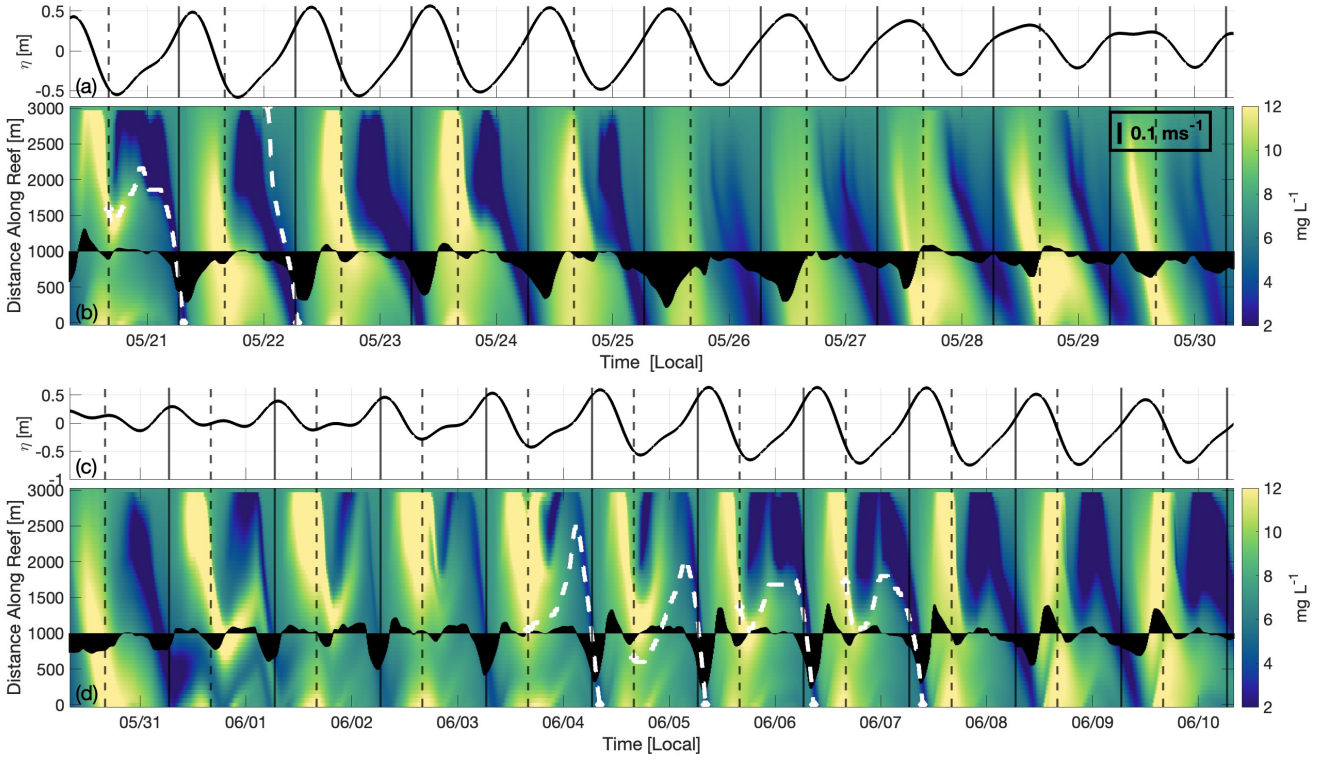

Figure 4.5: a) and b) show the free surface tidal elevation for 20-30 May and 31 May - 20 June, respectively. c) and d) depict the cross-reef oxygen budget from Equation 4.7, colored by oxygen concentration. 0 m is the lagoonward edge of the reef and 3000 m is the reef crest. Vertical black dashed lines denote beginning of oxygen-night, vertical solid lines denote end of oxygen-night. White dashed lines depict particle tracks started on the reef edge 15-minutes prior to observed low oxygen events inside the lagoon, tracked backwards in time. Black quivers show the 1-hr lowpass filtered cross-reef velocity at the east reef flat ADCP.

4.3.4 Physical drivers of oxygen variability across the reef flat

The origin and residence time of water plays a critical role in shaping the oxygen dynamics across the reef flat. To estimate residence time, particles were released 15-minutes preceding low oxygen events in the lagoon (Experiment A) and at the reef-lagoon boundary every 30-minutes throughout oxygen night (Experiment B). The net oxygen consumption within a given water mass (particle track) at night on the reef flat is related to its residence time and the average depth of the water column over the particle path as shown in Figure 4.6a for both particle tracking Experiments A and B. In general, the net rate of oxygen consumption on the reef flat at night is represented by the red line in Figure 4.6a and is equal to the respiration rate divided by the average depth of the reef flat. Deviations of the oxygen consumption along individual particle paths in Figure 4.6a from the red line are due to differences in the depth along those particle paths relative to the reef flat average depth, since the modeled respiration rate is spatially homogenous (Figure 4.6b).

The formation of hypoxia (< 2 mg L^{-1}) is dependent both on the net oxygen consumption along a particle path and the initial oxygen concentration at the beginning of oxygen night. Average offshore dissolved oxygen at night is 7.2 mg L^{-1}, while the average cross-reef dissolved oxygen at the beginning of oxygen-night is 11 mg L^{-1}.

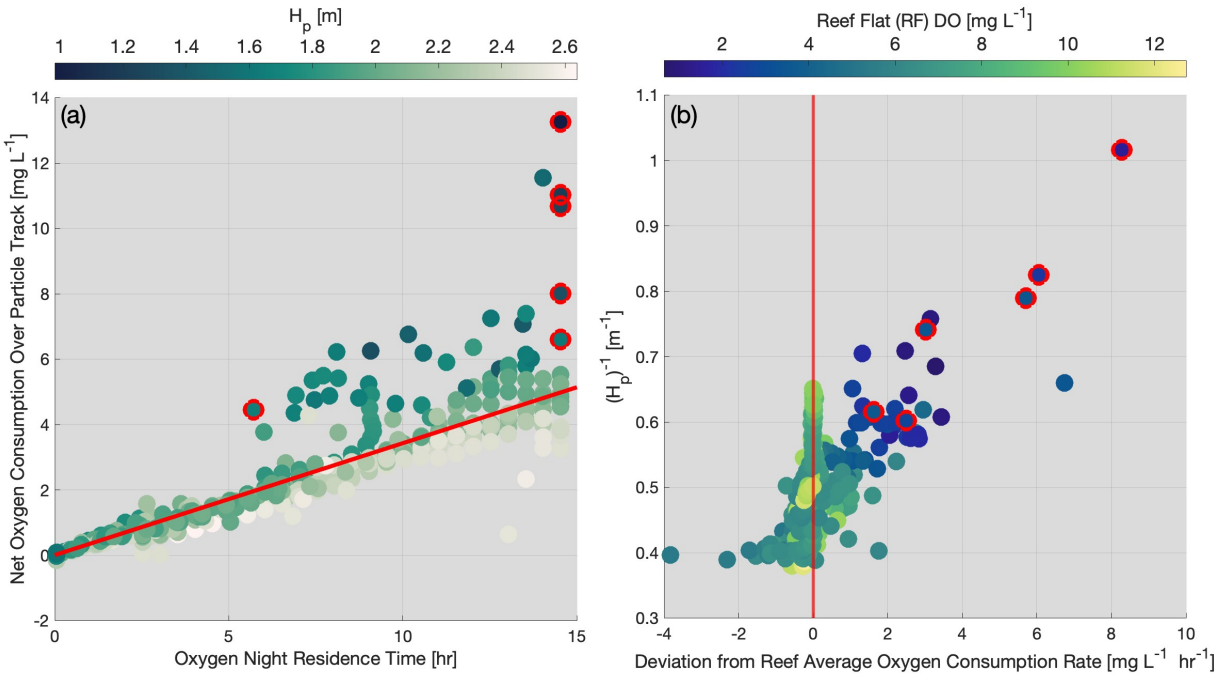

Figure 4.6: a) Scatter plot of the residence time during oxygen-night of a particle versus the net oxygen consumption over the particle path colored by (H_p), the average depth along the particle path. Particles are released at the lagoon edge of the reef flat throughout oxygen-night. Points circled in red were released 15-minutes prior to observed hypoxic events inside the lagoon. The red line indicates average oxygen drawdown with time. b) Scatter plot of particles deviation from the red line in a) versus $(H_p)^{-1}$, colored by the dissolved oxygen concentration at the lagoon-reef boundary, or where the particles were released.

The observed hypoxic events follow similar patterns to Experiment B. All but one of the particle paths corresponding to observed hypoxic events (Experiment A, circles with red outlines in Figure 4.6) had residence times of 14 hours, and thus spent all of oxygen-night on the shallow reef flat (Figure 4.6a). Furthermore, the average water depth over these particle paths was shallower than the average reef depth because they spent most of their time in the shallow oceanward side of the reef flat, where the net oxygen consumption was high (Figure 4.6b). One of the observed hypoxic events in Experiment A on 23 May 2019 had a shorter residence time (6 hours) but was traced to a water mass originating offshore which had a much lower initial concentration of oxygen (8 mg L^{-1} at the start of oxygen-night) compared to the oxygen concentration for water masses at the start of oxygen night. For Experiment A, the greatest rates of oxygen drawdown occured between 2000-2500 m along the reef– where the average decrease in oxygen concentration was nearly 3 mg L^{-1}– despite only spending 11% of their total path in that section of the reef (Figure 4.7).

The time to hypoxia is defined by the amount of time it takes a system to deplete its initial oxygen supplies C_{O_2} from respiration RR alone (Fennel and Testa, 2019),

$$\tau_{O_2} = \frac{C_{O_2}}{F_R}. \tag{4.9}$$

Here, C_{O_2} is defined as the beginning-of-night cross-reef oxygen concentration of 11 mg L^{-1} and F_R is the depth dependent respiration rate. Assuming an average depth along the particle path, the time to $\tau_{O_2} = 2.8$ hours on this section of the reef (Figure 4.7). All observed hypoxic events tracked in Experiment A correspond to spring tidal conditions, during which the larger tidal forcing results in increased transport across the reef flat. The average tidal excursion length of these particles is 2200 m, allowing for water parcels to be advected from the shallow part of the reef flat, with shorter τ_{O_2}, to the lagoon edge.

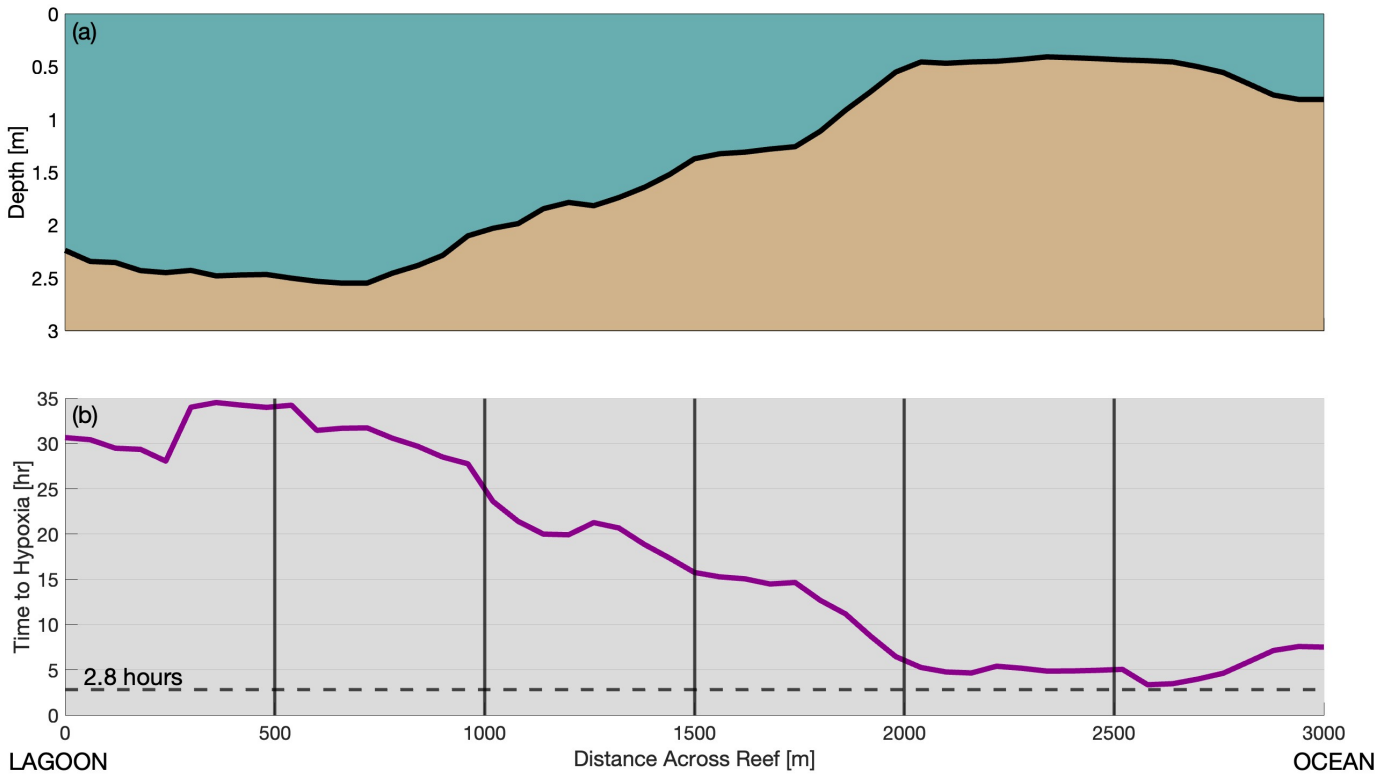

Figure 4.7: a) Smoothed bathymetry from LIDAR data on the east reef flat. c) The time to hypoxia, or the amount of time it takes to drawdown oxygen to hypoxia levels from the average cross reef oxygen concentration at the beginning of night, based on the average depth along the particle paths. The dashed line indicates the overall minimum time to hypoxia of 2.8-hours between 2000-25000 m on the east reef flat.

4.4 Discussion

The influence of diurnal physical and biogeochemical processes on reef flat oxygen

Our study only encompasses a three-week period during summer, and although we are able to capture some variation in wave forcing and temperature, we employ an idealized model in order to better understand the influence of wave forcing and seasonal fluctuations in temperature on residence time and the formation of low-oxygen water on the reef. In this idealized model, we estimate flow across the reef due to tide and surface wave forcing only. Tidal flow is estimated from tidal elevation models (TPXO8, Egbert and Erofeeva (2002)) and reef flat flow modeled from the momentum budget of Merrigan et al. (b) (in review) for a period when waves were low (01-07 June). The linear fit captures 62% of the variance in the momentum budget flow model.

To estimate primary production and respiration rates over a year, we implemented the functional dependence of primary production rates and respiration rates on temperature from work on Hawaiian reefs in Jokiel and Coles (1977). Using the observed night time averaged temperature on the reef from the east reef flat dissolved oxygen sensor sampling from March 2019 through February 2020, we estimated respiration and primary production rates throughout the year based on the relative change in temperature and our established respiration and primary production rates for our study period. During the 50-day gap in temperature measurements February to March 2020, we applied a linear interpolation to obtain an estimate of night-time temperature. Winter respiration rates are approximately half of those in the summer (Jokiel and Coles, 1977). The difference in the maximum primary production from winter to summer is less pronounced, with only a 10% reduction in winter primary production rate compared to summer.

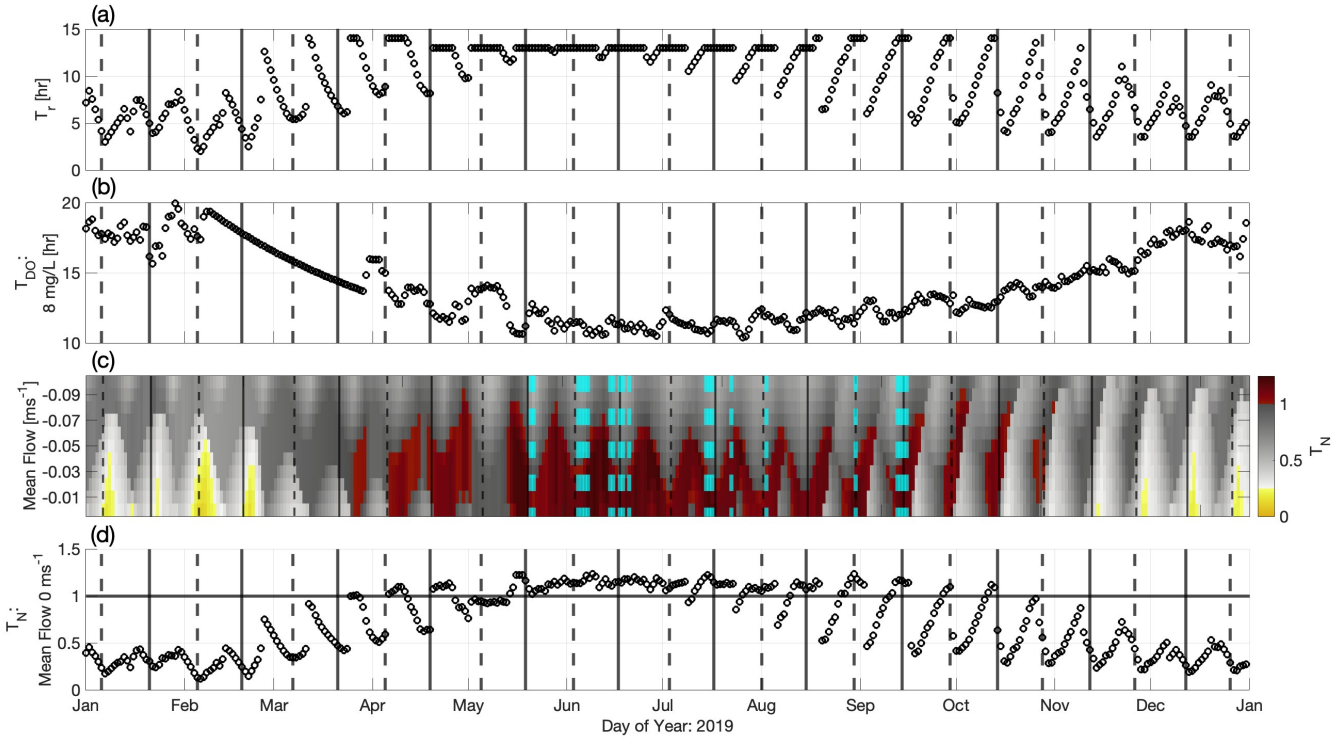

Figure 4.8: a) The maximum oxygen night residence time (T_r) for day of year in 2019 estimated from the linear flow model for a mean flow of zero. b) The time to 8 mgL^1 drawdown for day of year in 2019 based on a depth of 1 m with respiration rates extrapolated for the year from Jokiel and Coles (1977) using average night temperature observations on the east reef flat (T_{DO}). c) The normalized residence time (T_N), defined as the maximum residence time normalized by the drawdown time plotted for day of year in 2019 on the x-axis and mean flow, varying from 0 to -0.1 m s^{-1} on the y-axis. Values greater than on indicate periods when the residence time is greater than the time to drawdown, leaving the system susceptible to hypoxia formation. d) The normalized residence time for a mean flow of 0 m s^{-1}. Blue dashed lines are observed hypoxic events inside the east lagoon from observations in 2019. In all plots, black dashed vertical lines are new moons and black solid are full moons.

We used shortwave radiation from ECMWF to determine the length of night throughout year and the associated times of sunset and sunrise. The length of night varies from 13 hours to 11 hours between winter and summer, respectively. Using this information together with the estimated maximum primary production rate for each day, we created a primary production curve for each day of the year (Falter et al., 2013), which we use to establish oxygen-night start, end, and overall duration.

We then released particles every 30-minutes during oxygen-night and tracked them backwards in time to find the maximum oxygen-night residence time (T_r) for each night of the year (Figure 4.8a). For our idealized system, we assume a constant depth of 1 m without depth fluctuations due to η. Next, we estimate the time it takes to draw down oxygen by 8 mg L^{-1} in 1 meter of water depth, T_{DO}. (Figure 4.8b). The 8 mg L^{-1} benchmark is the oxygen decrease necessary to draw down the average beginning of oxygen-night reef flat oxygen concentration (10 mg L^{-1}) to hypoxic levels.

T_N is the normalized residence time calculated by dividing the T_r by T_{DO} (Figure 4.8c). When T_N exceeds one, water stays on the reef long enough to draw down oxygen to hypoxic levels if starting at the average beginning-of-night concentration. When T_N is less than one, the T_{DO} exceeds the T_r (Figure 4.8c), preventing hypoxia from forming.

There is a pronounced fortnightly signal (Figure 4.8c,d) in T_N, primarily modulated by T_r due to fluctuations in tidal (spring-neap) forcing, with longer residence times corresponding to spring tidal forcing. A seasonal cycle in T_N exists that is dependent on the seasonal temperature and resultant respiration rate and T_{DO}, in which T_N peaks in the summer and tapers off in the winter (Figure 4.8b,c).

The mean flow produced by the linear fit is set to 0 $m\,s^{-1}$ and then decreased in increments of -0.01 $m\,s^{-1}$ to -0.1 $m\,s^{-1}$ to simulate the effects of wave forcing on driving lagoonward flow on the reef flat flow (Figure 4.8c). When wave forcing is increased in the lagoonward

direction, T_r decreases, which subsequently decreases the periods when T_N is greater than 1 (Figure 4.8c). These idealized results suggest hypoxia is more probable during summer months, when respiration rates are higher due to warmer temperatures. This is exacerbated during periods of low wave forcing, which increase T_r and allow for further dissolved oxygen drawdown.

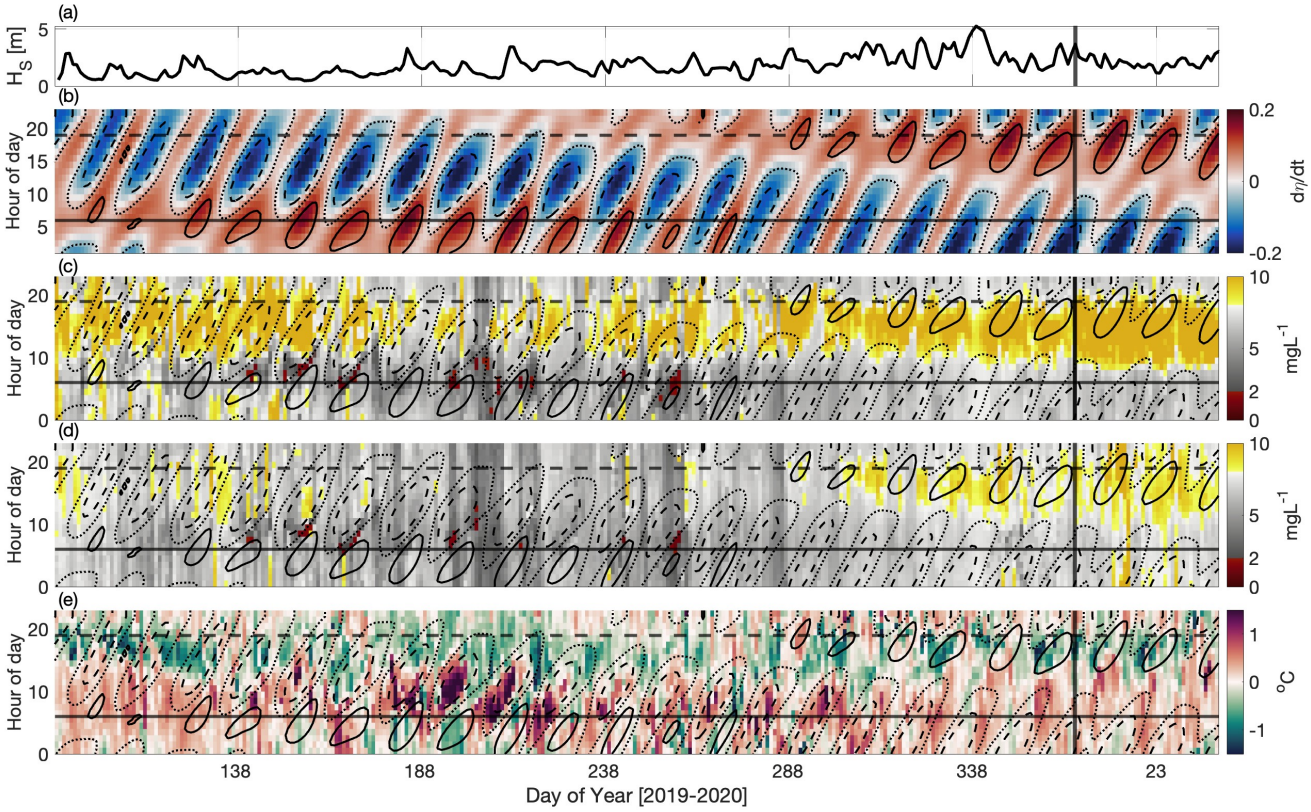

Figure 4.9: Starting March 2019 through February 2020 where black vertical line indicates change in year: a) Daily average significant wave height from ECMWF, b) Hourly $\frac{d\eta}{dt}$ where positive (red) indicates flood tide and negative (blue) indicates ebb tide from the TPXO8 Tidal Model. c) and d) Hourly dissolved oxygen data on the east reef flat and east lagoon, respectively. Red indicates oxygen concentrations below 2 mg L^1 and yellow indicated dissolved oxygen concentrations above 8 mg L^1. e) Hourly difference in temperature between the east lagoon temperature sensor and east reef flat temperature sensor where negative indicates cooler reef flat water relative to the lagoon. Solid and dashed contours are along 0.1 m and -0.1 m, respectively, and dashed contours are along 0 m. Solid horizontal line denotes the average time of sunrise and the dashed horizontal line denotes the average time of sunset.

4.4.1 Seasonal hypoxia trends on Dongsha Atoll

The previous section highlighted the role of residence time and temperature dependent respiration rate on the formation of hypoxia on the reef flat. From approximately 1-year of temperature and dissolved oxygen data on the east reef, spanning from March 2019 through February 2020 (Figure 4.9c), all low oxygen events occurred during periods when the normalized residence time is greater than one (Figure 4.8c). These events are observed near sunrise and primarily correspond to periods with flood tide at night and low wave forcing (Figure 4.9a,b). The reef flat low oxygen events are echoed in the east lagoon dissolved oxygen signal, with hypoxia observed 15-30 minutes lagged of the east reef flat signal (Figure 4.9d). These signals also correspond to periods of time when reef flat water is cooler and denser than lagoon bottom water (Figure 4.9e), allowing for bottom water renewal events that replenish the bottom lagoon waters with hypoxic water, as observed in Merrigan et al. (a) (in prep).

Temperature on the reef is influenced both by internal waves and convective cooling at night. From a simple back-of-the-envelope calculation, average net observed night time surface heat fluxes can cool 1 m of water $\sim 1.5°C$ over a 12-hour period. Similar to the oxygen budget, cooling occurs at an increased rate in shallow regions, making the section near the reef crest, which is both shallow and strongly influenced by internal waves, conducive to strong cooling relative to the rest of the reef flat. Based on these observations and oxygen particle tracking results, water parcels that spend time on this section of the reef are likely to be both cooler and lower in oxygen. These water masses are then advected to the reef edge by strong tidally-forced flow during spring tidal regimes.

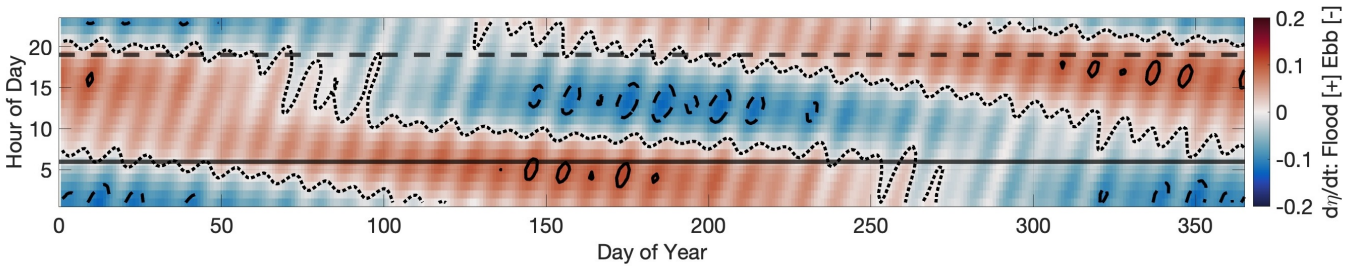

Figure 4.10: A 20 year average in hourly $\frac{d\eta}{dt}$ where positive (red) indicates flood tide and negative (blue) indicates ebb tide from the TPXO8 Tidal Model from 2000 through 2020. Solid and dashed contours are along 0.1 m and -0.1 m, respectively, and dashed contours are along 0 m. Solid horizontal line denotes the average time of sunrise and the dashed horizontal line denotes the average time of sunset.

4.4.2 Implications for the formation of hypoxia in coral reef systems

Though observations of temperature and dissolved oxygen for this paper are limited to a single year, tidal data is reproducible for many years through the TPXO tidal model. We have shown that hypoxic events on the reef flat and inside the lagoon occur during flood tide (or when $\frac{d\eta}{dt}$ is positive) at night, which occurs during the summer in 2019. Over a 20-year average of $\frac{d\eta}{dt}$ (Figure 4.10), this tidal phasing of flood-at-night is seasonally locked, consistently occurring during the summer. Due to the primarily diurnal tides on Dongsha Atoll, this tidal pattern is repeatable on a yearly cycle. Combined with seasonal heating trends, with warmest temperatures and highest respiration rates during the summer, this seasonally phase-locked pattern creates a seasonal risk for hypoxia on Dongsha Atoll. This is further compounded by the reduced oxygen solubility in warmer waters and the overall thermal stress induced by increased water temperatures on coral reef ecosystems.

Although this study specifically focuses on Dongsha Atoll, this phasing is likely relevant to other reef systems with diurnal tides due to the seasonality of both tides and temperature. While some studies (Lowe et al., 2016) and Buckee et al. (2022) have examined the influence of diurnal tides on reef thermal variability, little attention has been given to their influence

on dissolved oxygen variability. Furthermore, Altieri and Gedan (2015) highlights the overall lack of studies of hypoxia in the tropics, which are likely dramatically under reported. This paper underscores the need for additional exploration into oxygen dynamics on coral reefs with diurnal tides and emphasizes the compounded role of hypoxia as a stressor in coral reef systems.

4.5 Conclusion

Oxygen dynamics on the east reef flat of Dongsha Atoll are controlled by both physical processes and biological oxygen production and consumption. At night, strong biological respiration can draw down oxygen to hypoxic levels, especially in shallow regions of the reef where hypoxic conditions can form in as little as one hour. This hypoxic water is then transported across the wide reef flat by tidally driven advection, which was dominantly lagoonward at night during the study period, due to the locked phasing of the primarily diurnal tides and the solar cycle. From $\sim$ 1-year of dissolved oxygen data on the east reef flat, hypoxic events are consistently observed when this flood-at-night tidal phasing persists. Additionally, these hypoxic events on the reef flat correspond with hypoxic pulses at 10-m depth inside the east lagoon, highlighting a mechanism for the formation of hypoxia through advective processes, contrary to conventional understanding of hypoxia formation in semi-enclosed basins (Fennel and Testa, 2019)..

20-years of tidal model output shows that flood-at-night tidal phasing on Dongsha Atoll is seasonal, occurring during summer months, and leading to elevated hypoxia risk compounding with temperature induced thermal stress and reduced oxygen solubility. Though this study focuses on Dongsha Atoll, this tidal phasing is likely important in other reef systems with diurnal tides, motivating further work to understand oxygen dynamics in the coastal tropics.

Bibliography

Adelson, A. E., and Coauthors, 2022: Seasonal hypoxia and temperature inversions in a tropical bay. *Limnology and Oceanography*, **67 (10)**, 2174–2189.

Alford, M. H., and Coauthors, 2015: The formation and fate of internal waves in the south china sea. *Nature*, **521 (7550)**, 65–69.

Altieri, A. H., and K. B. Gedan, 2015: Climate change and dead zones. *Global change biology*, **21 (4)**, 1395–1406.

Altieri, A. H., S. B. Harrison, J. Seemann, R. Collin, R. J. Diaz, and N. Knowlton, 2017: Tropical dead zones and mass mortalities on coral reefs. *Proceedings of the National Academy of Sciences*, **114 (14)**, 3660–3665.

Andréfouët, S., M. Claereboudt, P. Matsakis, J. Pagès, and P. Dufour, 2001: Typology of atoll rims in tuamotu archipelago (french polynesia) at landscape scale using spot hrv images. *International Journal of Remote Sensing*, **22 (6)**, 987–1004

Andréfouët, S., C. Dutheil, C. E. Menkes, M. Bador, and M. Lengaigne, 2015: Mass mortality events in atoll lagoons: environmental control and increased future vulnerability. *Global Change Biology*, **21 (1)**, 195–205.

Arneborg, L., C. P. Erlandsson, B. Liljebladh, and A. Stigebrandt, 2004: The rate of inflow and mixing during deep-water renewal in a sill fjord. *Limnology and Oceanography*, **49 (3)**, 768–777

Bates, N. R., 2017: Twenty years of marine carbon cycle observations at Devils Hole Bermuda provide insights into seasonal hypoxia, coral reef calcification, and ocean acidification. *Frontiers in Marine Science*, **4**, 36.

Benjamin, T. B., 1968: Gravity currents and related phenomena. *Journal of fluid mechanics*, **31 (2)**, 209–248.

Best, M., A. Wither, and S. Coates, 2007: Dissolved oxygen as a physico-chemical supporting element in the water framework directive. *Marine pollution bulletin*, **55 (1-6)**, 53–64

Bianchi, T. S., S. F. DiMarco, J. Cowan Jr, R. D. Hetland, P. Chapman, J. Day, and M. Allison, 2010: The science of hypoxia in the Northern Gulf of Mexico: a review. *Science of the Total Environment*, **408 (7)**, 1471–1484.

Bicchi, E., J.-P. Debenay, and J. Pages, 2002: Relationship between benthic foraminiferal assemblages and environmental factors in atoll lagoons of the central Tuamotu Archipelago (French Polynesia). *Coral Reefs*, **21 (3)**, 275–290.

Boesch, D. F., and N. N. Rabalais, 1991: Effects of hypoxia on continental shelf benthos: comparisons between the new york bight and the northern gulf of mexico. *Geological Society, London, Special Publications*, **58 (1)**, 27–34.

Bograd, S. J., F. B. Schwing, C. G. Castro, and D. A. Timothy, 2002: Bottom water renewal in the santa barbara basin. *Journal of Geophysical Research: Oceans*, **107 (C12)**, 9–1–9–9

Bopp, L., and Coauthors, 2013: Multiple stressors of ocean ecosystems in the 21st century: projections with cmip5 models. *Biogeosciences*, **10 (10)**, 6225–6245.

Borsuk, M., C. Stow, R. Luettich Jr, H. Paerl, and J. Pinckney, 2001: Modelling oxygen dynamics in an intermittently stratified estuary: estimation of process rates using field data. *Estuarine, Coastal and Shelf Science*, **52 (1)**, 33–49.

Breitburg, D., and Coauthors, 2018: Declining oxygen in the global ocean and coastal waters. *Science*, **359 (6371)**, eaam7240.

Brown, J. H., J. F. Gillooly, A. P. Allen, V. M. Savage, and G. B. West, 2004: Toward a metabolic theory of ecology. *Ecology*, **85 (7)**, 1771–1789.

Buckee, J., Y. Hetzel, W. Edge, J. Verduin, and C. Pattiaratchi, 2022: Daily timing of low tide drives seasonality in intertidal emersion mortality risk. *Frontiers in Marine Science*, **9**, 904 191.

Callaghan, D. P., P. Nielsen, N. Cartwright, M. R. Gourlay, and T. E. Baldock, 2006: Atoll lagoon flushing forced by waves. *Coastal Engineering*, **53 (8)**, 691–704

Chan, F., J. Barth, J. Lubchenco, A. Kirincich, H. Weeks, W. T. Peterson, and B. Menge, 2008: Emergence of anoxia in the california current large marine ecosystem. *Science*, **319 (5865)**, 920–920.

Chen, C., and H.-L. Lin, 2017: Applying benthic foraminiferal assemblage to evaluate the coral reef condition in Dongsha Atoll lagoon. *Zoological studies*, **56**.

Chen, S.-M., 2023: Water exchange due to wind and waves in a monsoon prevailing tropical atoll. *Journal of Marine Science and Engineering*, **11 (1)**, 109.

Costa, M. B., E. C. Macedo, A. Valle-Levinson, and E. Siegle, 2017: Wave and tidal flushing in a near-equatorial mesotidal atoll. *Coral Reefs*, **36 (1)**, 277–291

Dai, C., 2004: Dongsha Atoll in the South China Sea: Past, present and future. *Islands of the world VIII international conference, Kinmen Island, Taiwan.*

Davis, K., S. Lentz, J. Pineda, J. Farrar, V. Starczak, and J. Churchill, 2011: Observations of the thermal environment on red sea platform reefs: a heat budget analysis. *Coral Reefs*, **30**, 25–36.

Davis, K. A., R. S. Arthur, E. C. Reid, J. S. Rogers, O. B. Fringer, T. M. DeCarlo, and A. L. Cohen, 2020: Fate of internal waves on a shallow shelf. *Journal of Geophysical Research: Oceans*, e2019JC015377.

Davis, K. A., G. Pawlak, and S. G. Monismith, 2021: Turbulence and coral reefs. *Annual review of marine science*, **13**, 343–373.

DeCarlo, T. M., A. L. Cohen, G. T. Wong, K. A. Davis, P. Lohmann, and K. Soong, 2017a: Mass coral mortality under local amplification of 2 c ocean warming. *Scientific reports*, **7 (1)**, 1–9.

DeCarlo, T. M., A. L. Cohen, G. T. Wong, F.-K. Shiah, S. J. Lentz, K. A. Davis, K. E. Shamberger, and P. Lohmann, 2017b: Community production modulates coral reef ph and the sensitivity of ecosystem calcification to ocean acidification. *Journal of Geophysical Research: Oceans*, **122 (1)**, 745–761.

Diaz, R. J., 2001: Overview of hypoxia around the world. *Journal of Environmental Quality*, **30 (2)**, 275–281.

Diaz, R. J., and R. Rosenberg, 2008: Spreading dead zones and consequences for marine ecosystems. *science*, **321 (5891)**, 926–929

Dumas, F., R. Le Gendre, Y. Thomas, and S. Andréfouët, 2012: Tidal flushing and wind driven circulation of ahe atoll lagoon (tuamotu archipelago, french polynesia) from in situ observations and numerical modelling. *Marine Pollution Bulletin*, **65 (10-12)**, 425–440

D'Avanzo, C., and J. N. Kremer, 1994: Diel oxygen dynamics and anoxic events in an eutrophic estuary of waquoit bay, massachusetts. *Estuaries*, **17**, 131–139.

Egbert, G. D., and S. Y. Erofeeva, 2002: Efficient inverse modeling of barotropic ocean tides. *Journal of Atmospheric and Oceanic technology*, **19 (2)**, 183–204.

Fabricius, K. E., 2005: Effects of terrestrial runoff on the ecology of corals and coral reefs: review and synthesis. *Marine pollution bulletin*, **50 (2)**, 125–146.

Fairall, C., E. Bradley, J. Hare, A. Grachev, and J. Edson, 2003: Bulk parameterization of air-sea fluxes: Updates and verification for the coare algorithm. *Journal of Climate*, **16 (4)**, 571–591.

Fairall, C., E. Bradley, D. Rogers, J. Edson, and G. Young, 1996: Bulk parameterization of air-sea fluxes for tropical ocean-global atmosphere coupled-ocean atmosphere response experiment. *Journal of Geophysical Research*, **101 (C2)**, 3747–3764.

Falter, J. L., M. J. Atkinson, and M. A. Merrifield, 2004: Mass-transfer limitation of nutrient uptake by a wave-dominated reef flat community. *Limnology and Oceanography*, **49 (5)**, 1820–1831

Falter, J. L., R. J. Lowe, Z. Zhang, and M. McCulloch, 2013: Physical and biological controls on the carbonate chemistry of coral reef waters: effects of metabolism, wave forcing, sea level, and geomorphology. *PloS one*, **8 (1)**, e53 303.

Farmer, D. M., and H. J. Freeland, 1983: The physical oceanography of fjords. *Progress in oceanography*, **12 (2)**, 147–219.

Fennel, K., and J. M. Testa, 2019: Biogeochemical controls on coastal hypoxia. *Annual review of marine science*, **11**, 105–130.

Frölicher, T. L., E. M. Fischer, and N. Gruber, 2018: Marine heatwaves under global warming. *Nature*, **560 (7718)**, 360–364.

Gade, H., and A. Edwards, 1980: Deep water renewal in fjords. *Fjord oceanography*, 453–489.

Gajdzik, L., and T. M. DeCarlo, 2017: The perfect calm: Reoccurring mass die-offs on a remote coral atoll. *Matters*, **3 (9)**, e201707000 003.

Geyer, W., and G. Cannon, 1982: Sill processes related to deep water renewal in a fjord. *Journal of Geophysical Research: Oceans*, **87 (C10)**, 7985–7996

Gilbert, D., N. N. Rabalais, R. J. Diaz, and J. Zhang, 2010: Evidence for greater oxygen decline rates in the coastal ocean than in the open ocean. *Biogeosciences*, **7 (7)**, 2283–2296.

Gill, A. E., 1982: *Atmoshpere-Ocean Dynamics*. Academic Press, San Diego.

Gillibrand, P., W. Turrell, D. Moore, and R. Adams, 1996: Bottom water stagnation and oxygen depletion in a scottish sea loch. *Estuarine, Coastal and Shelf Science*, **43 (2)**, 217–235

Goldberg, W. M., 2016: Atolls of the world: revisiting the original checklist. *Atoll Research Bulletin*, **610**, 1–47.

Green, R. H., R. J. Lowe, and M. L. Buckley, 2018: Hydrodynamics of a tidally forced coral reef atoll. *Journal of Geophysical Research: Oceans*, **123 (10)**, 7084–7101

Gruber, R. K., R. J. Lowe, and J. L. Falter, 2017: Metabolism of a tide-dominated reef platform subject to extreme diel temperature and oxygen variations. *Limnology and Oceanography*, **62 (4)**, 1701–1717

Hartstein, N. D., J. D. Maxey, J. C. H. Loo, and A. Y.-H. Then, 2019: Drivers of deep water renewal in macquarie harbour, tasmania. *Journal of Marine Systems*, **199**, 103 226

Hausner, M. B., F. Suárez, K. E. Glander, N. Van de Giesen, J. S. Selker, and S. W. Tyler, 2011: Calibrating single-ended fiber-optic raman spectra distributed temperature sensing data. *Sensors*, **11 (11)**, 10 859–10 879.

Hench, J. L., J. J. Leichter, and S. G. Monismith, 2008: Episodic circulation and exchange in a wave-driven coral reef and lagoon system. *Limnology and Oceanography*, **53 (6)**, 2681–2694

Hersbach, H., and Coauthors, 2020: The era5 global reanalysis. *Quarterly Journal of the Royal Meteorological Society*, **146 (730)**, 1999–2049.

Howarth, R. W., 2008: Coastal nitrogen pollution: a review of sources and trends globally and regionally. *Harmful algae*, **8 (1)**, 14–20.

Jokiel, P. L., and S. Coles, 1977: Effects of temperature on the mortality and growth of hawaiian reef corals. *Marine Biology*, **43**, 201–208.

Kealoha, A. K., S. M. Doyle, K. E. F. Shamberger, J. B. Sylvan, R. D. Hetland, and S. F. DiMarco, 2020: Localized hypoxia may have caused coral reef mortality at the flower garden banks. *Coral Reefs*, **39 (1)**, 119–132, doi:10.1007/s00338-019-01883-9, URL https://doi.org/10.1007/s00338-019-01883-9.

Keeling, R. F., A. Körtzinger, and N. Gruber, 2010: Ocean deoxygenation in a warming world. *Annual review of marine science*, **2**, 199–229.

Kemp, W., J. M. Testa, D. J. Conley, D. Gilbert, and J. D. Hagy, 2009a: Temporal responses of coastal hypoxia to nutrient loading and physical controls. *Biogeosciences*, **6 (12)**, 2985–3008.

Kemp, W., J. M. Testa, D. J. Conley, D. Gilbert, and J. D. Hagy, 2009b: Temporal responses of coastal hypoxia to nutrient loading and physical controls. *Biogeosciences*, **6 (12)**, 2985–3008.

Kinsey, D., and E. Kinsey, 1967: Diurnal changes in oxygen content of the water over the coral reef platform at heron i. *Marine and Freshwater Research*, **18 (1)**, 23–34.

Knauss, J., 1978: Underwater optics. *Introduction to Physical Oceanography, Prentice-Hall*, 262–267.

Kraines, S., Y. Suzuki, K. Yamada, and H. Komiyama, 1996: Separating biological and physical changes in dissolved oxygen concentration in a coral reef. *Limnology and Oceanography*, **41 (8)**, 1790–1799.

Kraines, S. B., A. Suzuki, T. Yanagi, M. Isobe, X. Guo, and H. Komiyama, 1999: Rapid water exchange between the lagoon and the open ocean at majuro atoll due to wind, waves, and tide. *Journal of Geophysical Research: Oceans*, **104 (C7)**, 15 635–15 653

Kwiatkowski, L., and Coauthors, 2020: Twenty-first century ocean warming, acidification, deoxygenation, and upper-ocean nutrient and primary production decline from cmip6 model projections. *Biogeosciences*, **17 (13)**, 3439–3470.

Lentz, S., K. Davis, J. Churchill, and T. DeCarlo, 2017: Coral reef drag coefficients–water depth dependence. *Journal of Physical Oceanography*, **47 (5)**, 1061–1075.

Li, Y., M. Li, and W. M. Kemp, 2015: A budget analysis of bottom-water dissolved oxygen in chesapeake bay. *Estuaries and Coasts*, **38 (6)**, 2132–2148.

Long, M. C., C. Deutsch, and T. Ito, 2016: Finding forced trends in oceanic oxygen. *Global Biogeochemical Cycles*, **30 (2)**, 381–397.

Long, M. H., J. E. Rheuban, D. C. McCorkle, D. J. Burdige, and R. C. Zimmerman, 2019: Closing the oxygen mass balance in shallow coastal ecosystems. *Limnology and Oceanography*, **64 (6)**, 2694–2708.

Lowe, R. J., X. Pivan, J. Falter, G. Symonds, and R. Gruber, 2016: Rising sea levels will reduce extreme temperature variations in tide-dominated reef habitats. *Science Advances*, **2 (8)**, e1600 825.

Maritorena, S., A. Morel, and B. Gentili, 1994: Diffuse reflectance of oceanic shallow waters: Influence of water depth and bottom albedo. *Limnology and oceanography*, **39 (7)**, 1689–1703.

McDougall, T. J., and P. M. Barker, 2011: Getting started with teos-10 and the gibbs seawater (gsw) oceanographic toolbox. *Scor/Iapso WG*, **127 (532)**, 1–28.

McGowan, H., A. Sturman, M. Saunders, A. Theobald, and A. Wiebe, 2019: Insights from a decade of research on coral reef—atmosphere energetics. *Journal of Geophysical Research: Atmospheres*, **124 (8)**, 4269–4282.

Merrigan, S. R., G. Pawlak, K.-H. Fu, and K. Davis, ????a: Physical processes shaping low-oxygen events in a highly flushed coral atoll lagoon. *In Review*.

Merrigan, S. R., G. Pawlak, G. Sinnett, K.-H. Fu, and K. Davis, ????b: Heat budget of a coral atoll lagoon and the effects of tidal and solar phasing. *In Review*.

Monsen, N. E., J. E. Cloern, L. V. Lucas, and S. G. Monismith, 2002: A comment on the use of flushing time, residence time, and age as transport time scales. *Limnology and oceanography*, **47 (5)**, 1545–1553.

Nelson, H. R., and A. H. Altieri, 2019: Oxygen: the universal currency on coral reefs. *Coral Reefs*, **38 (2)**, 177–198.

Nilsson, G. E., S. Östlund-Nilsson, and P. L. Munday, 2010: Effects of elevated temperature on coral reef fishes: loss of hypoxia tolerance and inability to acclimate. *Comparative Biochemistry and Physiology Part A: Molecular & Integrative Physiology*, **156 (4)**, 389–393.

Ohde, S., and R. van Woesik, 1999: Carbon dioxide flux and metabolic processes of a coral reef, okinawa. *Bulletin of Marine Science*, **65 (2)**, 559–576.

Pagès, J., S. Andrefouët, B. Delesalle, and V. Prasil, 2001: Hydrology and trophic state in takapoto atoll lagoon: comparison with other tuamotu lagoons. *Aquatic living resources*, **14 (3)**, 183–193

Pezner, A. K., and Coauthors, 2023: Increasing hypoxia on global coral reefs under ocean warming. *Nature Climate Change*, **13 (4)**, 403–409.

Poole, H., and W. Atkins, 1929: Photo-electric measurements of submarine illumination throughout the year. *Journal of the Marine biological Association of the United Kingdom*, **16 (1)**, 297–324.

Rabalais, N., R. J. Diaz, L. Levin, R. E. Turner, D. Gilbert, and J. Zhang, 2010a: Dynamics and distribution of natural and human-caused hypoxia. *Biogeosciences*, **7 (2)**, 585–619.

Rabalais, N. N., R. J. Diaz, L. A. Levin, R. E. Turner, D. Gilbert, and J. Zhang, 2010b: Dynamics and distribution of natural and human-caused hypoxia. *Biogeosciences*, **7 (2)**, 585–619.

Rainville, L., and R. Pinkel, 2001: Wirewalker: An autonomous wave-powered vertical profiler. *Journal of Atmospheric and Oceanic Technology*, **18 (6)**, 1048–1051.

Ramp, S., and Coauthors, 2022: Solitary waves impinging on an isolated tropical reef: Arrival patterns and wave transformation under shoaling. *Journal of Geophysical Research: Oceans*, **127 (3)**, e2021JC017 781.

Reid, E., S. Lentz, T. DeCarlo, A. Cohen, and K. Davis, 2020: Physical processes determine spatial structure in water temperature and residence time on a wide reef flat. *Journal of Geophysical Research: Oceans*, **125 (12)**, 1949–1965.

Reid, E. C., T. M. DeCarlo, A. L. Cohen, G. T. F. Wong, S. J. Lentz, A. Safaie, A. Hall, and K. A. Davis, 2019: Internal waves influence the thermal and nutrient environment on a shallow coral reef. *Limnology and Oceanography*, **64 (5)**, 1949–1965.

Rogers, J. S., S. G. Monismith, O. B. Fringer, D. A. Koweek, and R. B. Dunbar, 2017: A coupled wave-hydrodynamic model of an atoll with high friction: Mechanisms for flow, connectivity, and ecological implications. *Ocean Modelling*, **110**, 66–82

Scranton, M. I., and Coauthors, 2014: Interannual and subdecadal variability in the nutrient geochemistry of the Cariaco Basin. *Oceanography*, **27 (1)**, 148–159

Scully, M. E., 2010: The importance of climate variability to wind-driven modulation of hypoxia in Chesapeake Bay. *Journal of Physical Oceanography*, **40 (6)**, 1435–1440.

Scully, M. E., 2013: Physical controls on hypoxia in Chesapeake Bay: A numerical modeling study. *Journal of Geophysical Research: Oceans*, **118 (3)**, 1239–1256.

Sinnett, G., and F. Feddersen, 2019: The nearshore heat budget: Effects of stratification and surfzone dynamics. *Journal of Geophysical Research: Oceans*, **124 (11)**, 8219–8240.

Sinnett, G., S. R. Ramp, Y. J. Yang, M.-H. Chang, S. Jan, and K. A. Davis, 2022: Large-amplitude internal wave transformation into shallow water. *Journal of Physical Oceanography*, **52 (10)**, 2539–2554.

Stanley, D. W., and S. W. Nixon, 1992: Stratification and bottom-water hypoxia in the pamlico river estuary. *Estuaries*, **15**, 270–281.

Stramma, L., G. C. Johnson, J. Sprintall, and V. Mohrholz, 2008: Expanding oxygen-minimum zones in the tropical oceans. *science*, **320 (5876)**, 655–658.

Tartinville, B., E. Deleersnijder, and J. Rancher, 1997: The water residence time in the mururoa atoll lagoon: sensitivity analysis of a three-dimensional model. *Coral Reefs*, **16 (3)**, 193–203

Taylor, J., J. Edwards, M. Glew, P. Hignett, and A. Slingo, 1996: Studies within a flexible new radiation code. II: Comparisons with aircraft short-wave observations. *Q. J. R. Meteorol. Soc.*, **122**, 839–861.

Tkachenko, K. S., and K. Soong, 2017: Dongsha atoll: A potential thermal refuge for reef-building corals in the South China Sea. *Marine environmental research*, **127**, 112–125.

Turner, R., W. Schroeder, and W. J. Wiseman, 1987: The role of stratification in the deoxygenation of mobile bay and adjacent shelf bottom waters. *Estuaries*, **10**, 13–19.

Tyler, R. M., D. C. Brady, and T. E. Targett, 2009a: Temporal and spatial dynamics of diel-cycling hypoxia in estuarine tributaries. *Estuaries and Coasts*, **32**, 123–145.

Tyler, S. W., J. S. Selker, M. B. Hausner, C. E. Hatch, T. Torgersen, C. E. Thodal, and S. G. Schladow, 2009b: Environmental temperature sensing using raman spectra dts fiber-optic methods. *Water Resources Research*, **45 (4)**.

Vaquer-Sunyer, R., and C. M. Duarte, 2008: Thresholds of hypoxia for marine biodiversity. *Proceedings of the National Academy of Sciences*, **105 (40)**, 15 452–15 457.

Vaquer-Sunyer, R., and C. M. Duarte, 2011: Temperature effects on oxygen thresholds for hypoxia in marine benthic organisms. *Global Change Biology*, **17 (5)**, 1788–1797.

Weiss, R. F., 1970: *The solubility of nitrogen, oxygen and argon in water and seawater*, Vol. 17. Elsevier, 721-735 pp.

Willmott, C. J., 1982: Some comments on the evaluation of model performance. *Bulletin of the American Meteorological Society*, **63 (11)**, 1309–1313.

Zhang, J., and Coauthors, 2010: Natural and human-induced hypoxia and consequences for coastal areas: synthesis and future development. *Biogeosciences*, **7 (5)**, 1443–1467.